

KWAME NKRUMAH UNIVERSITY OF SCIENCE AND TECHNOLOGY, KUMASI,

COLLEGE OF SCIENCE

DEPARTMENT OF CHEMISTRY

KNLIST
**PREPARATION AND CHARACTERIZATION OF LOW DENSITY
POLYETHYLENE/CLAY NANOCOMPOSITES**

A Thesis Submitted to the Department of Chemistry,
Kwame Nkrumah University of Science and Technology, Kumasi,
In Partial Fulfillment of the Requirements for the Award
of the Master of Philosophy Degree in Polymer Science and Technology

BY

BONIFACE YEBOAH ANTWI

SUPERVISORS:

DR. J.A.M. AWUDZA AND

PROF. V.N. BERKO-BOATENG

JUNE 2012

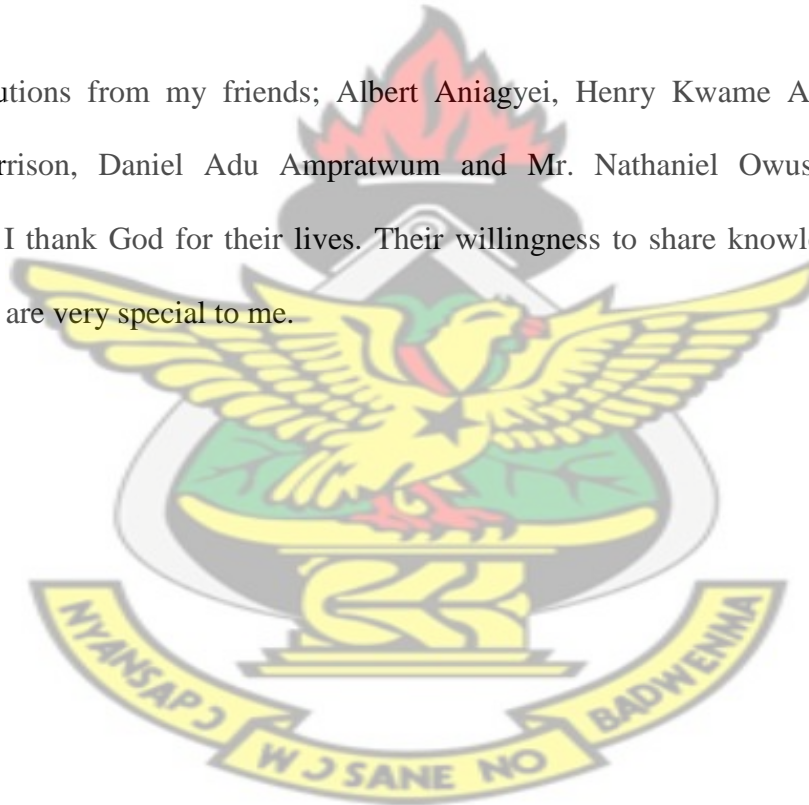
ACKNOWLEDGMENT

May the name of God be glorified, for the strength and grace that was freely granted me throughout the two years of postgraduate studies. I owe it all to God. Thank you, God.

I am also grateful to my parents and siblings, who supported me financially and emotionally. They are truly, a gift from above.

Special thanks to my supervisors, Dr. Johannes A. M. Awudza and Prof. Victor N. Berko-Boateng, for their tireless guidance and advice. God richly bless you.

The contributions from my friends; Albert Aniagyei, Henry Kwame Abgovi, Issaka Seidu, Francis Morrison, Daniel Adu Ampratwum and Mr. Nathaniel Owusu Boadi, are much appreciated. I thank God for their lives. Their willingness to share knowledge has brought me this far. You are very special to me.



DEDICATION

I dedicate this work to God Almighty.

KNUST



ABSTRACT

Low Density Polyethylene/clay nanocomposite is a thermoplastic polymer matrix, (Low density polyethylene), that has nanometer scale clay fillers dispersed in it. The characteristic structure (phase separated or intercalated or exfoliated structure) of the material enhances its properties. This work reports the preparation of Low density polyethylene filled with nanometer scale Ghanaian clay particles, and determines the structure of the material formed. Commonly known clay samples from Mfensi and Aferi communities in Ashanti region were used. Clay particles were modified with octadecylamine surfactant and incorporated into the LDPE matrix by melt mixing route. The modified Mfensi and Aferi clays, as well as LDPE/ Mfensi clay nanocomposites and LDPE/ Aferi clay nanocomposites, were characterized by Fourier Transform Infrared spectroscopy, (FTIR) and X-ray diffractometric (XRD) techniques. Crosslinking density of the materials was determined by swelling index measurements. Complete dispersion of clay fillers were best observed at very low clay loadings. LDPE/Aferi clay nanocomposites had modified Aferi clay particles well dispersed in them compared to that of LDPE/Mfensi clay nanocomposites. Modified clay contents increased the C-H vibrational motions of the LDPE/Mfensi and LDPE/Aferi clay nanocomposites. Crosslinking density of the nanocomposites decreased with increasing clay contents. This work concludes that, the best modified clay dispersion for property enhancement of Low Density Polyethylene/ clay nanocomposites was obtained at 2wt% clay loadings for both modified Mfensi and Aferi clay loadings. The structure of the LDPE/ clay nanocomposites formed was a phase separated structure.

TABLE OF CONTENT

Declaration	ii	
Acknowledgment	iii	
Dedication	iv	
Abstract	v	
List of tables	x	List
of figures	xii	
List of schemes	xvi	
List of equations	xvii	

KNUST

Chapter One

	1	
Introduction	1	1.1
Composite	4	
1.2 Polymer Composites	5	1.3
Polymer Nanocomposites	6	1.4
Layered silicates	8	1.4.1
Structure of clays	9	
1.4.2. Modification of clay layers	12	1.5
Nanocomposite structure	15	
1.5.1. Phase separated structure	16	
1.5.2 Intercalated structure	16	
1.5.3 Exfoliated structure	16	
1.6 Preparation of polymer/clay nanocomposites	17	
1.6.1 In situ intercalative polymerization	17	
1.6.2 Solution intercalation	18	
1.6.3 Melt intercalation	18	1.7
Structural characterization of polymer/clay nanocomposites	18	1.8 Study
Objectives	19	1.8.1
Specific Objectives	19	1.8.2
Justification of Specific Objectives	20	

Chapter Two

2 Literature review	21	2.1.
Theoretical Considerations of Experimental Methods	30	
2.1.1. Cation Exchange Capacity	30	
2.1.2. X-ray Defractometry	31	

2.1.3 X-ray Fluorescence	33	
2.1.4 Fourier Transform – Infrared Spectroscopy	35	
2.1.5 Polymer Crosslinking Measurements	40	
Chapter Three		
3 Experimental methods	42	3.1
Materials	42	
3.2 Samples Preparations	43	
3.2.1 Clay Samples	43	
3.2.2 Modification of Clay Samples (Organoclay preparation)	44	
3.2.3 Preparation of LDPE/Clay Nanocomposite	45	
3.2.4 LDPE/clay nanocomposite powder	46	
3.3 Characterization	47	
3.3.1 Cation exchange capacity of pristine clay (raw clay).	47	
3.3.2 X-ray fluorescence, (XRF), analysis on pristine clay.	48	
3.3.3 Fourier Transform - Infra Red spectroscopic analysis.	49	
3.3.4 X-ray Diffractometric Measurements.	49	
3.3.5 Cross-linking density Test	50	
Chapter Four		
4 Results and discussions	51	
4.1 Properties of clay samples	51	
4.2 FT-IR characterization	52	
4.2.1 FT-IR spectra of modified Mfensi clay compared to that of pristine Mfensi clay.	52	
4.2.2 FT-IR Spectra of Modified Aferi clay compared to that of Pristine Aferi clay.	55	4.2.3
FT-IR Spectra of Low Density Polyethylene/ Mfensi clay nanocomposites at different clay loadings.	57	
4.2.4 Influence of modified Mfensi Clay on the characteristic functional groups of Low Density Polyethylene, (LDPE)/ Mfensi clay nanocomposite.	59	
4.2.5 FT-IR Spectra of Low Density Polyethylene/ Aferi clay nanocomposite at different clay loadings.	61	4.2.6
Influence of Aferi Clay on the characteristic group vibrations of Low density Polyethylene.	63	functional
Diffractometric Characterization.	65	4.3 X-ray
4.3.1 XRD Characterization of organically modified Mfensi clay.	65	
4.3.2 XRD Characterization of organically modified Aferi clay.	67	
4.3.3 XRD Characterization of Low Density Polyethylene/ Mfensi clay nanocomposite.	69	
4.3.4 XRD Characterization of Low Density Polyethylene/ Aferi clay nanocomposite.	71	
4.4 Influence of Clay on crosslinking density of Low density polyethylene.	73	4.4.1

Crosslinking density of the LDPE/ Mfensi clay nanocomposites.				73
4.4.2 Crosslinking density of the LDPE/ Aferi clay nanocomposites.				74
Chapter Five				
5 Conclusions and Recommendations				76 5.1
Conclusions				76 5.2
Recommendations				77 References
	78			Appendices
				86
Appendix 1: Properties of pristine and modified Aferi and Mfensi clay samples.				86
Appendix 1.1 Major and minor elements of Pristine Mfensi and Aferi clay samples.				86 Appendix 1.2
Calculation of Cation Exchange Capacity of clay samples.				87
Appendix 2: Fourier Transform-Infra Red (FT-IR) spectra of octadecylamine, Pristine and Modified, Mfensi and Aferi clay Samples.				88 Appendix 2.1
Absorbance of C-H and Si-O peaks in Modified Mfensi and Aferi clays compared to pristine Mfensi and Aferi clays.				91
Appendix 3: Fourier Transform-Infra Red spectra, (FT-IR), of Low Density Polyethylene (LDPE) / Mfensi clay nanocomposites and Low Density Polyethylene/ Aferi clay nanocomposites at different clay loadings.				94 Appendix 3.1:
Comparison of C-H and Si-O peak absorbance in LDPE/ Mfensi clay nanocomposites at different percentage clay loadings.				100 Appendix 3.2:
Comparison of C-H and Si-O peak absorbance in LDPE/ Aferi clay nanocomposites at different percentage clay loadings.				106
Appendix 4: calculations of d-spacing of pristine and modified Mfensi and Aferi clay samples, as well as average particle size of the clay samples.				107 Appendix 4.1: d-spacing Mfensi and
calculations for pristine and modified Aferi clay samples.				107 Appendix 4.2: Calculating average and Aferi clay samples
particle size of modified Mfensi prepared.				108
Appendix 5: X-ray diffractograms of LDPE/ Mfensi clay nanocomposites and LDPE/ Aferi clay nanocomposites at different percentage clay loadings.				111

Mfensi and Aferi clays.

107 Table A.4.2: calculation of average particle size of modified Mfensi clay.

109 Table A.4.5: calculation of average particle size of modified Aferi clay.

110

KNUST



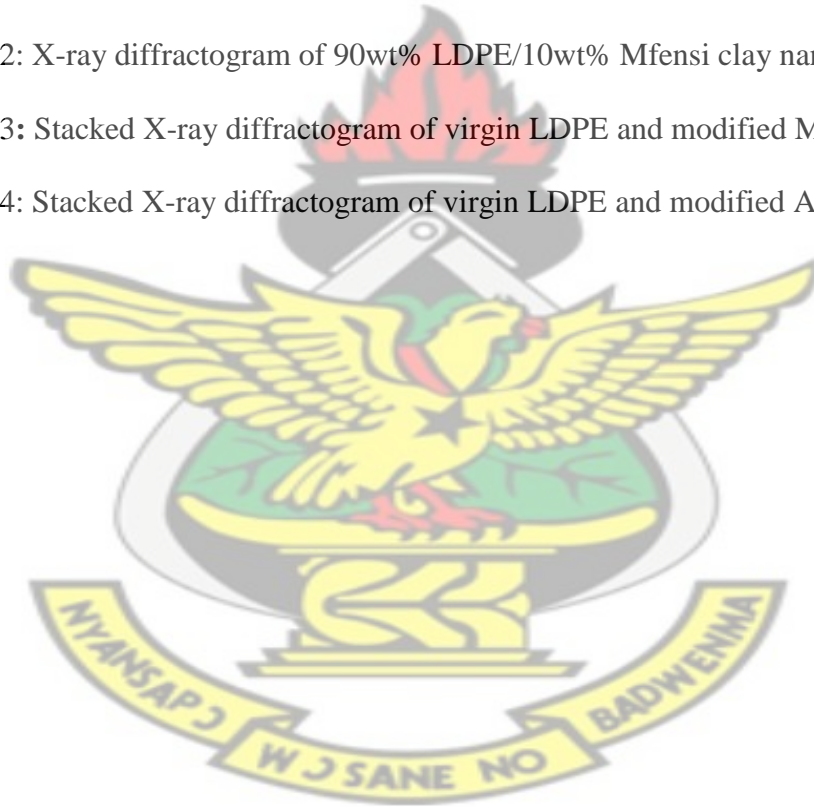
LIST OF FIGURES

Figure 1.1: Scheme of various types of nanofillers or fillers with nanoscale dimensions.	7
Figure 1.2: Scheme of the 2:1 smectite clay structure.	11
Figure 1.3: Scheme of the modification of clay layers by organic onium cations.	14
Figure 1.4: Diagramme of various configurations of organic oniums into the clay galleries.	15
Figure 1.5: Scheme of different types of composite arising from the interaction between layered silicates and polymers.	17
Figure 2.1: X-ray diffractometer set-up.	32
Figure 2.2: Bragg's Law.	32
Figure 2.3: X-ray fluorescence in a schematic representation.	34
Figure 2.4: The Electromagnetic Spectrum.	36
Figure 2.5: The Infrared Region of the Electromagnetic Spectrum.	36
Figure 2.6: A simple FT-IR spectrometer layout.	38
Figure 2.7a: Crosslink between Polymer Chains.	41
Figure 2.7b: Crosslinking introduced by clay layers.	41
Figure 3.1a: Micron Sieves and Aluminium Foil.	43
Figure 3.1b: Mortar and Pestle.	43
Figure 3.2a: Photograph of organoclay and octadecylamine mixture on a hot plate.	44
Figure 3.2b: Photograph of settled organoclay with a supernatant gelatinous white precipitate, on a hot plate.	44 Figure
3.3: Photograph of Set-up for the preparation of LDPE/clay nanocomposite.	45 Figure
3.4a: Photograph of prepared nanocomposite being ground on a grater.	46 Figure

3.4b: Photograph of powdered nanocomposite in a plastic envelopes.	46
Figure 3.5: Photograph of Flame Photometer Set-Up.	47
Figure 3.6: Photograph of SpectroX-lab, 2000 and a computer display set-up for XRF	48
Figure 3.7: Photograph of FT-IR Spectrometric Set-up.	49
Figure 3.8a: Photograph of X-ray Diffractometer.	50
Figure 3.8b: Photograph of computer for data display and analysis.	50
Figure 4.1: FT-IR Spectra of Modified Mfensi Clay compared to that of the Pristine Mfensi clay.	52
Figure 4.2: FT-IR Spectra of Pristine Aferi clay compared to that of the Modified Aferi clay.	55
Figure 4.3: FT-IR Spectra Comparing LDPE/Mfensi clay nanocomposites of different clay loadings to virgin LDPE.	57
Figure 4.4: Functional group absorbance versus percentage clay loadings of LDPE/ Mfensi clay nanocomposites.	59
Figure 4.5: FT-IR Spectra comparing LDPE/ Aferi clay nanocomposites of different percentage clay loadings to virgin LDPE.	61
Figure 4.6: Functional group absorbance versus percentage clay loadings of LDPE/ Mfensi clay nanocomposites.	63
Figure 4.8: X-ray diffractogram comparing modified Aferi clay to pristine Aferi clay.	67
Figure 4.9: X-ray diffractogram comparing LDPE/ Mfensi clay nanocomposites at 2%, 6% and 10% clay loadings to virgin LDPE.	69
Figure 4.10: X-ray diffractogram comparing LDPE/ Aferi clay nanocomposites to virgin LDPE	71
Figure 4.11: A Graph of Swelling Index of LDPE/ Mfensi Clay Nanocomposites against	

Percentage Clay Loadings.	73	Figure
4.12: A graph of crosslinking density of LDPE/ Aferi clay nanocomposites against Percentage Clay Loadings.	74	
Figure A.2.1: FT-IR Spectrum of Octadecylamine.	88	
Figure A.2.2: FT-IR Spectrum of Pristine Mfensi Clay.	89	
Figure A.2.3: FT-IR Spectrum of Modified Mfensi Clay.	90	
Figure A.2.4 : FT-IR Spectrum of Pristine Aferi Clay.	92	
Figure A.2.5 : FT-IR Spectrum of Modified Aferi Clay.	93	
Figure A.3.1: FT-IR Spectrum of Low Density Polyethylene, (100 wt% P / 0 wt% C).	94	
Figure A.3.2: FT-IR Spectrum of 98 wt% LDPE / 2 wt% Mfensi clay nanocomposite.	95	
Figure A.3.3: FT-IR Spectrum of 96 wt% LDPE / 4wt% Mfensi clay nanocomposite.	96	
Figure A.3.4: FT-IR Spectrum of 94 wt% LDPE / 6 wt% Mfensi clay nanocomposite.	97	
Figure A.3.5: FT-IR Spectrum of 92 wt% LDPE / 8 wt% Mfensi clay nanocomposite.	98	
Figure A.3.6: FT-IR Spectrum of 90 wt% LDPE / 10wt% Mfensi clay nanocomposite.	99	
Figure A.3.7: FT-IR Spectrum of 98 wt% LDPE / 2 wt% Aferi Clay nanocomposite.	101	
Figure A.3.8: FT-IR Spectrum of 96 wt% LDPE / 4 wt% Aferi Clay nanocomposite.	102	
Figure A.3.9: FT-IR Spectrum of 94 wt% LDPE / 6 wt% Aferi Clay nanocomposite.	103	
Figure A.3.10: FT-IR Spectrum of 92 wt% LDPE / 8 wt% Aferi Clay nanocomposite.	104	
Figure A.3.11: FT-IR Spectrum of 90 wt% LDPE / 10 wt% Aferi Clay nanocomposite.	105	
Figure A.4.1: Calculations average particle size of modified (organo) Mfensi clay.	109	
Figure A.4.2: Calculations of average particle size of modified Aferi clay.	110	
Figure A.5.1: X-ray diffractogram of virgin Low Density Polyethylene, (LDPE).	111	
Figure A.5.2: X-ray diffractogram of octadecylamine.	112	
Figure A.5.3: X-ray diffractogram of pristine (raw) Mfensi Clay.	113	

Figure A.5.4: X-ray diffractogram of Modified Mfensi Clay.	114
Figure A.5.5: X-ray diffractogram of Pristine Aferi Clay.	115
Figure A.5.6: X-ray diffractogram of Modified Aferi Clay.	116
Figure A.5.7: X-ray diffractogram of 98wt% LDPE/2wt% Aferi clay nanocomposite.	117
Figure A.5.8: X-ray diffractogram of 94wt% LDPE/6wt% Aferi clay nanocomposite.	118
Figure A.5.9: X-ray diffractogram of 90wt% LDPE/10wt% Aferi clay nanocomposite.	119
Figure A.5.10: X-ray diffractogram of 98wt% LDPE/2wt% Mfensi clay nanocomposite.	120
Figure A.5.11: X-ray diffractogram of 94wt% LDPE/6wt% Mfensi clay nanocomposite.	121
Figure A.5.12: X-ray diffractogram of 90wt% LDPE/10wt% Mfensi clay nanocomposite.	122
Figure A.5.13: Stacked X-ray diffractogram of virgin LDPE and modified Mfensi clay.	123
Figure A.5.14: Stacked X-ray diffractogram of virgin LDPE and modified Aferi clay.	124



LIST OF SCHEMES

Scheme 1: Instrumental Process in sample analysis by an FT-IR spectrometer.	39
Scheme 2: Preparation of organically modified clay.	66
Scheme 3: Formation of Phase separated Structured LDPE/ clay nanocomposite.	70

KNUST



LIST OF EQUATIONS

Equation – 2.1: Cation Exchange Capacity equation	31
Equation – 2.2: Bragg's Law	32
Equation – 2.3: Scherrer's equation	33
Equation – 2.4: Beer's Law	37
Equation – 3.1: Swelling Index equation	50

KNUST



CHAPTER ONE

1 INTRODUCTION

Polymer/clay nanocomposite is a value added polymer. This material gives researchers maximum control over the preparation, property enhancement, and application of polymers. The material has a continuous phase being the polymer and dispersed phase, the clay particles. The clay particles are reduced to dimensions within the nanometer scale (<100 nm) for effective property enhancement (Paula *et al.*, 2008). Amongst properties enhanced by the nanoclay particles are, barrier to gases, mechanical strength, thermal stability, flammability, and degradability of the polymeric material (Zhao *et al.*, 2005; Arunvisut *et al.*, 2007). Proper dispersion of the clay particles guarantees an efficient and effective property enhancement as reported (Lee *et al.*, 2007). Morphological description of the material is based on the degree of dispersion of clay particles. The terms, “tactoid”, indicate clay particles are agglomerated in the matrix, “intercalated” shows the polymer chains have inserted into the gallery space between the individual silicate layers, and “delaminated or exfoliated” results from the individual silicate layers not being close enough to interact with adjacent gallery cations (Gilman, 1999). Therefore, the silicate particles are considered well dispersed in a delaminated or exfoliated polymer/clay nanocomposite.

The miscibility of the clay particles in the polymer matrix is enhanced by modification of the clay surface and gallery spaces with a surfactant, mostly long chain cationic surfactant onium ions such as alkylammonium or phosphonium salts. These render hydrophilic clays hydrophobic, making them more miscible in hydrophobic polymer matrix (Ishida *et al.*, 2000; Roelofs *et al.*, 2006; López-Manchado *et al.*, 2003). During modification, the cationic surfactants, such as

octadecylamine replaces cations (Ca^{2+} and Na^+), adsorbed to the clay surfaces and galleries. Expansion of the clay galleries due to intercalation of polymer chains occur. The clay surface energy therefore reduces to enhance its miscibility, during formation of the polymer/clay nanocomposite (López-Manchado *et al*, 2003).

The most commonly used clay family is the smectite clays of 2:1 layered phyllosilicates. Their structures consist of two fused silica tetrahedral sheets sandwiching an edge-shared octahedral sheet of either aluminum or magnesium hydroxide. The silicate layers are coupled through relatively weak dipolar and van der Waals forces (Xu *et al*, 2004). This makes their interlayer galleries available to intercalation by both surfactant and polymer.

Filled polymer matrices include; vinyl addition polymers from common monomers like methyl methacrylate, methyl methacrylate copolymers, other acrylates, acrylic acid, acrylonitrile, styrene, 4-vinylpyridine, acrylamide, poly(N-isopropylacrylamide), and tetrafluoro ethylene (Sinha *et al*, 2003). In addition, selective polymers like poly(vinyl amide), poly(N-vinyl pyrrolidone), poly(vinyl pyrrolidinone), poly(vinyl pyridine), poly(ethylene glycol), poly(ethylene vinyl alcohol), poly(vinylidene fluoride), poly(p-phenylenevinylene), polybenzoxazole, poly(styrene-co-acrylonitrile), ethyl vinyl alcohol copolymer, polystyrene–polyisoprene diblock copolymer, and others have been used (Sinha *et al*, 2003). Polycondensates have also been used in nanocomposites preparation with layered silicates. These include nylon 6, poly(1-caprolactone), poly(ethylene terephthalate), poly(trimethylene terephthalate), poly(butylene terephthalate), polycarbonate, polyethylene oxide, ethylene oxide copolymers, poly(ethylene imine), poly(dimethyl siloxane), polybutadiene, butadiene copolymers, epoxidized natural rubber, epoxy polymer resins (EPR), phenolic resins, polyurethanes (PU), polyurethane

urea, polyimides, poly(amic acid), polysulfone, polyetherimide and fluoropoly(ether-imide) (Sinha *et al*, 2003). Polyolefins such as polypropylene (PP), polyethylene (PE), polyethylene oligomers copolymers such as poly(ethylene-covinyl acetate) (EVA), ethylene propylene diene methylene linkage rubber (EPDM), and poly(1-butene) have also been used (Sinha *et al*, 2003).

In general, nanocomposites can be formed in one of three ways by, solution dispersion, *in-situ* polymerization and melt blending or melt mixing. The solution dispersion method involves mixing a preformed polymer solution with clay. This is based on a solvent system in which the polymer or pre-polymer is soluble and the silicate layers are swellable. *In-situ* polymerization involves the dispersion and distribution of clay layers in the monomer followed by polymerization. The layered silicate is swollen within the liquid monomer or a monomer solution so that polymer formation can occur between the intercalated sheets. The melt blending process involves mixing both layered silicate and polymer with heating the above the glass transition temperature of the polymer. During this process, the polymer chains diffuse from the bulk polymer melt into the galleries between the silicate layers (Gupta *et al*, 2008). Of the three general routes to polymer/clay nanocomposites, melt intercalation is the most widely used route, mainly because it involves no solvent, relatively cost effective, and industrially applicable.

Characterization of polymer/clay nanocomposite is mainly focused on confirming clay modification in Fourier Transform-Infra Red Spectroscopy, which indicates the presence of surfactant functional groups and that of the clay,(Nantana, 2004). X-ray diffractometry (XRD) is onward employed to determine the extent of surfactant intercalation into clay galleries. This is evident in the *d*-spacing of intercalated layered silicates, calculated from the Braggs law ($\lambda=2d\sin\theta$). Dry inorganic layered silicates (smectides) show diffraction at about 8 degree, which corresponds to a *d*-spacing of about 1 nm (Alexandre *et al*, 2001).

Due to its easy to use and availability, X-ray diffraction (XRD) is most commonly used to probe the nanocomposite structure. However, XRD can only detect the periodically stacked silicate layers; disordered or exfoliated layers are not detected. Transmission Electron Microscopy (TEM) and Scanning Electron Microscopy (SEM) are further employed to complement X-ray diffractogram (Zhang *et al*, 2008).

1.1. Composite

A composite is any material made of more than one component. Composite materials are solid multiphase materials formed through the combination of materials with different structural, physical and chemical properties. This makes composites different from the other multi component systems such as blends and alloys. Composites are widely used in such diverse areas as transportation, construction and consumer products (Giannelis, 1996). Composites offer unusual combinations of component materials properties such as weight, strength, stiffness, permeability, electrical conductivity, biodegradability and optical properties that is difficult to attain separately by individual components. A composite material can be tailored to have specific properties that will meet special requirements. The optimum design of composite component materials and manufacturing process to meet the target properties for specific engineering application is very important. In a composite, one phase is continuous and is called matrix, while the other is filler or reinforced material which make the dispersed phase. Composite materials based on the nature of matrix phase can be divided into polymeric, ceramic and metallic composites (Carlsson, *et al*, 1987). Usually the filler phase is embedded in the host matrix phase to make a composite which has properties far from either phase alone.

Polymers often have advantages over other materials such as metals and ceramics. They are widely used in various technical applications because of their unique advantages such as ease of production, light weight and ductility. However they have lower mechanical, modulus and strength properties compared to that of metals and ceramics. The commercial importance of polymers and their increasing use, results in the continuous demand for improvements of their properties to meet the necessary applications. By the composite technology, polymer properties are improved while maintaining their light weight and ductile nature (Jordan *et al.*, 2005).

1.2. Polymer Composites

Polymer composite is made by the combination of a polymer and synthetic or natural inorganic filler. Fillers are employed to improve the desired properties of the polymer or simply reduce the cost. Polymer composites with improved mechanical, thermal, barrier and fire retardancy properties are widely used in very large quantities in variety of applications. However by the application of conventional fillers such as talc, calcium carbonate, fibers, etc, a large amount of filler is used in the polymer matrix. This results in significant improvements in the composite properties. But it introduces other undesired properties such as brittleness or loss of opacity into the material (Zhang *et al.*, 2003).

The final properties of reinforced polymers (composites) are influenced by the nature, properties and content of components, dimensions of components and micro structure of composite and interfacial interactions between matrix and dispersed phase. The efficiency of properties improvements depends strongly on the properties (mechanical) of the filler, the adhesion between matrix and filler and especially on the aspect ratio of the filler. The aspect ratio of the filler is very important and crucial for many properties in composite such as electrical (Al-Saleh

et al., 2010; Grossiord *et al.*, 2008), mechanical (Zhang *et al.*, 2007) and thermal (Meneghetti *et al.*, 2006) properties. Polymer composites with the high aspect ratio of nano-fillers such as platelet clays, carbon nanotubes and nanofibers are receiving considerable attention due to their unique multifunctional and highly enhanced properties. Combination of filler nanoscale dimension and high aspect ratio with its nanoscale dispersion within polymer matrix leads to the significant improvements in the polymer properties at very low filler volume fractions. As a result of lower filler using, the macroscopic homogeneity and low density of primary polymer retains as well as its opacity in the final nanocomposite system. Polymer nanocomposites are the new class of hybrid materials in this category (Mittal, 2009).

1.3. Polymer Nanocomposites

A nanocomposite is defined as a composite material in which at least one dimension of at least one component is in the nanometer size scale (< 100 nm). Although the term nanocomposite represent a new and exciting field in polymer science and technology, the nanocomposites have actually been used for centuries by the nature. Using natural materials and polymers such as carbohydrates, lipids and proteins, nature makes strong nanocomposites such as bones, shells and wood (Hussain *et al.*, 2006). However in recent years the characterization and control of structures at the nanoscale have been studied, investigated and exploited by the learning from the natural surroundings. Consequently the nanocomposite technology has emerged as an efficient and powerful strategy to upgrade the structural and functional properties of synthetic polymers. This is the new nanocomposite science, and was started by the Toyota report (Usuki *et al.*, 1993) on the superior improvement in the properties of nylon-6 by the preparation of exfoliated nylon-6/clay nanocomposites. It has been continued by more recent studies with carbon nanotubes,

carbon nanofillers, exfoliated graphite, nanocrystalline metals and fibers modified with inorganic fillers used in polymeric composites (Paul *et al*, 2008).

In polymer nanocomposites, the filler has at least one dimension in the nanometer scale. This leads to the tremendous interfacial contacts between the polymer and inorganic filler which yield superior properties to that of bulk polymer phase. When the dimensions of filler particles are decreased to the nanoscale, their properties change also significantly (Kumar *et al.*, 2009). This is well-known as nano-effect. Studies and modelings using quantum mechanics reveal that, the enhanced properties of nanocomposites are strongly dependent on the particular features of nanofillers system, in particular, its content, aspect ratio and the ratio of filler mechanical properties to those of the matrix (Sheng *et al.*, 2004). The nanoscale is considered where the dimensions of filler particles (diameter), platelets (thickness) or fibers (diameter) are in the size range of 1-100 nm (Figure1.1).



Figure 1.1: Scheme of various types of nanofillers or fillers with nanoscale dimensions. (Olad, 2010.)

A broad spectrum of polymer properties can be improved by nanocomposite technology such as mechanical, thermal, barrier, durability, chemical stability, flame retardancy, scratch/wear

resistance, biodegradability as well as optical, magnetic and electrical properties (Armentano *et al.*, 2010; Cosoli *et al.*, 2008; Ma *et al.*, 2006; Pandey *et al.*, 2005).

The final properties of nanocomposites are determined by the component properties, composition, micro-structure and interfacial interactions. However it has been established that the properties of nanocomposites are strongly influenced by the dimensions and micro structure of filler phase (Sheng *et al.*, 2004). In other word the filler nature has a main effect on the final morphology and properties of the polymer nanocomposite. Clays are one group of nano-fillers which have been widely used for the preparation of polymer nanocomposites. Recently there has been a growing interest for the development of polymer/clay nanocomposites due to their dramatic improved properties compared to the conventional filled polymers in a very low fraction of filler addition (LeBaron *et al.*, 1999; Thostenson *et al.*, 2005). Polymer/clay nanocomposites have received intense attention and research interest driven by the unique properties which can never be obtained by micro size fillers or especially by other nanofillers. The value added properties enhanced without the sacrificing of pure polymer processability, mechanical properties and light weight, make the clays more and more important in modern polymer industry. Clay minerals belong to silicates with layered structure known as layered silicates.

1.4. Layered silicates

The layered silicates are natural or synthetic minerals consisting of the regular stacks of aluminosilicate layers with a high aspect ratio - (length/thickness), and high surface area. Layered silicates are easily available and have low cost. The current most popular layered silicates used in polymer nanocomposites preparation are clays.

Clay is a soil fraction with particle size being less than 2 μm . The clay layers have a thickness of about 1 nm (Gieseking, 1975). There are many members of clays with some difference in their formula, structure and properties including swelling and exfoliation. Those members who are able to be exfoliated by polymer chains or monomers and distributed as individual clay layers within polymer matrix are suitable for the preparation of polymer nanocomposites. The individual clay layers can cause dramatic improvements in polymer properties due to their high aspect ratio and high interfacial interactions with polymer matrix (Mittal, 2007).

1.4.1 Structure of clays

Clays have layered structure. The layers are built from tetrahedral sheets in which a silicon atom is surrounded by four oxygen atoms and octahedral sheets in which a metal like aluminium or magnesium is surrounded by eight oxygen atoms (Sposito, 1989). The tetrahedral and octahedral sheets are fused together by sharing the oxygen atoms. Unshared oxygen atoms are present in hydroxyl form. Two main arrangements of tetrahedral and octahedral sheets fused together make the one layer structure of clay. One tetrahedral fused to one octahedral (1:1) is known as kaolin group with the general composition of $\text{Al}_2\text{Si}_2\text{O}_5(\text{OH})_5$ and the layer thickness of ~ 0.7 nm. The crystal lattice consisted of one octahedral sheet sandwiched between two tetrahedral sheets (2:1) with the total thickness of 0.94 nm is well known as phyllosilicates (Greenland, *et al*, 1978). The 2:1 phyllosilicate layers can be electrostatically neutral with no inter layer ion present known as pyrophyllite. Due to the absence of inter layer ions, the layers do not expand in water. When silicon in tetrahedral sheets is substituted by aluminium, the 2:1 structure is called mica. The negative charge induced by this substitution is balanced by the insertion of potassium cations between layers. Due to the equal size of potassium cation and the hole created by Si/Al tetrahedral sheets, the presence of potassium cation makes no inter layer spacing. Consequently the 2:1 layers are held together strongly and the swelling or exfoliation of layers is not possible.

When in neutral pyrophyllite, the aluminum cations in the octahedral layers are partially substituted by divalent magnesium or iron cations the smectite clay group is formed. The negative charge created by this substitution is balanced by inter layer counter sodium or calcium ions. The charge created on the layers is not locally constant and varies from layer to layer. An average charge value is considered for the layers which can be determined by cation exchange capacity (CEC) measurement (Borden *et al*, 2001). Due to the unequal size of inter layer cations with the holes of tetrahedral sheets, the presence of inter layer cations causes an inter layer spacing. The layers stay near together with a regular gap between them. The gap is called inter layer or gallery. The thickness of the repeated units in a regular multilayer structure contained of one layer and one inter layer space is called d-spacing (d_{001}) or basal spacing (Figure 1.2). The basal spacing of clays can be measured or calculated from their X-ray diffraction patterns (Kloprogge *et al*, 1999). The inter layer dimension is also dependent to the clay nature and swelling or hydration degree of inter layer cations. The inter layer distance is about 1 nm for montmorillonite. The electrostatic and van der Waals forces holding the layers together are relatively weak, as inter layer distance varies depending on the charge density on the layers, inter layer cation radius and its degree of hydration. Because of the inter layer spacing and weak inter layer forces, the cations present between the layer can be hydrated in aqueous solutions known as clay swelling (Mittal, 2009). The swelling increases the inter layer spacing. Due to the inter layer spacing and weak forces between layers, especially in the hydrated form, other molecules also can be intercalate between layers, which may lead to the expansion of layered lattice and finally causing the separation of individual layers. The unique intercalation/exfoliation behavior of smectite clay minerals which is responsible for the high aspect ratio of this clay type makes them very important and powerful as reinforcing filler for polymers.

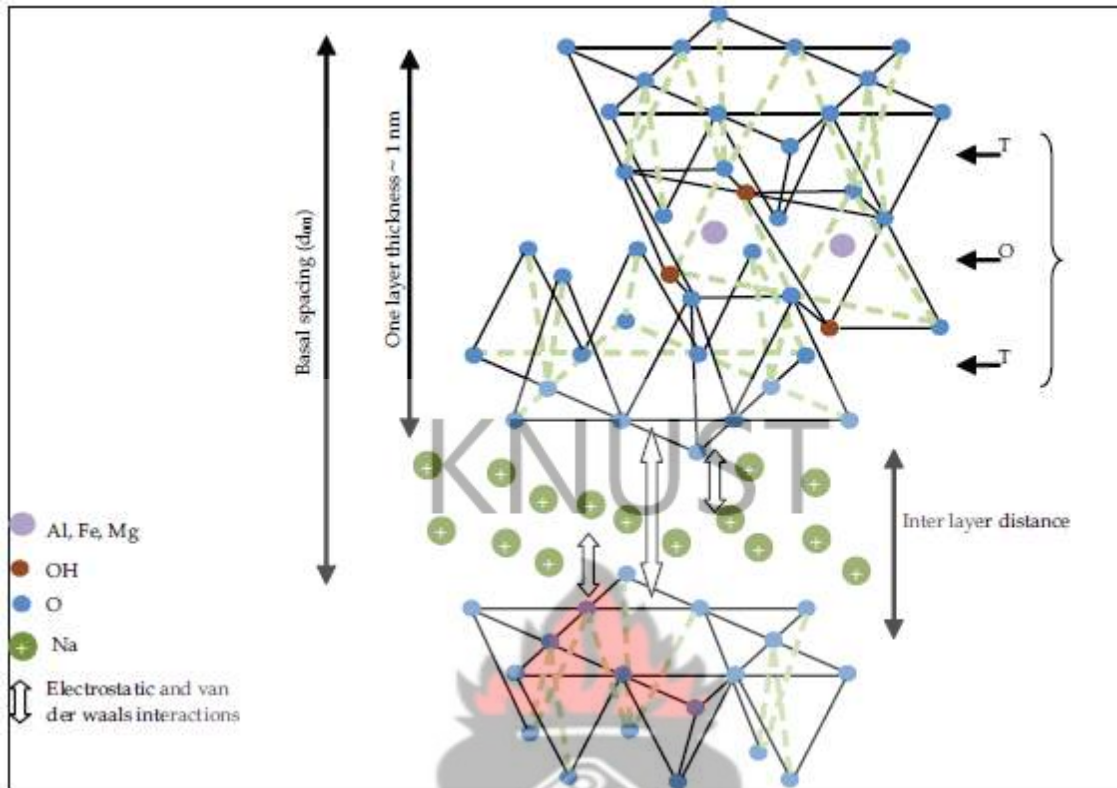


Figure 1.2: Scheme of the 2:1 smectite clay structure (Kloprogge *et al*, 1999).

The dimension of 2:1 layer structures are about 1 nm in thickness and 30 nm to several microns in lateral, depending on the source and preparation method of clay. The clay lateral dimensions and its ability to disperse into separated layers determine the aspect ratio of clay which is strongly important in polymer/clay interfacial interactions. Separation of individual clay layers having about 1 nm thickness display a perfect structure which strongly contributes to the improvement of polymer properties.

Clay minerals belong to the nanoplatelet structured filler particles in polymer composite technology. Montmorillonite, hectorite and saponite are the well known smectites which are most commonly used in the preparation of polymer nanocomposites (Table 1) (Pavlidou and Papaspyrides, 2008).

Smectites	Chemical formula
Montmorillonite	$M_x(Al_{4-x}Mg_x)Si_8O_{20}(OH)_4$
Hectorite	$M_x(Mg_{6-x}Li_x)Si_8O_{20}(OH)_4$
Saponite	$M_xMg_6(Si_{8-x}Al_x)O_{20}(OH)_4$

Table 1: Chemical structure of commonly used smectite type clays, M: monovalent cation, x: degree of cations isomorphous substitution in octahedral sheets (Pavlidou and Papaspyrides, 2008).

Other clay materials such as 1:1 structures, 2:1 pyrophyllites and mica are not commonly used in polymer nanocomposites because they have no useful intercalation/exfoliation characteristics or they cannot be easily separated into layers. Due to the higher charge density on their layers, they are strongly stacked together as such intercalations of polymer chains between layers are much difficult to achieve.

1.4.2. Modification of clay layers

The preparation of polymer/clay nanocomposites with good dispersion of clay layers within the polymer matrix is not possible by physical mixing of polymer and clay particles. It is not easy to disperse nanolayers in most polymers due to the high face to face stacking of layers in agglomerated tactoids and their intrinsic hydrophilicity which makes them incompatible with hydrophobic polymers. Only a few hydrophilic polymers such as poly(ethylene oxide) and poly(vinyl alcohol) can be miscible with clay nanolayers (Pavildou and Papaspyrides, 2008).

The intrinsic incompatibility of hydrophilic clay layers with hydrophobic polymer chains prevents the dispersion of clay nanolayers within polymer matrix leading to weak interfacial interactions. Incompatibility and weak interfacial interactions hinders the exfoliation and preparation of dispersed stable nanocomposite with improved properties. Modification of clay

layers with hydrophobic agents is necessary in order to render the clay layers more compatible with polymer chains. This is a surface modification which causes to the reduction of surface energy of clay layers and match their surface polarity with polymer polarity. The organoclays with lowered surface energy are more compatible with polymers. The polymer molecules are able to intercalate within the interlayer space or galleries under well defined experimental conditions (Chigwada *et al.*, 2006).

The surface modification of clay layers can be achieved through a cation exchange process by the replacement of sodium and calcium cations present in the interlayer space or clay galleries by alkylammonium or alkylphosphonium (onium) cations (Ahmad *et al.*, 2009). In addition to the surface modification and increasing the hydrophobicity of clay layers, the insertion of alkylammonium or alkylphosphonium cations into the galleries leads to an increase in the interlayer spacing which promotes intercalation of polymer chains into the galleries during nanocomposite preparation (Chigwada *et al.*, 2006).

The alkylammonium or alkylphosphonium cations can provide functional groups which interact with polymer chains or initiate the polymerization and therefore increase the interfacial interactions. Figure 1.3 schematically shows the organic modification of clay layers using alkylammonium cations via the ion exchange process.

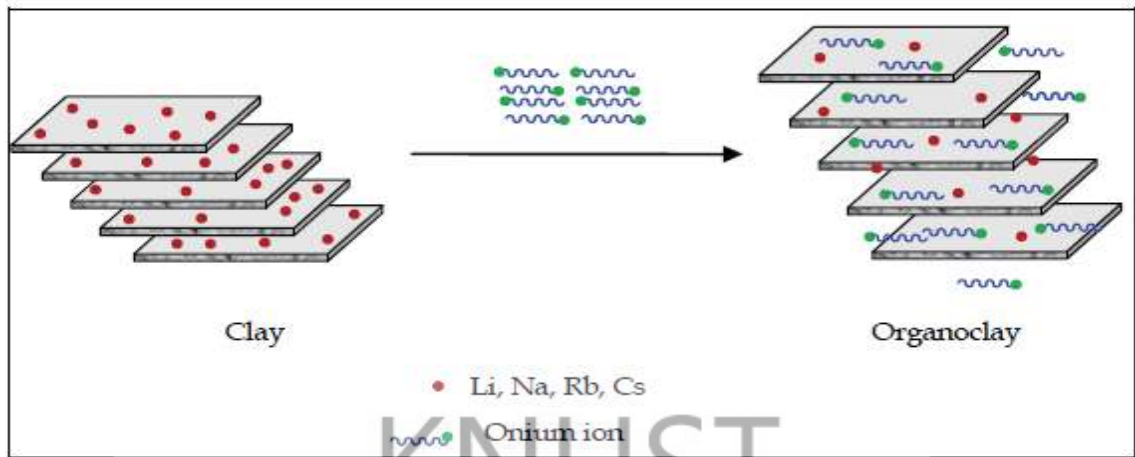


Figure 1.3: Scheme of the modification of clay layers by organic onium cations (Quang, 2006).

The ion exchange process is carried out in aqueous solution with the hydrated inter layer cations. The affinity of monovalent sodium cations to hydration promotes the ion exchange process and increases the efficiency of organic modification of clay layers. Clays containing divalent counter cations such as calcium cannot be easily hydrated and therefore their replacement by ion exchange process is not efficient (Ray and Okamoto, 2003).

The structure of the organoclays and their basal spacing depends on the molecular size of organic onium and its configuration in the interlayer spacing after modification. Figure 4 schematically shows the various configurations of the organic modifiers inserted within the clay layers by ion exchange with sodium cations.

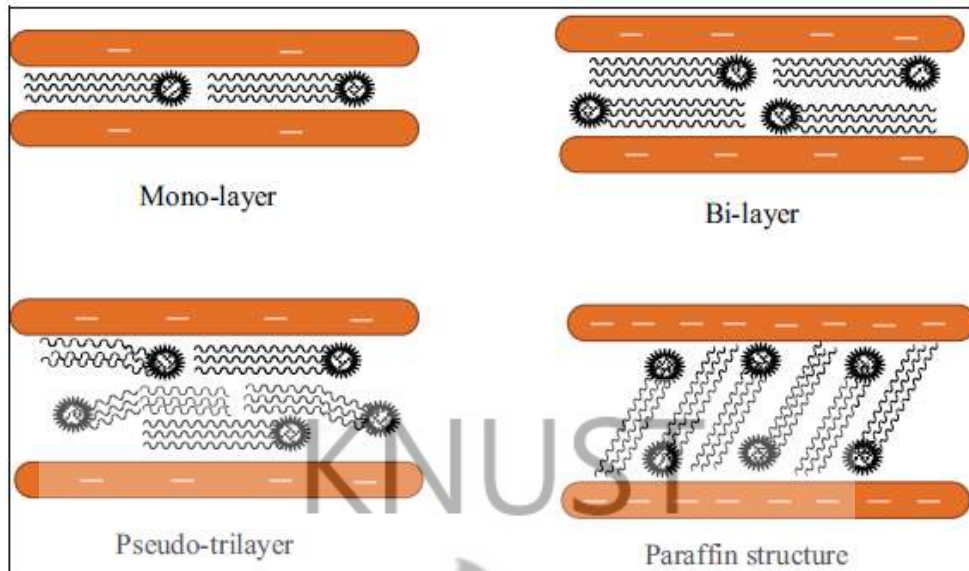


Figure 1.4: Diagramme of various configurations of organic oniums into the clay galleries (Lagaly, 1986).

The organic tail of onium laid up parallel to the clay layer can be obtained with lower charge densities. By increasing the charge density of clay layers, bilayer or trilayer structures with more increasing of inter layer spacing can be formed. Finally with the higher charge densities more inter layer spacing is obtained by the formation of paraffin structure. Increasing of temperature can lead to the structures with more basal spacing by increasing the mobility of onium molecules into the galleries. However in a given temperature two parameters determine the equilibrium layer spacing, the charge density of layers, driving the packing and number of onium chains entering the interlayer space, and the size or chain length of organic tail in onium compound (LeBaron *et al*, 1999).

1.5. Nanocomposite structure

The structures of polymer/clay nanocomposites are classified according to the degree of intercalation and exfoliation of polymer chains into the clay galleries. These include, Phase separated structure, intercalated structure and exfoliated structure.

1.5.1. Phase separated structure

When the organic polymer is interacted with inorganic clay (unmodified clay), the polymer is unable to intercalate within the clay layers and the clay is dispersed as aggregates or particles with layers stacked together within the polymer matrix. The obtained composite structure is considered as “phase separated” (Mark, 1996). The properties of phase separated polymer/clay composites are in the range of traditional micro composites.

1.5.2 Intercalated structure

When polymer chains are inserted into the interlayer spacing and causes an increase in the interlayer spacing, with the periodic array of the clay layers maintained, the intercalated nanocomposite is formed (Reynaud *et al*, 1999). The presence of polymer chains in the galleries leads to a decrease in the electrostatic forces between the layers but it is not totally dissolved.

1.5.3 Exfoliated structure

Exfoliated or delaminated structure is obtained when the insertion of polymer chains into the clay galleries separates the layers into individual layers dispersed within the polymer matrix. At 80-100 Å interlayer spacing an exfoliated structure is obtained. The complete dispersion of individual clay layers, leads to high aspect ratio of the clay layers, as such, lower clay content is required for an exfoliated nanocomposite (Reynaud *et al*, 1999). A significant improvement in polymer properties is obtained due to the large surface area interactions between polymer and clay particles. Various polymer/clay structural configurations have been shown in Figure 1.5.

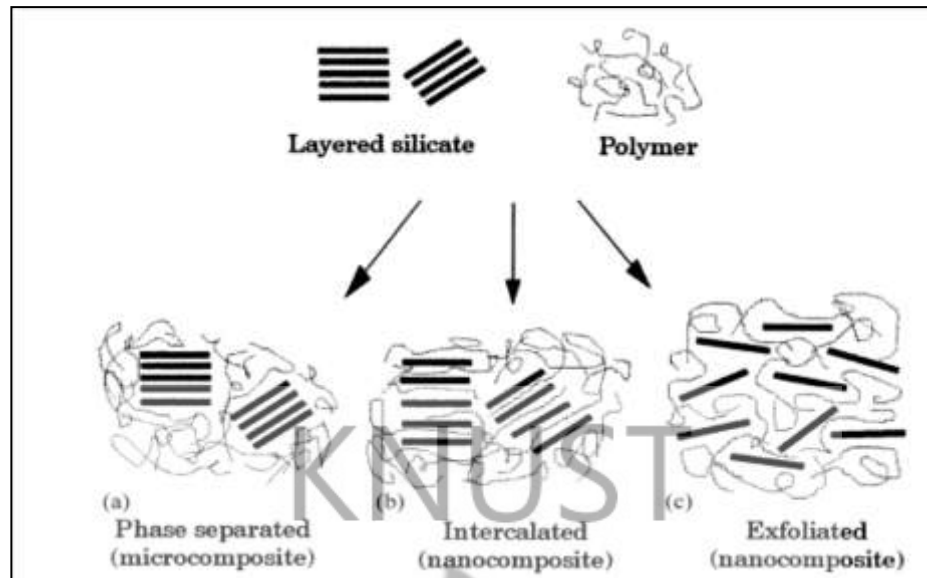


Figure 1.5: Scheme of different types of composite arising from the interaction between layered silicates and polymers: (a) phase separated microcomposite; (b) intercalated nanocomposite and (c) exfoliated nanocomposite (Werne *et al.*, 1999).

1.6. Preparation of polymer/clay nanocomposites

Different synthetic approaches have been used for the preparation of polymer/clay nanocomposites. In general there are three preparation methods including in situ intercalative polymerization, solution intercalation, and melt intercalation.

1.6.1 In situ intercalative polymerization

This technique was the first method used for the preparation of polymer/clay nanocomposite by Toyota research group in the preparation of Nylon-6 nanocomposite from caprolactam monomer (Usuki *et al.*, 1993).

In this method, the organoclay is swollen in monomer liquid or monomer solution. The monomers diffused into the interlayer spacing are polymerized, by heat or radiation, or diffusion of an initiator, or organic initiator present on the organic modifier of clay (Hussain *et al.*, 2006). The polymerization is carried out within the clay galleries as well as extra galleries. The growth of polymer chains results in the exfoliation and formation of disordered structure. This method is

suitable for the preparation of thermoset/clay nanocomposites and has been widely used for epoxy matrix (Lan *et al.*, 1995).

1.6.2 Solution intercalation

In this method the polymer or prepolymer is dissolved in a solvent and the clay is dispersed in the same solution. The clay is swollen in the solvent and the polymer chains intercalate between the layers. The intercalated nanocomposite is obtained by solvent removal through vaporization or precipitation. However due to the need for solvent, this technique cannot be industrially applied (Wang *et al.*, 2004).

1.6.3 Melt intercalation

Clay is mixed within the polymer matrix in molten temperature. The conventional methods such as extrusion and injection molding are used for dispersion of clay layers within the polymer matrix. This method is an effective technique for the preparation of thermoplastic nanocomposites (Kornmann *et al.*, 2001). The polymer chains are intercalated or exfoliated into the galleries. Clays are organically modified to enhance their compatibility with polymer matrix, to enhance exfoliation. Melt intercalation is industrially applicable since no solvent is required in the process (Ray *et al.*, 2003).

1.7 Structural characterization of polymer/clay nanocomposites

In the preparation of a polymer/clay nanocomposite it is important to know the degree of intercalation/exfoliation and its effect on the nanocomposite moderate properties. In other words there is the need to analyze the micro structure of the prepared nanocomposite. Two common techniques including X-ray diffraction (XRD) analysis and transmission electron microscopy (TEM) are widely used to characterize the micro structure of nanocomposite as well as pure clay

or pure organoclay (Vaia *et al*, 2002). Clays and organoclays show a characteristic peak in XRD analysis due to their regular layered structures. The peak is indicative of the platelet separation or d-spacing in clay structure. Using the peak width at half maximum height and peak position (2θ) in the XRD spectra the inter layer space can be calculated utilizing Bragg's law (eq. 1).

$$\sin \theta = \frac{n\lambda}{2d} \dots \dots \dots (1)$$

Where λ is wave length of X-ray radiation used in the diffraction experiments, d is the space between layers in the clay lattice and θ is measured diffraction angle. Any change in the interlayer or d-spacing of a clay lattice by organic modification or polymer intercalation causes to the change in the position, broadness and intensity of the characteristic peak in XRD spectra. According to the Bragg's law, increasing of d-spacing results in broadening and shifting of related XRD peak toward lower diffraction angles (2θ) (Vaia *et al*, 2003) . By monitoring the position (2θ), shape and intensity of the characteristic peak for organoclay in nanocomposite structure it is possible to determine the degree of intercalation/exfoliation.

1.8 Study Objectives

This project work seeks to prepare and characterize low density polyethylene/clay nanocomposite materials. Low density polyethylene shall be the matrix, while Ghanaian clays from Mfensi and Aferi shall be the separate fillers to be used.

1.8.1 Specific Objectives are to:

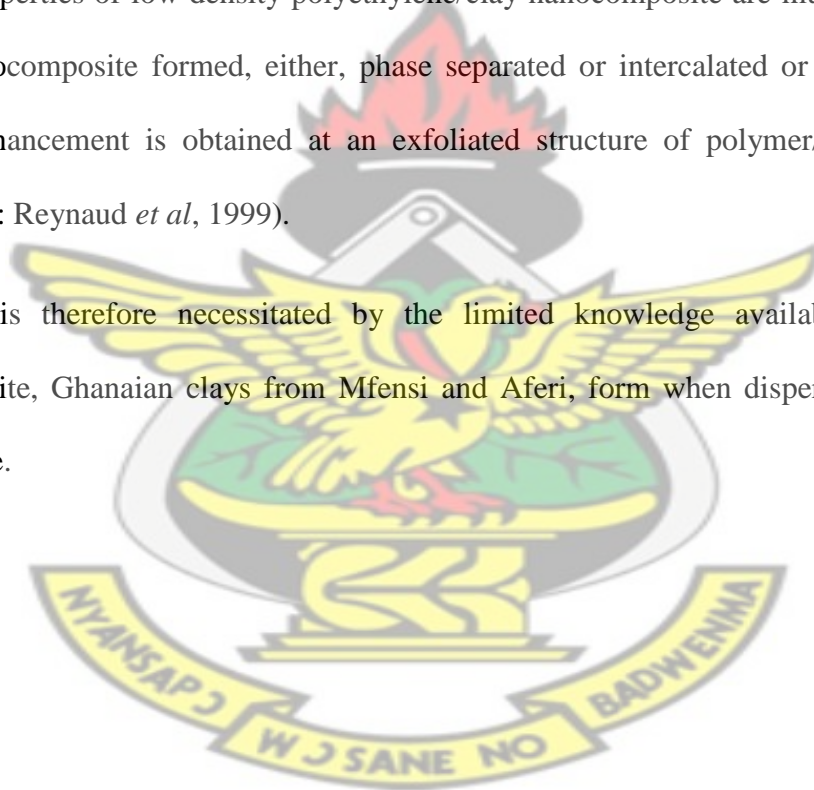
1. Prepare organically modified clays from Mfensi and Aferi.
2. Prepare low density polyethylene/ clay nanocomposites.
3. Determine the type of nanocomposite prepared.
4. Compare findings to literature.

1.8.2 Justification of Specific Objectives

Incorporation of small amount of clay nanoparticles into low density polyethylene matrix is reported to yield polymeric material of improved properties such as, high mechanical properties, high barrier to gas properties, and high thermal stability (Kato *et al*, 2011). These enhanced properties qualify the nanocomposite to replace metals, wood and other materials in several applications, such as, furniture, packaging, and automobile parts (Kato *et al*, 2011).

Superior properties of low density polyethylene/clay nanocomposite are much dependent on the type of nanocomposite formed, either, phase separated or intercalated or exfoliated. The best property enhancement is obtained at an exfoliated structure of polymer/clay nanocomposite (Mark, 1996; Reynaud *et al*, 1999).

This work is therefore necessitated by the limited knowledge available on the type of nanocomposite, Ghanaian clays from Mfensi and Aferi, form when dispersed in Low Density Polyethylene.



CHAPTER TWO

2 LITERATURE REVIEW

Several research works have proposed different approaches to the preparation of organophilic clay for polymer/clay nanocomposite. These routes are generally differentiated by the type of surfactant employed and the clay type involved. Commercially prepared montmorillonite is popular in the clays used.

Masaya *et al.*, (1997), intercalated Na^+ -montmorillonite with stearylammmonium. Interlayer spacing of both pristine and modified clay was measured by X-ray diffraction. The interlayer spacing of the sodium montmorillonite was 12 Å, while that of the stearylammmonium modified montmorillonite was 22 Å, clearly indicating that, the stearylammmonium intercalation into the clay galleries.

Song *et al.*, (2001), used X-ray powder diffraction (XRD), thermal gravimetric analysis (TGA), surface area measurements, and near-edge X-ray absorption fine structure (NEXAFS) spectroscopy to examine the surface properties of organosilane-modified smectite-type aluminosilicate clays. Organic modified clays derived from the reactions of montmorillonite with octadecyltrichlorosilane ($\text{C}_{18}\text{H}_{37}\text{SiCl}_3$) and octadecyltrimethoxysilane [$\text{C}_{18}\text{H}_{37}\text{Si}(\text{OMe})_3$] were highly hydrophobic. Surface loadings of the modified clays were dependant on the organosilane and the solvent, and they range from 10 to 25 wt%. The organic species were probably adsorbed to the outer surfaces and bound to the edges of the clay via condensation with edge-OH groups. Encapsulation of montmorillonite with $\text{C}_{18}\text{H}_{37}\text{SiCl}_3$ and $\text{C}_{18}\text{H}_{37}\text{Si}(\text{OMe})_3$ resulted in a hydrophobic coating that acted like a “cage” around the clay particles to limit diffusion. Basal spacing of the organic modified clays remained at ~15 Å upon heating to 400°C in N_2 , whereas

those of unmodified clays collapsed to ~ 10 Å. A considerable reduction in surface area (by 75–90%) of the organic modified clays was observed, which was consistent with the existence of a surface coating. The carbon and oxygen K-edge NEXAFS spectroscopy of the modified montmorillonite surfaces showed that surface coatings on the outside of the clay particles existed.

Jyh *et al*, (2001), also modified Na^+ -montmorillonite with the surfactant, stearyltrimethyl ammonium chloride, and characterized the resulting organoclay by an X-ray diffractometry, in which calculations from Bragg's law indicated an increase in the d-spacing of the organo clay, since, the measured d_{001} -spacing of pristine montmorillonite was 1.40 nm corresponding to $2\theta = 6.25^\circ$ and after cation exchange with stearyltrimethyl ammonium chloride, the d_{001} -spacing becoming 1.84 nm which also correspond to $2\theta = 3.9^\circ$. This implied that, the stearyltrimethyl ammonium chloride intercalated the clay galleries.

López-Manchado *et al*, (2003), reported the modification of Na^+ bentonite with octadecylamine, which increased the interlaminar spacing and the hydrophobic character of the clay. The sodium cations of bentonite were ion exchanged for the quaternary ammonium salt into the silicate galleries. X-ray diffraction patterns of the pristine clay and organoclay showed a characteristic diffraction peak at $2\theta = 7^\circ$ which is assigned to the interlayer platelet spacing (001 diffraction peak) of bentonite, with a spacing of 12.6 Å. When the intercalating reagent (octadecylamine) was added, a displacement of the peak to lower angles was observed at $2\theta = 5^\circ$, which, was deduced by the Bragg law equation. It therefore corresponds to an interlayer distance of 17.6 Å. They therefore, inferred that, octadecylamine behaved as an effective intercalating agent, which delaminated the bentonite. Additionally, FTIR spectra of Na^+ -bentonite and organoclay showed

two peaks of Na⁺-bentonite and three for the organoclay respectively. A strong absorption band at 969 cm⁻¹ observed was corresponding to the Si—O stretching vibrations of the silicate. A weak band observed at 1633 cm⁻¹ was assigned to the deformation vibrations of the interlayer water of the bentonite clay. Meanwhile, the three peaks appearing in the FTIR spectrum of the organoclay, were 2919 and 2850 cm⁻¹ bands, attributed to the C—H asymmetric and symmetric stretching vibrations of octadecylamine, respectively and a band at 1467 cm⁻¹ corresponding to the ammonium salt. These results further indicated that the ammonium salt has been incorporated within the silicate layers.

Work done by Nantana *et al*, (2004), showed organophylic montmorillonite prepared by a cation exchange process of interaction between Na⁺ ions of montmorillonite and ammonium salt of octadecylamine. Fourier-transform infrared spectrometry (FT-IR) and X-ray diffractometry profiles showed organophylic characteristics in modified montmorillonite with interlayer spacing increasing by twice of magnitude relative to unmodified montmorillonite, as calculated d-spacing from Bragg's law for the modified clay was 31.1 Å at 2θ=2.84 compared to that of the unmodified clay with d-spacing of 12.44 Å at 2θ=7.1. They inferred that, octadecylamine was effective in intercalation of the montmorillonite clay, making the clay potential to exfoliate in a polymer matrix.

Zheng *et al*, (2004) reported the preparation of three separate organo montmorillonite clays, with distearyldimethyl ammonium salt, octadecyltrimethyl ammonium salt, and hexadecyltrimethyl ammonium, as surfactants. X-ray diffraction profile of the three compared with unmodified montmorillonite showed an increase in the d-spacing of the modified clay samples, of value 4.2 nm, 2.7 nm, 1.8 nm for the various surfactants used respectively. As such, long chain carbon

content of surfactant influence intercalation of the clay galleries. This makes the organoclay more favorable to exfoliation in polymer matrix.

Roelofs *et al*, (2006), prepared organoclay from synthetic, Zn-stevensite, modified and intercalated with dimethyl octadecylammonium cations. The clay mineral was of high crystallinity with a low stacking number, which facilitated exfoliation in polymers like PP and PE, as confirmed in X-ray diffractometry and transmission electron microgram.

Work done by Keun-byoung *et al*, (2007), modified Sodium montmorillonite (Na-MMT) with oligomeric polyoxypropylene amine derivatives as well as simple amines by a cation exchange process. Commercially modified MMTs, Cloisites, were also analyzed in detail. The modifier content in organoamine modified-MMT (OA-MMT) as determined by thermo gravimetric Analysis was found to be 4–40 wt% and dependent on the structure of the modifier. The basal spacing of OA-MMT was strongly dependent on the structure and amount of the modifier. With the polyoxypropylenediamine of molecular mass 2000, the basal spacing of OA-MMT was enlarged up to 45.3 Å.

Salawudeen *et al*, (2008), also reported the preparation of organically modified bentonite. The organophilic clay prepared by ion exchange process using Octadecylamine as modifying agent was examined for physical, chemical and thermal properties. The specific gravity of the modified clay reduced after modification. This was due to the organic compounds attachment to the clay surfaces. The FT-IR showed clearly that the magnesium cations in the clay had been exchanged for alkylammonium ions and hence makes the clay more organophilic or less hydrophilic. This is evident in the FT-IR peaks analysis that showed the presence of functional groups like alkyl

group (-CH₃), halo alkyl group (-CH₃-Cl-) and some silicon based esters (R-O-Si-O) in the modified clay. The thermal stability of the clay modified with alkylammonium salts such as octadecylamine was not affected once the residual free ammonium salts was avoided. This was confirmed in thermo gravimetric Analytical plots of both pure unmodified and organically modified clay that attained stability at a temperature between 500 °C and 900 °C after loss in weight due to evaporation of moisture and decomposition of the adhered alkylammonium salts between 30 °C and 500 °C.

KNUST

Amanda *et al*, (2009), also prepared organophilic montmorillonite with Dodigen, Genamin salts and Cetremide salt. X-ray patterns of the unmodified clay, and organoclay (OMMT) showed a peak at basal distance of $d_{001} = 12.74 \text{ \AA}$ for the unmodified clay. The interlayer spacing for the treated sample with three quaternary ammonium salts obtained from the corresponding XRD patterns is 23.72 \AA (OMMT-Dod), 22.34 \AA (OMMT-Gen) and 21.41 \AA (OMMT-Cet), respectively. The interlayer distance was determined by the diffraction peak in the X-ray method, using the Bragg equation. The results indicated that the quaternary ammonium salts were intercalated between the basal planes of clay, leading to an expansion of the interlayer spacing, that is, the treatment with the quaternary ammonium salts was efficient and increase the d_{001} spacing.

Organophilic clays prepared are subsequently dispersed in polymer matrices to form the polymer/clay nanocomposites. Several works have been reported on the different routes to the formation of these nanocomposites with different polymer matrices.

Wang *et al.*, (2003), employed Static melt-intercalation to prepare s-PS/imidazolium-MMT nanocomposites. The syndiotactic polystyrene (s-PS) dried powder and organically treated layered silicate were mixed and ground together in a mortar and pestle. The mixed powder was heated at 290 °C for 8 h in a vacuum oven. The material was stirred once halfway through the melt-intercalation process. At 5 wt% organoclay loading, an X-ray diffractogram showed an increased interlayer distance of about 3.14 nm, of the organoclay, which indicates the development of a miscible s-PS/MMT hybrid structure. Transmission Electron Micrograph pictures also confirmed a periodically stacked clay particles at about 3–3.5 nm, consistent with the value corresponding to the intercalated XRD peak. It was then concluded that, that high-shear-rate processing, such as twin-screw extrusion, was not necessary for the formation of s-PS/MMT nanocomposites.

Dhruba *et al.*, (2011), investigation reported the preparation of tailor made poly (2-ethylhexyl acrylate) (PEHA) prepared by in-situ living radical polymerization in the presence of layered silicates and characterization of this polymer/clay nanocomposite. 2-Ethylhexyl acrylate was polymerized at 90°C using CuBr and Cu(0) as catalyst in combination with N,N,N',N'',N'''-pentamethyl diethylenetriamine (PMDETA) as ligand. Polymer/clay interaction was studied by Fourier Transform Infrared spectrometry and wide-angle X-ray diffraction analyses. Distribution of clay in the polymer matrix was studied by the transmission electron microscopy. They reported an increase in the rate of polymerization when nanoclay was added to the polymerization system. The optimum polymerization rate was obtained at 2 wt% nanoclay loading. The PEHA/clay nanocomposites had intercalated morphology as evidenced by wide angle X-ray diffractogram and transmission electron microscopic studies.

Cunyue *et al*, (2002), prepared polyethylene/montmorillonite nanocomposite by in situ copolymerization. The catalyst $\{[(2\text{-ArN}=\text{C}(\text{Me}))_2\text{C}_5\text{H}_3\text{N}]\text{FeCl}_2\}$ (Ar = C₆H₄(i-Pr)) with methylaluminoxane (MAO) as cocatalyst was intercalated between layers of montmorillonite (MMT) for ethylene oligomerization. Metallocene catalyst Me₂Si(Ind)₂ZrCl₂ and MAO was then added to form a dual functional catalytic system. A Polyethylene/montmorillonite nanocomposite was prepared by copolymerization of ethylene with α -olefins produced in situ from ethylene over the dual functional catalytic system. The catalytic system was of high polymeric activity. The resultant PE/MMT nanocomposite had the clay particles partially exfoliated at 30% clay loadings,

Araújo *et al*, (2007), prepared nanocomposites containing polyethylene (PE) and montmorillonite clay organically modified (OMMT) with quaternary ammonium salts by direct melt intercalation. A montmorillonite sample from the Brazilian state of Paraíba was treated with four different types of quaternary ammonium salts was used. After the treatment, the powder was characterized by X-ray diffraction and scanning electron microscopy. The dispersion and morphologies of OMMT within PE were investigated by X-ray diffraction and transmission electron microscopy. The results revealed the formation of intercalated montmorillonite layers in the PE matrix. The thermal stability and flammability of the PE/montmorillonite clay nanocomposites were measured by thermogravimetry and horizontal burning tests for HB classification, Underwrites Laboratories (UL 94), respectively. It was reported that the samples do not degrade at the processing temperature. By adding only 3 wt% montmorillonite, the burning rate of the nanocomposites was reduced by 17%, and tensile test showed that the yield strength and modulus of the nanocomposites were close to the pure PE.

Yixiang *et al*, (2006), prepared nanocomposites of chitosan and nanoclays (MMT-Na⁺ and Cloisite 30B) by solvent casting. The structural properties, thermal behaviors, and mechanical properties were characterized using X-ray diffraction (XRD), transmission electron microscopy (TEM), atomic force microscopy, differential scanning calorimetry, thermogravimetry analyses, and an Instron universal testing machine. XRD and TEM results indicated that an exfoliated structure was formed with addition of small amounts of MMT-Na⁺ to the chitosan matrix. Intercalation along with some exfoliation occurred with up to 5 wt % MMT-Na⁺.

Wentao *et al*, (2004), synthesized, poly(ethylene terephthalate) (PET)/silica nanocomposites by direct polymerizing PET monomer dispersed with organic modified silica nanoparticles. The characteristics and properties of these nanocomposites were investigated by the transmission electron microscopy, differential scanning calorimetry, and thermogravimetric analysis, respectively. Results obtained showed that, the nanoparticles have been well dispersed in the polymer matrix (exfoliated), the addition of nanoparticles can speed up the crystallization and melting point, and last but not least, the addition has no significant effect on the synthesis process.

Jin *et al*, (2002), successfully prepared Polyethylene/montmorillonite nanocomposites by performing in-situ Ziegler-Natta polymerizations of ethylene using montmorillonite (MMT-OH) modified with intercalation agents containing hydroxyl groups. Hydroxyl groups in intercalation agents offered facile reactive sites for anchoring catalysts in between silicate layers. Wide interlayer distance and abundant hydroxyl groups of MMT-OH facilitated the fixation of TiCl₄ / Et₃Al inside the interlayer space, and subsequent polymerization induced a complete exfoliation

of the layered silicates in the polymer matrix, as confirmed by data from X-ray diffractometry and Transmission Electron microscopy.

Choi *et al*, (2003), prepared poly(hydroxybutyrate-co-hydroxyvalerate)(PHB/HV)/organoclay nanocomposites by a melt intercalation method using Cloisite 30B as the organoclay. An intercalated structure was formed due to the strong hydrogen bond interaction between PHB/HV and the organoclay. The nanodispersed organoclay increased both the temperature and rate of crystallization of PHB/HV, indicating that the organoclay was an effective nucleating agent in the polymer matrix.

Mishra *et al*, (2003) successfully prepared new millable polyurethane/organoclay nanocomposites. The WAXD results of the nanocomposites showed a shift in the peak position with reduced intensity in comparison to the organoclay, suggesting thereby the intercalation of the polymer inside the silicate layer.

Morgan *et al*, (2001), successfully synthesize Polyetherimide (PEI) nanocomposites using montmorillonite treated with n-dodecylamine ammonium salt (MMT-C12), and montmorillonite treated with 12-aminododecanoic acid ammonium salt (MMT-C12Acid), by an in situ solution polymerization approach. Using TEM and XRD to analyze these materials revealed two nanocomposites whose exact dispersion could not be accurately described by XRD alone. While XRD showed no d spacing increase for the PEI-1/MMT-C12 nanocomposite, TEM showed exfoliated single clay layers and some undispersed multilayer clay tactoids (particles). Combining the observations from TEM and XRD indicated that the PEI 1/MMT-C12 was an exfoliated immiscible nanocomposite. Meanwhile, the MMT-C12Acid/PEI 1 nanocomposite,

XRD observed an increase in d-spacing, indicating an intercalated nanocomposite. However, when this datum was combined with the TEM images, the MMT-C12Acid/PEI 1 nanocomposite was shown to be an exfoliated-intercalated nanocomposite.

Zhao *et al*, (2004), prepared Polyethylene–clay nanocomposites by melt compounding.

Na-montmorillonite clay was modified by trimethylchlorosilane. Wide angle X-ray diffraction (WAXD) and transmission electron microscopy (TEM) showed that intercalated nanocomposites were formed.

2.1. Theoretical Considerations of Experimental Methods

Experimental methods that are commonly employed in the characterization of raw clay, modified clay, and the Polymer/clay nanocomposite include; cation exchange capacity process, X-ray diffractometry, X-ray fluorescence spectroscopy, Fourier transform infra-red spectroscopy and Cross-linking measurements.

2.1.1. Cation Exchange Capacity

Cation exchange capacity (CEC) of clay refers to the amount of positively charged ions a clay sample can attract, retain, and exchange. Examples of positively charged ions (cations) include: calcium (Ca^{2+}), magnesium (Mg^{2+}), potassium (K^+), sodium (Na^+), and ammonium (NH_4^+). It is reported in millequivalents per 100 grams of clay (meq/100g). Clays have a slight negative charge due to the isomorphic substitution (the replacement of one atom by another of similar size in a crystal lattice during crystal growth without changing the crystal structure) between Al^{3+} and Si^{2+} ions and Al^{3+} and Mg^{2+} ions. Standard ammonium acetate method is used in estimating the cation exchange capacity of clay (Camberato, 2001).

The cation exchange capacity (CEC) of clay is determined by leaching the clay with a chosen electrolyte so as to replace all existing cations by one particular cation. The clay is filtered, rinsed to free excess electrolyte and the amount of chosen cation determined. Cation exchange capacity (CEC) of the chosen electrolyte is calculated as below.

$$\text{CEC} \left(\frac{\text{meq}}{100 \text{ g}} \right) \text{ of clay} = \frac{10 \times \text{cation concentration}}{\text{Mass of clay}} \text{-----} (2.1)$$

Other electrolytes are also used and their cation exchange capacity (CEC) also computed.

The cation exchange capacity (CEC) for the clay is evaluated from the sum of the cation exchange capacity of the various chosen electrolytes used (Hess, 1994).

2.1.2. X-ray Diffractometry

The three-dimensional structure of **non-amorphous** materials is defined by regular, repeating planes of atoms that form a crystal lattice. When a focused X-ray beam interacts with these planes of atoms, part of the beam is transmitted, part is absorbed by the **sample**, part is refracted and scattered, and part is diffracted. X-rays are diffracted by each mineral differently, depending on what atoms make up the crystal lattice and how these atoms are arranged. In X-ray powder diffractometry, X-rays are **generated within a sealed tube** that is under vacuum. A current is applied that heats a filament within the tube, the higher the current the greater the number of electrons emitted from the filament. A high voltage, typically 15-60 kV, is applied within the tube. This high voltage accelerates the electrons, which then hit a target, commonly made of copper. When these electrons hit the target, X-rays are produced. The wavelength of the X-ray is characteristic of the target. These X-rays are collimated and directed onto the sample, which has been ground to a fine powder. A detector detects the X-ray signal; the signal is then processed either by a microprocessor or electronically, converting the signal to a count rate. Changing the angle between the X-ray source, the sample, and the detector at a controlled rate between preset

limits is an X-ray scan (Flohr, 1997). Figure 2.1 shows the major components of an X-ray diffractometer.

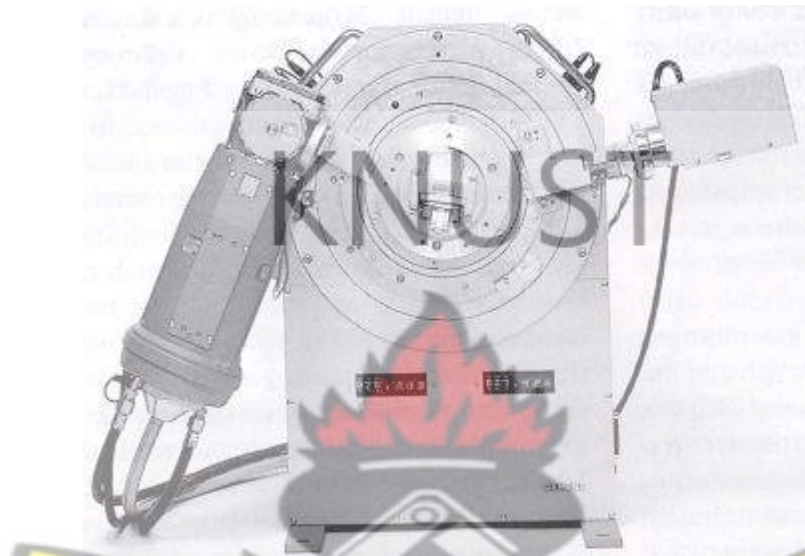


Figure 2.1: X-ray diffractometer set-up (Flohr, 1997).

When an X-ray beam hits a sample and is diffracted, we can measure the distances between the planes of the atoms that constitutes the sample by applying Bragg's Law. Bragg's law is given by the equation;

$$n \lambda = 2 d \sin \theta \text{ ----- (2.2)}$$

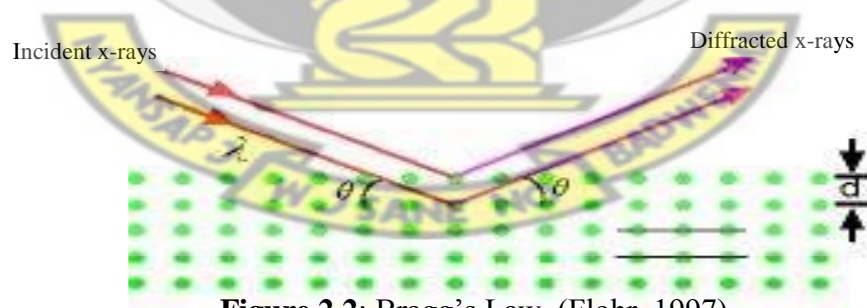


Figure 2.2: Bragg's Law, (Flohr, 1997)

where the integer n is the order of the diffracted beam, an integer, λ is the wavelength of the incident X-ray beam, d is the distance between adjacent planes of atoms (the d -spacings), and θ is the angle of incidence of the X-ray beam. Since we know λ and we can measure θ , we can calculate the d -spacings. The geometry of an XRD unit is designed to accommodate this

measurement (figure 2.2). The characteristic set of d -spacings generated in a typical X-ray scan provides a unique "fingerprint" of the mineral or minerals present in the sample. When properly interpreted, by comparison with standard reference patterns and measurements, this "fingerprint" allows for identification of the material (Flohr, 1997).

If the diffracting specimen is stress free, the average particle size in the specimen is also evaluated using Scherrer's equation:

$$t = \frac{(0.9\lambda)}{(B \cos \theta)} \dots\dots (2.3)$$

where:

t = Average particle size in the specimen

λ = Wavelength of X-ray radiation

B = Angular width of the extent of broadening of diffraction peaks of the diffractograms measured at half the maximum intensity in radians

θ = Diffracting angle. (Callister, 2007).

2.1.3 X-ray Fluorescence

X-ray fluorescence (XRF) spectrometry is an elemental analysis technique with broad application in science and industry. XRF is based on the principle that individual atoms, when excited by an external energy source, emit X-ray photons of a characteristic energy or wavelength. By counting the number of photons of each energy emitted from a sample, the elements present may be identified and quantitated (Jenkins *et al*, 2000).

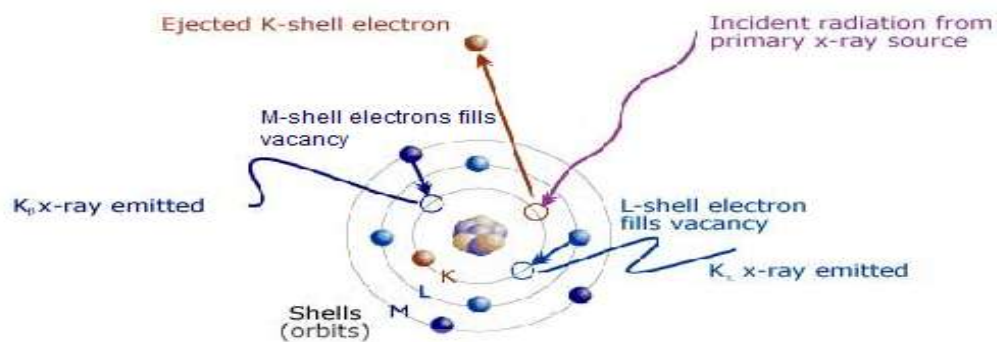


Figure 2.3: X-ray fluorescence in a schematic representation (Jenkins *et al*, 2000).

When a primary X-ray excitation source from an X-ray tube or a radioactive source strikes a sample, the X-ray can either be absorbed by the atom or scattered through the material. The process in which an X-ray is absorbed by the atom by transferring all of its energy to an innermost electron is called the “photoelectric effect.” During this process, if the primary X-ray had sufficient energy, electrons are ejected from the inner shells, creating vacancies. These vacancies present an unstable condition for the atom. As the atom returns to its stable condition, electrons from the outer shells are transferred to the inner shells and in the process giving off a characteristic X-ray. The emitted X-rays produced from this process are called “X-ray fluorescence,” or XRF. Detecting this photon and measuring its energy allows us to determine the element and specific electronic transition from which it originated. Herein lies the basis for XRF spectrometry, where elements are quantitated based on the rate of emission of their characteristic X-rays from a sample that is being excited. The process of detecting and analyzing the emitted X-rays is called “X-ray fluorescence analysis”. In most cases the innermost K and L shells are involved in XRF detection (Jenkins *et al*, 2000).

Samples prepared for XRF are usually in the form of flat 32 mm disks. Most solid samples can be ground and pressed into pellets. A general rule of thumb is that XRF probes only a depth of 100 μm for most sample matrices. The most common method of sample preparation is pelletizing, which can be made to work for most matrices that can be ground into a homogeneous powder, including soil, minerals, and dried organic matrices such as tissues or leaves. Normally difficult grinding is accomplished with a hard agate mortar and pestle but many samples can be adequately homogenized by placing into a hard plastic vial, adding a plastic mixing ball, and violently shaking in a mixer mill. A powdery binder containing cellulose, starch, polyvinyl alcohol or other organics is usually weighed and blended thoroughly with the sample, and the resulting mixture added to a deformable aluminum cup. The sample and cup are pressed in a cylindrical die to form a supported pellet which ideally has a smooth, homogeneous sample surface and good physical stability (Buhrke *et al.*, 1998). It is analyzed in an XRF spectrometer thereafter.

2.1.4 Fourier Transform – Infrared Spectroscopy

Fourier transform infrared (FTIR) spectroscopy is an analysis technique that provides information regarding the molecular structure and chemical bonding of materials. These materials can be organic or inorganic. The infrared region of the electromagnetic spectrum (Figure 2.4) is divided into three regions: the near-, mid-, and far-IR (Figure 2.5). The mid-IR ($400\text{-}4000\text{ cm}^{-1}$) is the most commonly used region for analysis as all molecules possess characteristic absorbance frequencies and primary molecular vibrations in this range.

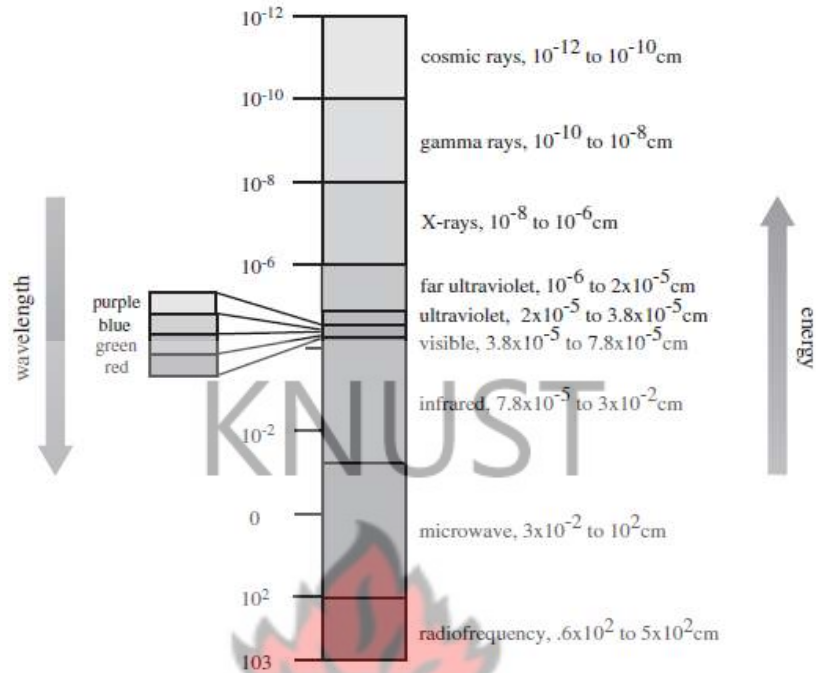


Figure 2.4: The Electromagnetic Spectrum (Szymanski *et al*, 1970).

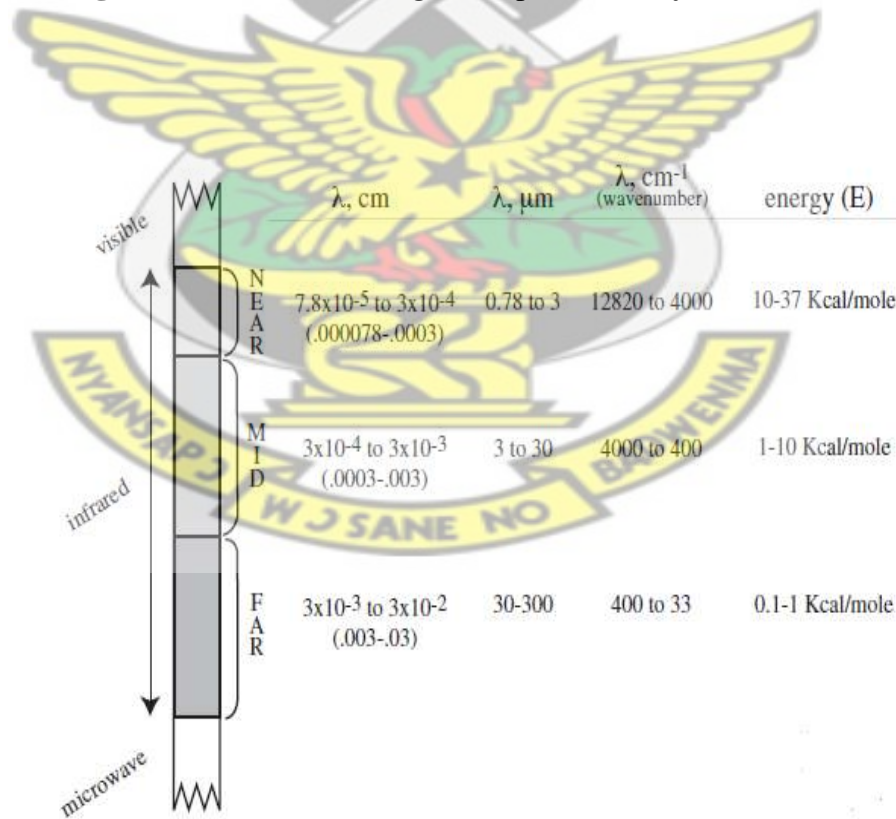


Figure 2.5: The Infrared Region of the Electromagnetic Spectrum (Szymanski *et al*, 1970).

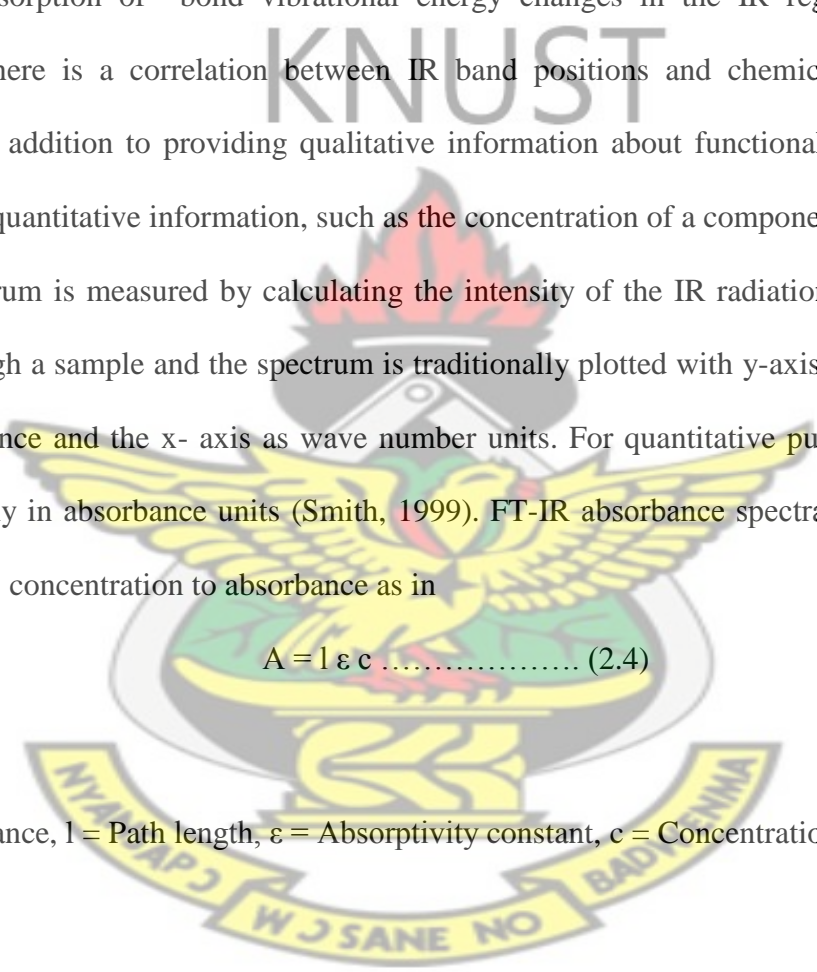
Mid-infrared spectroscopy methods are based on studying the interaction of infrared radiation with samples. As IR radiation is passed through a sample, specific wavelengths are absorbed causing the chemical bonds in the material to undergo vibrations such as stretching, contracting, and bending. Functional groups present in a molecule tend to absorb IR radiation in the same wave number range, regardless of other structures in the molecule, and spectral peaks are derived from the absorption of bond vibrational energy changes in the IR region (Smith, 1996). Therefore, there is a correlation between IR band positions and chemical structures in the molecule. In addition to providing qualitative information about functional groups, IR spectra can provide quantitative information, such as the concentration of a component in a sample.

An IR spectrum is measured by calculating the intensity of the IR radiation before and after it passes through a sample and the spectrum is traditionally plotted with y-axis units as absorbance or transmittance and the x-axis as wave number units. For quantitative purposes the spectrum plot is usually in absorbance units (Smith, 1999). FT-IR absorbance spectra follow Beer's law, which relates concentration to absorbance as in

$$A = l \epsilon c \dots\dots\dots (2.4)$$

Where

A = Absorbance, l = Path length, ϵ = Absorptivity constant, c = Concentration



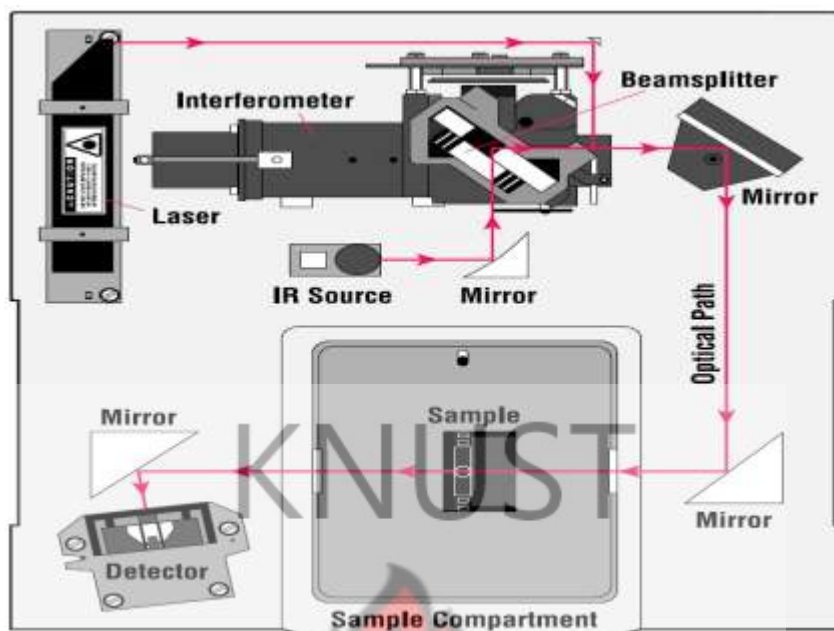


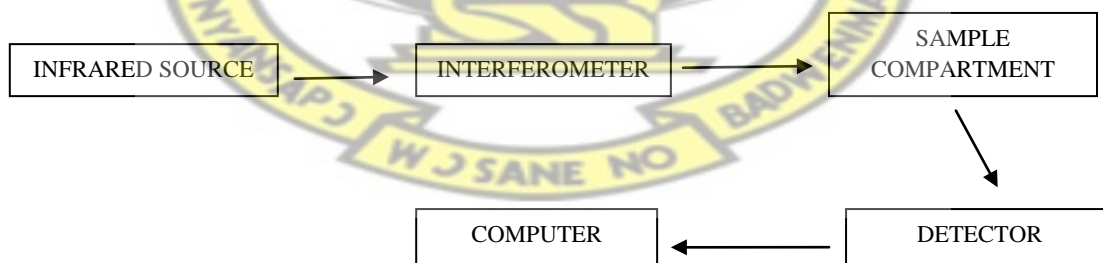
Figure 2.6: A simple FT-IR spectrometer layout (Smith, 1999).

A general schematic diagram of an FT-IR spectrometer is presented in Figure 2.6 above. The IR source emits radiation that is passed through an interferometer, usually a Michelson interferometer with a beam splitter, a fixed mirror, and a moving mirror. The interferometer uses interference patterns to make accurate measurements of the wavelength of light. When IR radiation is passed through a sample, some radiation is absorbed and the rest is transmitted to the detector. The detector measures the total interferogram from all the different IR wavelengths. A mathematical function called Fourier transform converts the interferogram (intensity versus time spectrum) to an IR spectrum (intensity versus frequency spectrum) (Smith, 1999).

Almost any solid, liquid or gas sample can be analyzed. Many sampling accessories are available. Approximately 50 to 200 mg of solids is desirable, but 10 μg ground with transparent matrix (such as KBr) is the minimum for qualitative determinations; 1 to 10 μg minimum is required if solid is soluble in suitable solvent. 0.5 μL of liquid is needed if neat, less if pure. Approximately 50 ppb of gases is needed. During preparation dry solids are ground into KBr

matrix or dissolved in a suitable solvent (preferably, CCl_4 and CS_2 solvents). Estimated time to obtain spectrum for a routine sample varies from 1 to 10 min depending on the type of instrument and the resolution required. Most samples can be prepared for infrared (IR) analysis in approximately 1 to 5 min (Coleman, 1993).

The instrumental process of FT-IR spectroscopy involves, the Source, which generates Infrared energy from a glowing black-body source. This beam passes through an aperture which controls the amount of energy presented to the sample. IR Beam from the source enters the interferometer where the “spectral encoding” takes place. The resulting interferogram signal then exits the interferometer to the sample compartment. Here it is transmitted through or reflected off of the surface of the sample, depending on the type of analysis being accomplished. In the samples compartment, specific frequencies of energy, which are uniquely characteristic of the sample, are absorbed. The beam finally passes to the detector for final measurement. Detectors used are specially designed to measure the special interferogram signal. Measured signal is digitized and sent to the computer where Fourier transformation takes place. Final infrared spectrum is then presented to user for interpretation and any further manipulation (Coleman, 1993).



Scheme 1: Instrumental Process in sample analysis by an FT-IR spectrometer.

2.1.5 Polymer Crosslinking Measurements

Covalent chemical bonds that occur between macromolecules are known as crosslinks. Their presence and density have a profound influence on both the chemical, morphological and mechanical properties of the materials in which they occur. The presence of crosslinks between macromolecules influences the way in which these materials respond to heat. Uncrosslinked thermoplastic polymers will generally melt and flow at sufficiently high temperatures. On the contrast, crosslinked polymers cannot melt at elevated temperatures due to the constraints on molecular motions introduced by the crosslinks. Instead, at temperatures well above those at which thermoplastics typically melt, they begin to undergo irreversible degradation (Billmeyer, 1984).

Response to heat is not the only difference in chemical behaviour between crosslinked and uncrosslinked polymers. Dissolution behaviour is also different since this, too, depends on the nature and extent of any inter-chain covalent bonds. An uncrosslinked polymer will usually dissolve in an appropriate solvent. The process may well be lengthy, but given sufficient time and adequate polymer-solvent compatibility, the polymer will dissolve. By contrast, crosslinked polymers will not dissolve. Solvation of chain segments cannot overcome the effect of the covalent bonds between the macromolecules; hence crosslinked molecules cannot be carried off into the solution. Depending on the crosslink density, however, such materials may admit significant amounts of solvent, becoming softer and swollen as they do so. Such swelling by fairly lightly crosslinked materials is generally reversible and, given appropriate conditions, solvent that has entered a crosslinked structure can be removed and the polymer returned to its original size, Therefore swelling index measurements of polymeric material leads to estimation of degree of crosslinking (Nicholson, 1994).

Crosslinks do exist in the polymers from polymerization processes or thermally introduced into them by crosslinking agents as Clay, Sulphur or Sodium Borate (Na_3BO_3). Below is a scheme of the two cases.

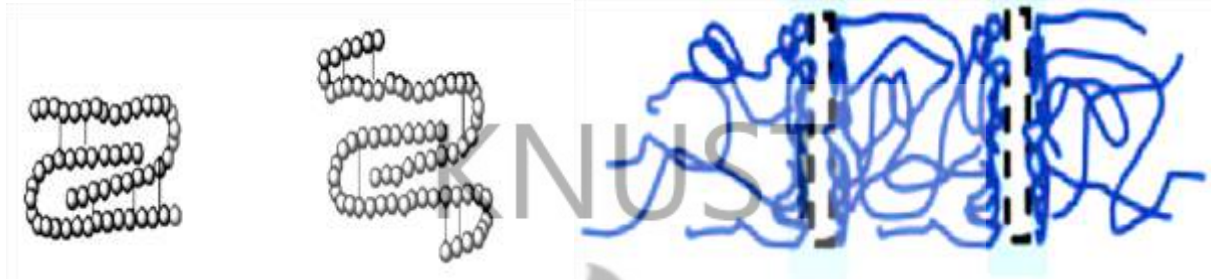
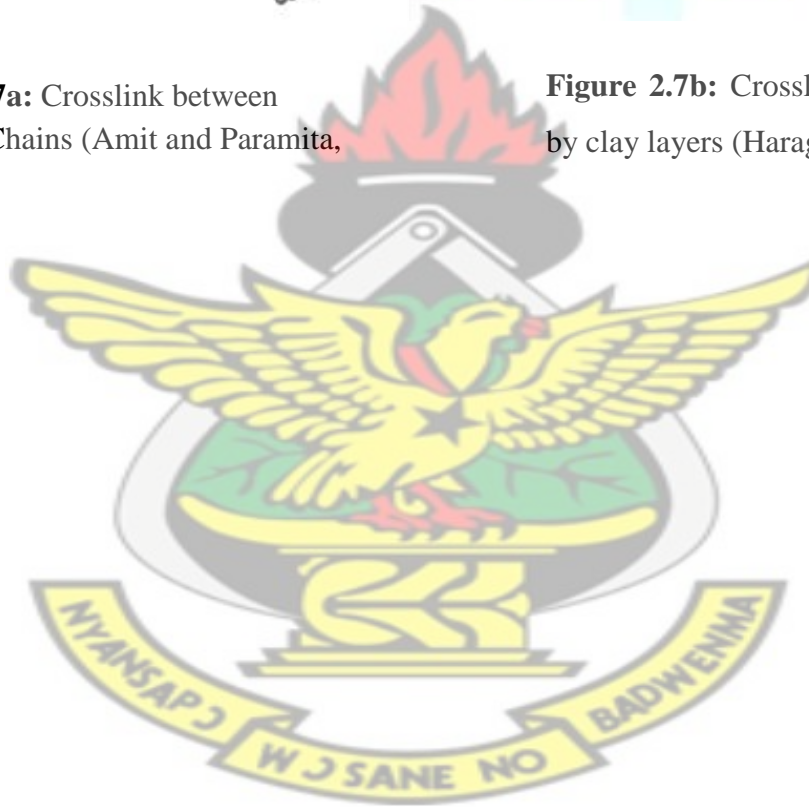


Figure 2.7a: Crosslink between Polymer Chains (Amit and Paramita, 2009).

Figure 2.7b: Crosslinking introduced by clay layers (Haraguchi, 2011).



CHAPTER THREE

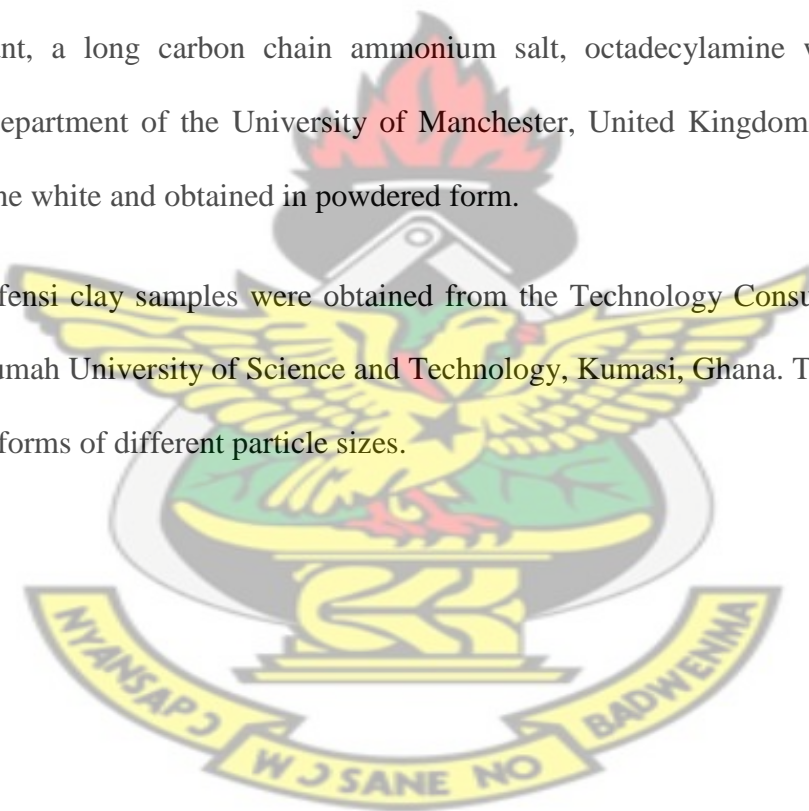
3.0 EXPERIMENTAL METHODS

3.1. Materials

Commercial low density polyethylene was donated by the School of Material Science, University of Manchester, United Kingdom. It is a product from ExxonMobil with a product number LDPE LD 650, a density of 0.914 g/cm^3 , and a glass transition temperature of $81.0 \text{ }^\circ\text{C}$. It was white in colour and obtained in pellet form.

The surfactant, a long carbon chain ammonium salt, octadecylamine was donated by the Chemistry Department of the University of Manchester, United Kingdom. The surfactant was fine crystalline white and obtained in powdered form.

Aferi and Mfensi clay samples were obtained from the Technology Consultancy Center of the Kwame Nkrumah University of Science and Technology, Kumasi, Ghana. They were obtained in dry granular forms of different particle sizes.



3.2 Samples Preparations

3.2.1 Clay Samples

Clay particles were dried at room temperature of 30 °C for 24 h and crashed in a porcelain mortar with a pestle. The ground clay particles were then sieved through a 150 μ mesh followed by 75 μ mesh. Samples were collected on an aluminium foil and stored in transparent polyethylene bags for further analysis. Below is a photograph of micron sieves as well as mortar and pestle used.

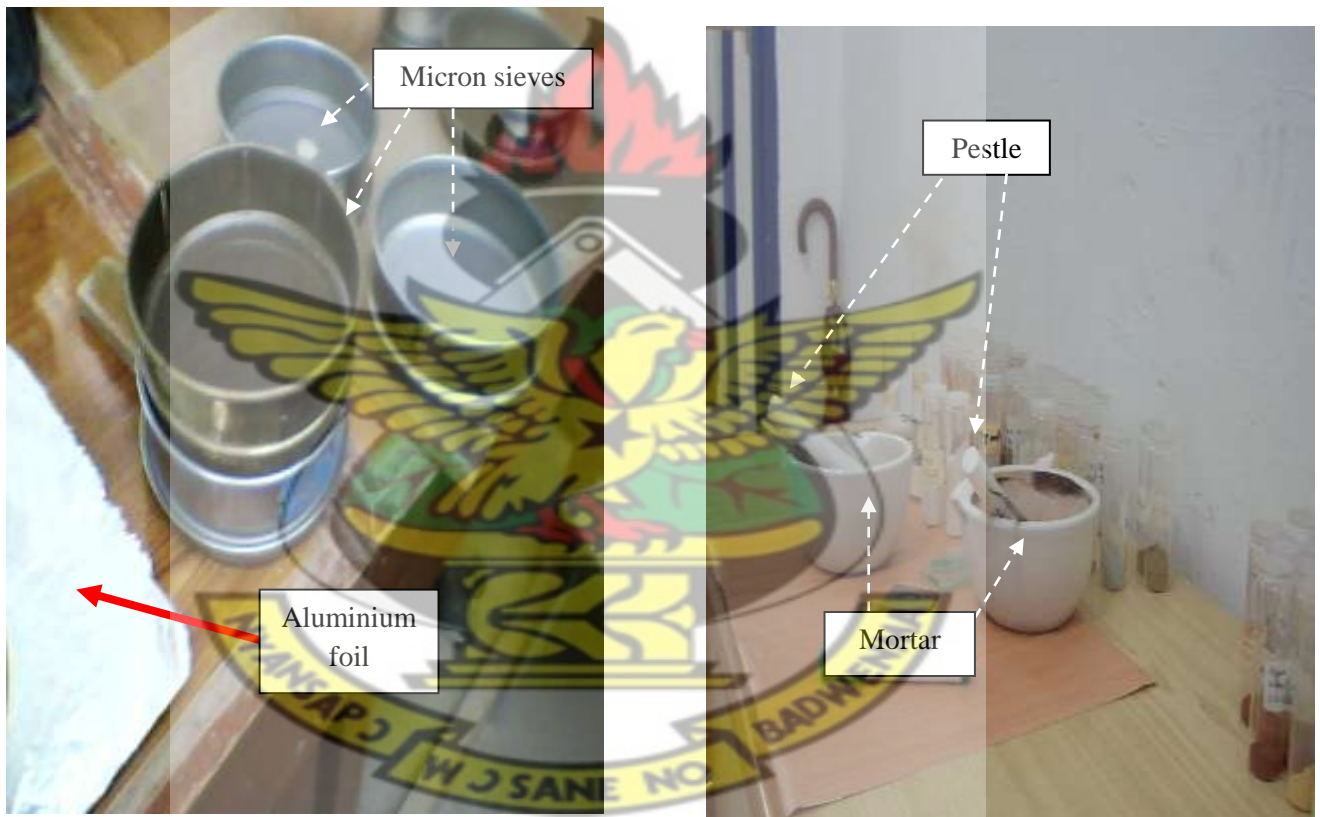


Figure 3.1a: Micron Sieves and Aluminium Foil.

Figure 3.1b: Mortar and Pestle

3.2.2 Modification of Clay Samples (Organoclay preparation)

2.5 g of prepared clay was dispersed in 100 ml distilled water at a temperature of 80 °C for five minutes and quickly transferred into a beaker containing 1.08 g of octadecylamine dissolved in 16.00 ml of 0.75M dilute solution of hydrochloric acid at 80 °C.

The mixture was stirred at 750 rpm for 30 min and allowed to settle for 20 min. A white gelatinous precipitate observed as the supernatant was gently decanted and the residue which is the organoclay thoroughly washed from any excess chlorine ions. The residue was air dried for 24 h and oven dried at 50 °C for 4 h.

Dry organoclay samples were ground and stored in sterilized plastic bottles for further analysis.

Figure 3 below are some photographs of the preparation of organoclay.

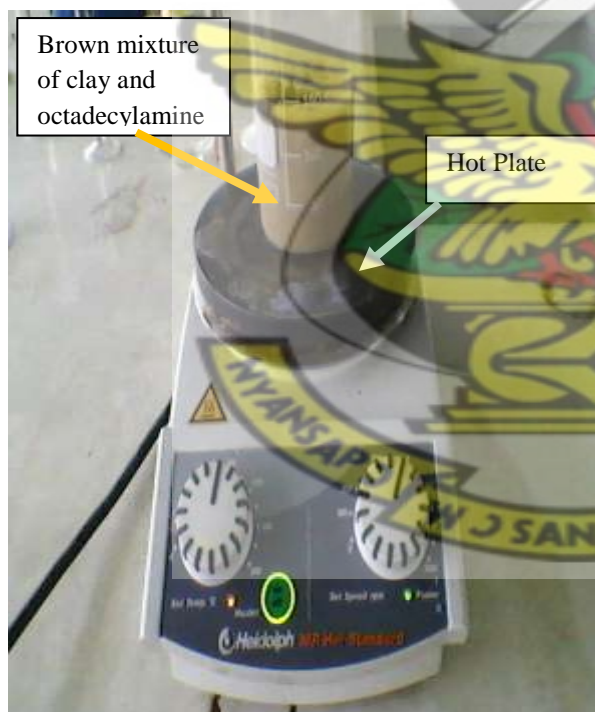


Figure 3.2a: Photograph of organoclay and octadecylamine mixture on a hot plate.

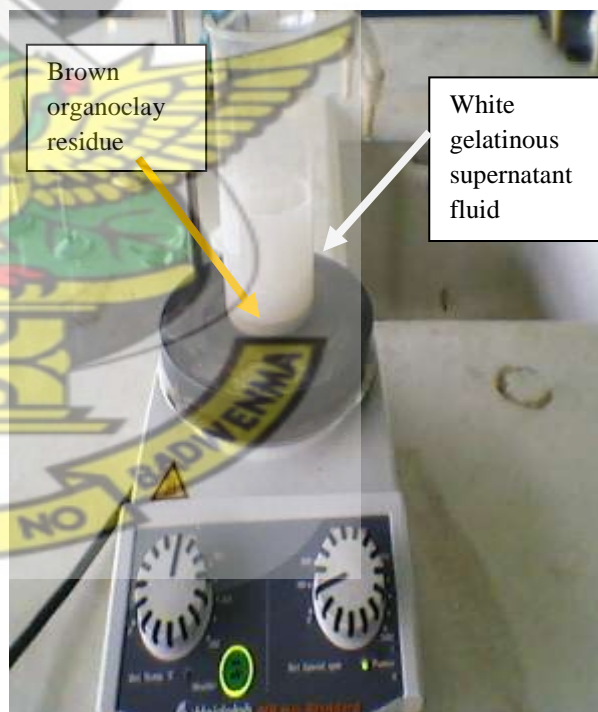


Figure 3.2b: Photograph of settled organoclay with a supernatant gelatinous white precipitate, on a hot plate.

3.2.3 Preparation of LDPE/Clay Nanocomposite

The melt mixing technique was employed. organoclay powder and LDPE pellets were pre-mixed in a 20 ml steel dish for 10 min and subsequently subjected to heating over a hot plate at a temperature of 80 °C with stirring. The molten material was annealed after 15 min of stirring at a temperature of 100 °C for 5 min. Annealing was employed to ensure a homogenous interaction between organoclay particles and the LDPE chains. Temperature was gradually reduced to 10 °C for 10 min and the prepared material picked with a clean spatula from the dish. 2 wt%, 4 wt%, 6 wt%, 8 wt%, and 10 wt% composition of clay to low density polyethylene were prepared.

The prepared materials were stored in plastic envelopes for further analysis.

Figure 3.3 below is a photograph of the LDPE/clay nanocomposite preparation set-up.

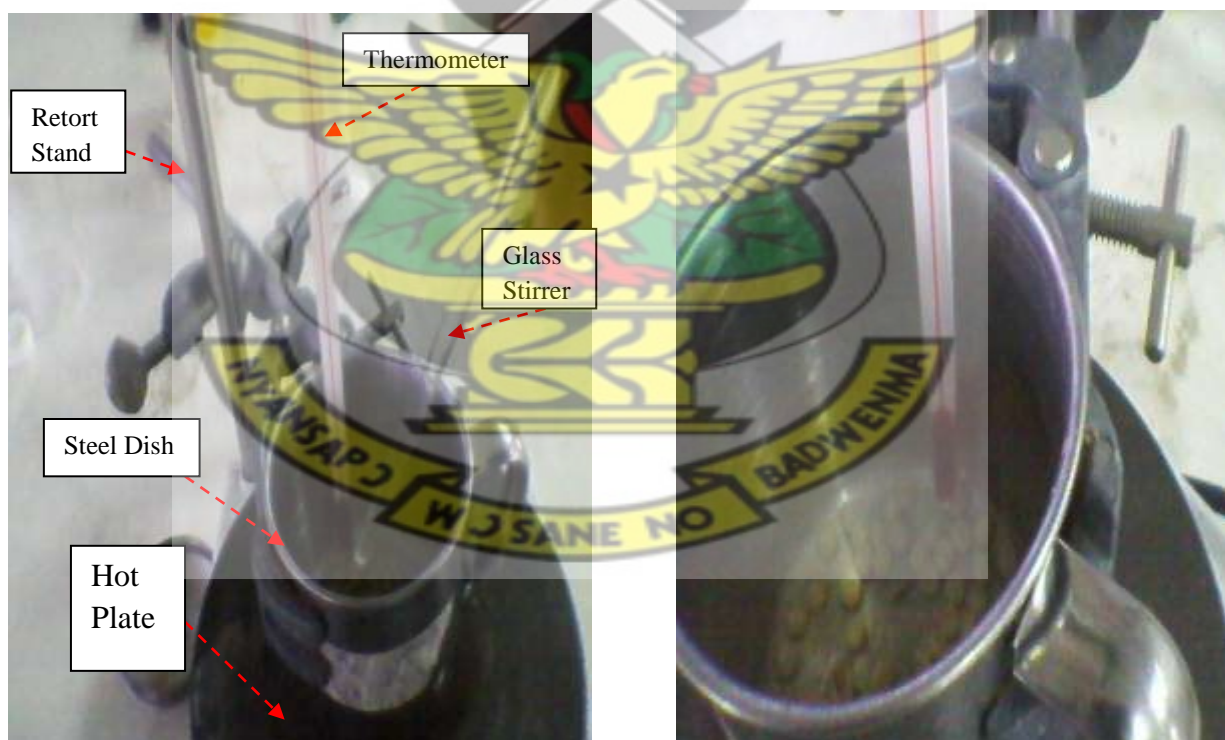


Figure 3.3: Photograph of Set-up for the preparation of LDPE/clay

3.2.4 LDPE/clay nanocomposite powder

Powdered form of the prepared material was obtained by grating them on an aluminium sheet. The aluminium sheet had nail-holes formed rough surface. Samples were collected on a clean white paper and stored in plastic envelopes for Characterization. Figure 3.4 below is a photographic representation of the grating process.

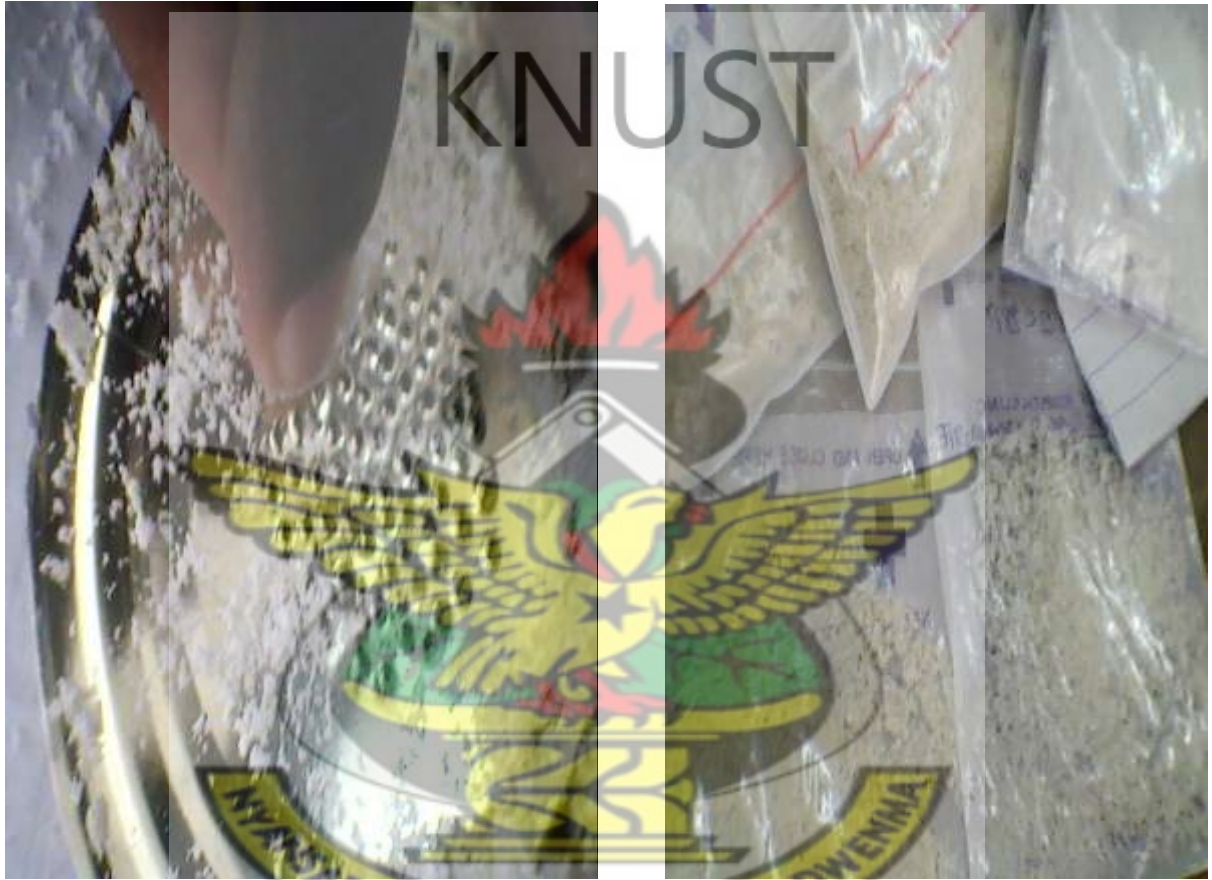


Figure 3.4a: Photograph of prepared nanocomposite being ground on a grater.

Figure 3.4b: Photograph of powdered nanocomposite in a plastic envelopes.

3.3 Characterization

3.3.1 Cation exchange capacity of pristine clay (raw clay)

5 g of the clay was weighed into a 50 cm³ centrifuge tube and 15 cm³ of sodium acetate solution added. The centrifuge tube was stoppered with a rubber stopper. It was then centrifuged at about 100 rps for about 5 min until the supernatant liquid was clear. The liquid was decanted and discarded. The centrifuging was repeated four times with fresh portions of the 15 cm³ sodium acetate solution. An amount of 15 cm³ of 95% ethanol was added to the clay in the centrifuge tube and the mixture was centrifuged and the ethanol decanted and discarded. The ethanol washing was repeated three more times.



Figure 3.5: Photograph of Flame Photometer Set-Up.

Finally, the clay was extracted with three 15 cm³ sodium acetate solution and the extract was collected in a 200 cm³ graduated flask. The extract was diluted to 100 cm³ with distilled water and the sodium concentration was determined by flame photometry. The cation exchange capacity for the sodium and hydrogen ions was then computed. This process was repeated with

15 cm³ for each of the solutions: magnesium acetate, potassium acetate, calcium acetate, and aluminum acetate. Mg²⁺, K, Ca²⁺ and Al³⁺ concentrations were then determined and their cation exchange capacity computed. The total cation exchange capacity of the clay was thereafter calculated.

3.3.2 X-ray fluorescence (XRF), analysis on pristine clay (raw clay)

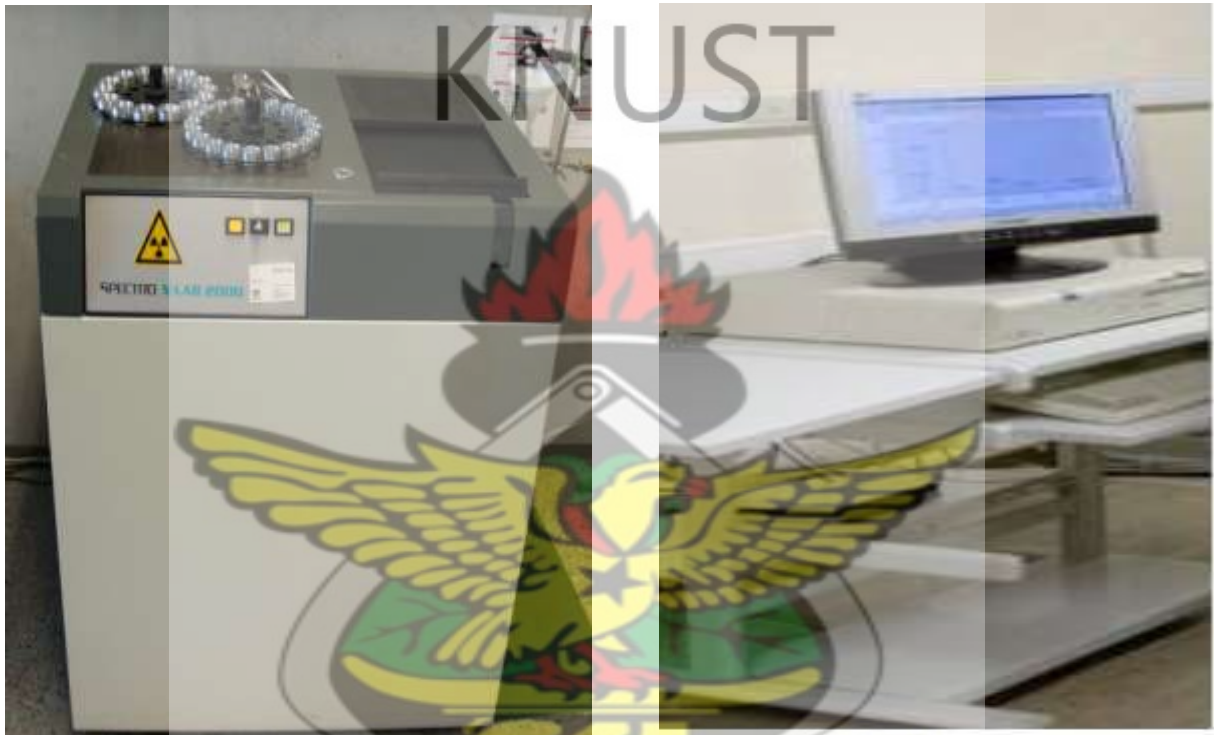


Figure 3.6: Photograph of SpectroX-lab, 2000 and a computer display set-up for XRF

X-ray fluorescence analysis was performed for very fine powder specimen of the pristine clay samples using SpectroX-Lab 2000 X-ray fluorescence spectrometer operated at 40 kV, 30 mA. 4 g of pristine (raw) clay was measured with an electronic chemical balance and placed in a metal die of diameter 2.5 cm. An amount of 0.9 g starch binder was mixed with the 4 g of the pristine clay in the metal die. The mixture was pressed in a metal screw to form a pellet of diameter 2.5 cm. The pellet was placed in a sample holder at an angle of 45° with respect to the source and detector of the X-ray fluorescence spectrometer. Samples were scanned. Elemental components

and their amounts were determined by comparing the scanned diffractograms with standard patterns.

3.3.3 Fourier Transform - Infra Red (FT-IR), spectroscopic analysis



Figure 3.7: Photograph of FT-IR Spectrometric Set-up.

The analysis was carried out on an Interspec200-X FT-IR Spectrometer. 20 μg of the sample and 200mg Potassium Bromide crystals were mixed and ground in a mortar and pestle, into very fine powdered form. They were gently transferred into a press to form a very thin transparent film with smooth surfaces. The thickness of the film was between 30-50 μm . It was vertically placed in a sample holder and analyzed. Spectrums obtained were saved on the computer for interpretation.

3.3.4 X-ray Diffractometric Measurements

The experiment was carried out on a Siemens-D5000 diffractometer with Cu K_α radiation at a wavelength, $\lambda = 0.15 \text{ nm}$ and a scanning rate of 2° per second from 10° to 80° . 2 g of powdered sample in the finest form was measured on an analytical balance and transferred unto the sample cell. It was then pressed with a smooth glass slide to obtain a uniform smooth surface. The cell was placed in the sample holder. A command issued on the computer inter-phase starts up the

scanning process. At a scanning rate of 2° from of 10° to 80° on the 2θ axis. It took 45 min to complete a single scan. Diffractograms were analyzed using the computer application software EVA and PowderX.



Figure 3.8a: Photograph of X-ray Diffractometer.



Figure 3.8b: Photograph of computer for data display and analysis.

3.3.5 Cross-linking density Test

0.2g of the nanocomposite was immersed in 10 ml of toluene solvent. The sample was allowed to swell in the toluene for 48 h in the dark. The nanocomposite was then placed on a dish lined with filter paper and turned over once to assist blotting. Weight of the dish and content was taken. The dish was emptied of the nanocomposite and its weight with the filter paper taken. Cross-linking density of the nanocomposite was calculated by taking the inverse of the Swelling Index.

$$\text{Swelling Index (SI)} = \frac{\text{weight of swollen gel}}{\text{weight of dry gel}} \quad \text{----- (3.1)}$$

CHAPTER FOUR

4 RESULTS AND DISCUSSIONS

4.1 Properties of clay samples

Table 4.1: A table showing some properties of clay samples.

Clay samples from	Properties					Amount of some XRF determined major oxides/ (%)
	Colour	Average particle size/(nm)	Cation exchange capacity/ (meq/100g)	d-spacing/ (nm)	pH	
Mfensi	Pale brown	5.54 (Table A.4.2)	9.87 (Appendix 1.2)	0.325 (Appendix 4)	5.78	SiO ₂ (74.49%), and Al ₂ O ₃ (15.77%). (Appendix 1.1)
Aferi	Deep brown	5.55 (Table A.4.3)	30.03 (Appendix 1.2)	0.322 (Appendix 4)	6.86	SiO ₂ (59.98%) and Al ₂ O ₃ (24.41%). (Appendix 1.1)

X-ray fluorescence determined major elements of Mfensi and Aferi clay samples were Si, Al, Fe, Mg, Na, Ca and Ti. They existed as oxides in the clay samples. Detailed proportions of these major elemental oxides and minor oxides are presented in Appendix 1. The clay samples have cation exchange capacities of 9.87 meq/100 g for Mfensi clay and 30.03 meq/100 g for Aferi clay. pH values of 5.78 for Mfensi clay and 6.86 for Aferi clay. Mfensi clay had an interplanar distance of 0.325 nm and that of Aferi clay was 0.322 nm. Calculated d-spacing is reported in Appendix 4.

4.2 FT-IR Characterization

4.2.1 FT-IR Spectra of Modified Mfensi clay compared to that of Pristine Mfensi clay

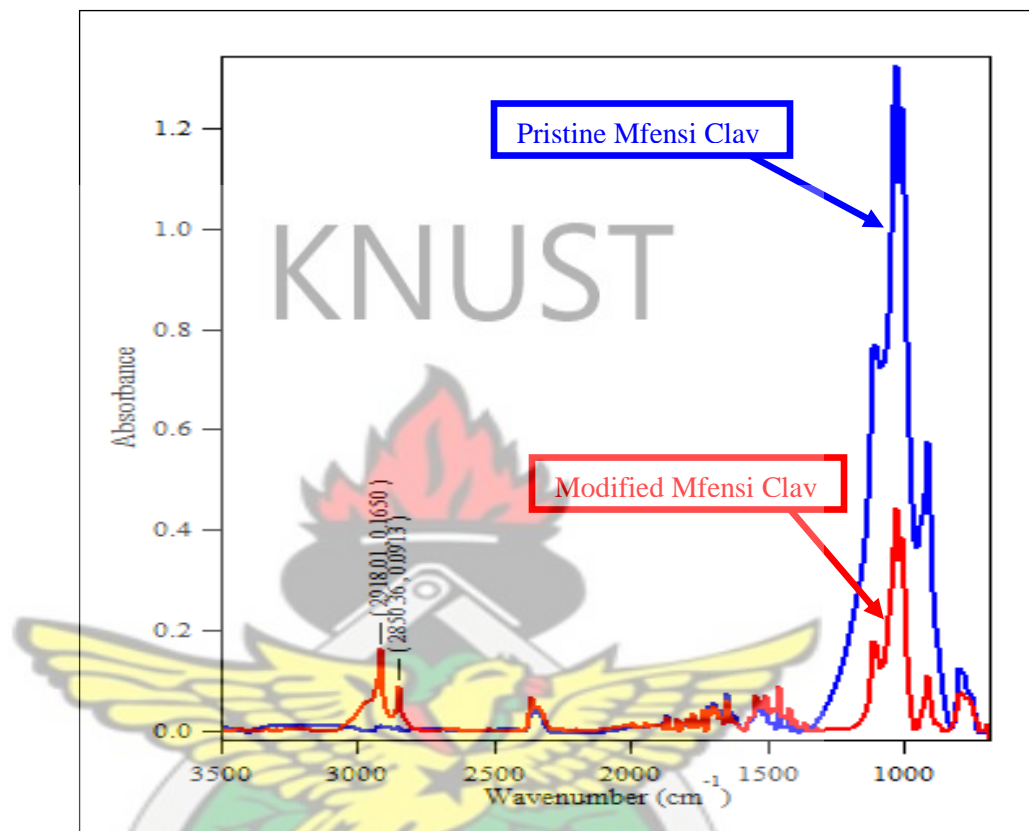


Figure 4.1: FT-IR Spectra of Modified Mfensi Clay compared to that of the Pristine Mfensi clay.

Stacked spectra of pristine (raw) Mfensi clay and the modified mfensi clay are compared in figure 4.1 above. Si-O vibration of the clay and aliphatic C-H stretch of the octadecylamine are observed in the two spectra. The spectrum for pristine Mfensi clay shows only one peak which is a tall broad peak between 1100 cm^{-1} and 970 cm^{-1} and is reported to be a peak for the Si-O vibrational motions (Nascimento *et al*, 2002; Zhang *et al*, 2011). On the other hand, the Modified Mfensi clay spectrum shows three different major peaks. Two short narrow adjacent peaks at 2919 cm^{-1} and 2850 cm^{-1} which are reported to be aliphatic symmetric and asymmetric stretch of C-H vibrations (Coats, 2000; Wahit *et al*, 2011). The third peak, a semi-tall, broad peak observed

between 1100cm^{-1} and 970cm^{-1} , which is reported to be a peak for the Si-O vibrational motions (Nascimento *et al*, 2002; Zhang *et al*, 2011).

Comparing the IR spectrum of the modified Mfensi clay to the pristine Mfensi clay, it can be deduced that, the absorbance of Si-O vibrations reduced, from 1.2638 in pristine Mfensi clay to 0.4837 in modified Mfensi clay. The modified Mfensi clay recorded an absorbance of 0.1650 and 0.0774 for C-H symmetric and asymmetric stretch respectively, as shown in Table 4.2 below. It is therefore suspected that, reduction in absorbance for Si-O vibrations is due to the presence C-H molecular vibrations contributed by the octadecylamine.

Table 4.2: Table of Si-O and C-H absorbance in Pristine and Modified Mfensi clays.

Peak Positions	Si-O Absorbance			C-H Absorbance		
	Pristine Mfensi	Modified Mfensi	Octadecylamine	Pristine Mfensi	Modified Mfensi	Octadecylamine
1029.13	1.2638	0.4837	0.0000	0.0000	0.0000	0.0000
2850.36	0.0000	0.0000	0.0000	0.0000	0.0774	1.5042
2919.01	0.0000	0.0000	0.0000	0.0000	0.1650	0.6177

The C-H symmetric and asymmetric peaks are also suspected to be contributed by the long carbon chained octadecylamine surfactant present in the modified clay.

From the spectrum of the modified clay, there is no new peak observed, apart from that of the constituent compounds. The absence of a peak for a possible chemical bond between the clay

molecules and that of the octadecylamine molecules indicates that, the octadecylamine molecules are adsorbed to the clay surfaces.

The presence of C-H vibrational motions therefore confirms the modification of organophobic pristine (raw) Mfensi clay into organophilic Mfensi clay as reported by Salawudeen *et al*, (2008).

Individual spectrum of the modified Mfensi clay and Pristine Mfensi clay are shown in Appendix 2.

KNUST



4.2.2 FT-IR Spectra of Modified Aferi clay compared to that of Pristine Aferi clay

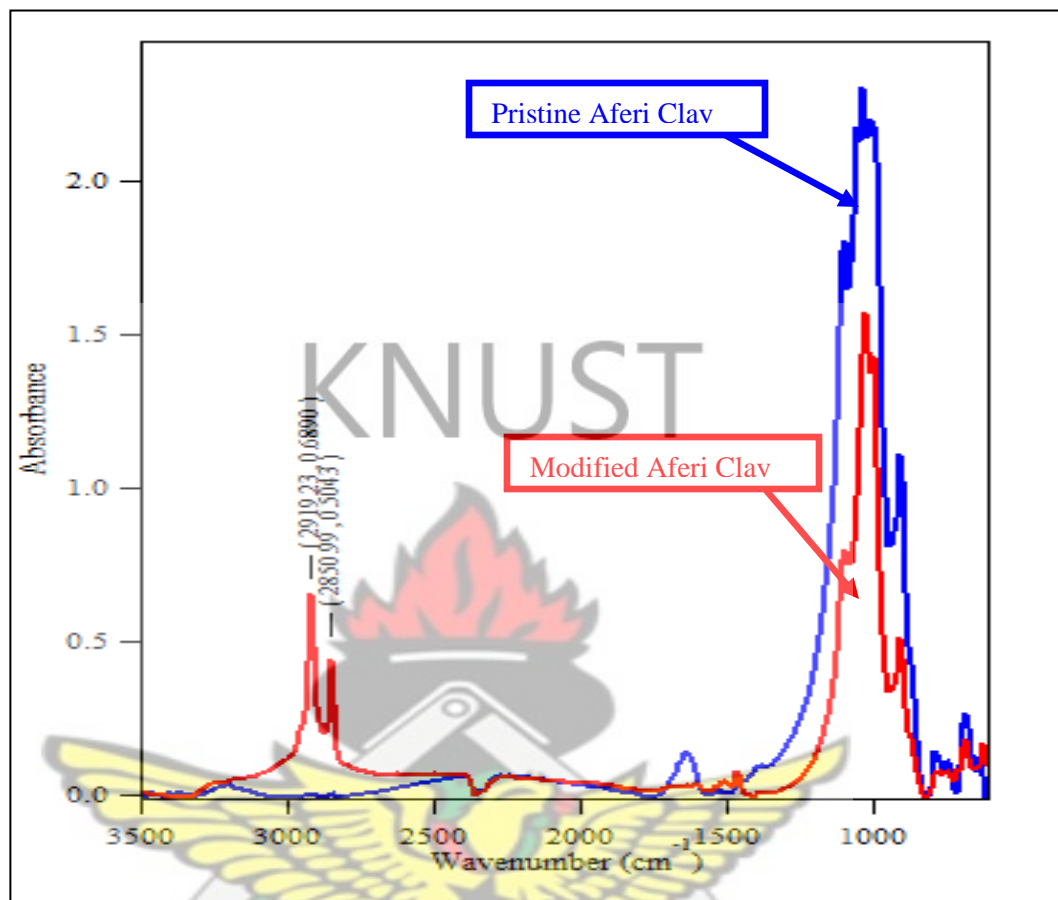


Figure 4.2: FT-IR Spectra of Pristine Aferi clay compared to that of the Modified Aferi clay.

Stacked spectra of pristine (raw) Aferi clay and the modified Aferi clay are compared in Figure 4.2 above. Si-O vibration of the clay and aliphatic C-H stretch of the octadecylamine are observed in the two spectra. The spectrum for pristine (raw) Aferi clay shows only one peak which is a tall broad peak between 1100 cm^{-1} and 970 cm^{-1} and is reported to be a peak for the Si-O vibrational motions (Nascimento *et al*, 2002; Zhang *et al*, 2011). On the other hand, the Modified Aferi clay spectrum shows three different major peaks. Two short narrow adjacent peaks at 2919 cm^{-1} and 2850 cm^{-1} which are reported to be aliphatic symmetric and asymmetric stretch of C-H vibrations (Coats, 2000; Wahit *et al*, 2011). The third peak, a semi-tall broad peak is observed between 1100 cm^{-1} and 970 cm^{-1} and reported to be a peak for the Si-O vibrational motions (Nascimento *et al*, 2002; Zhang *et al*, 2011).

Comparing the spectrum of modified Aferi clay to the pristine Aferi clay, it can be deduced that, the absorbance of Si-O vibrations reduced, from 2.4522 in pristine Aferi clay to 1.5047 in modified Aferi clay. The modified Aferi clay recorded an absorbance of 0.1689 and 0.5043 for C-H symmetric and asymmetric vibrations respectively, as shown in Table 4.3 below. It is therefore suspected that, reduction in absorbance for Si-O vibrations is due to the presence C-H molecular vibrations contributed by the octadecylamine.

Table 4.3: Table of Si-O and C-H absorbance in Pristine and Modified Aferi clays.

Peak Positions	Si-O Absorbance			C-H Absorbance		
	Pristine Aferi	Modified Aferi	Octadecylamine	Pristine Aferi	Modified Aferi	Octadecylamine
1049.85	2.4522	1.5047	0.0000	0.0000	0.0000	0.0000
2850.36	0.0000	0.0000	0.0000	0.0000	0.5043	1.5042
2919.01	0.0000	0.0000	0.0000	0.0000	0.1689	0.6177

The C-H symmetric and asymmetric peaks are therefore suspected to be contributed by the long carbon chained octadecylamine present in the modified Aferi clay.

From the spectrum of the modified Aferi clay, there is no new peak observed, apart from that of the constituent compounds. The absence of a peak for a possible chemical bond between the clay molecules and that of the octadecylamine molecules indicates that, the octadecylamine molecules are adsorbed to the clay surfaces. The presence of C-H vibrational motions confirms the modification of organophobic pristine (raw) Aferi clay into organophilic Aferi clay as reported by Salawudeen, *et al* (2008)

Individual spectrum of the modified Mfensi clay and Pristine Mfensi clay are shown on Appendix 2.

4.2.3 FT-IR spectra of low density polyethylene/ Mfensi clay nanocomposites at different clay loadings.

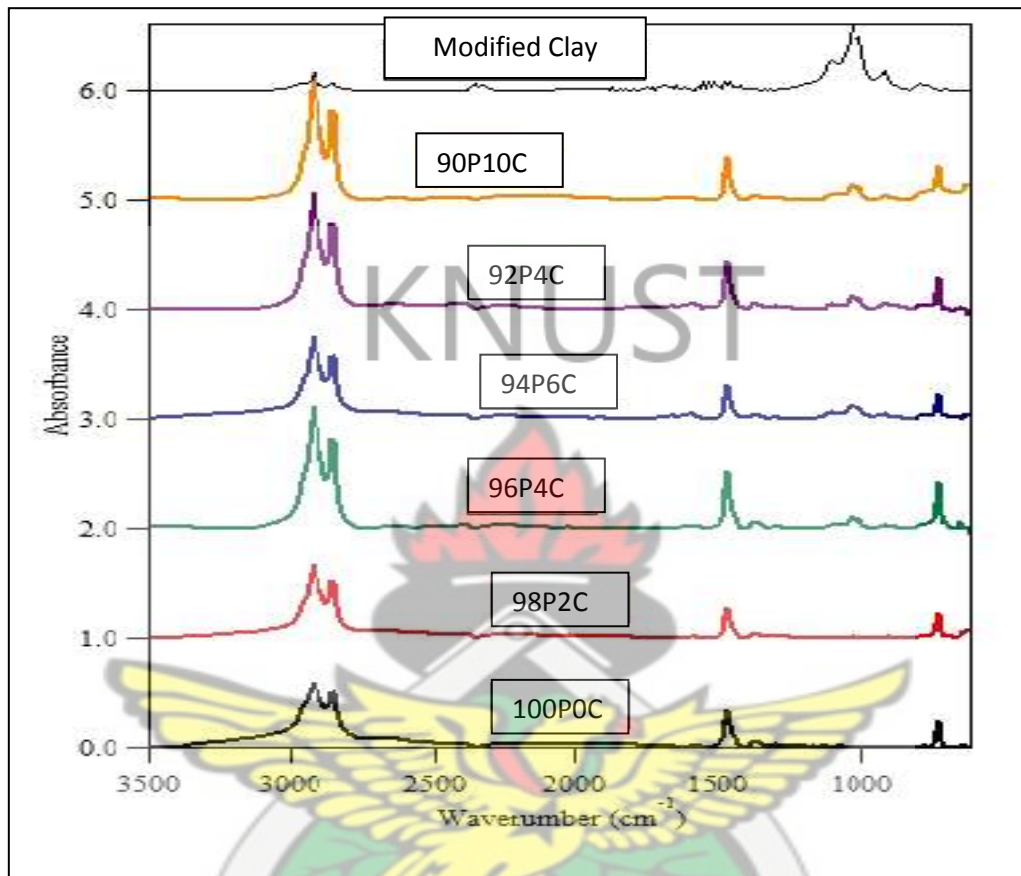


Figure 4.3: FT-IR Spectra Comparing LDPE/Mfensi clay nanocomposites of different percentage clay loadings to virgin LDPE. (P-Polymer, C-clay.)

From bottom to up, Figure 4.3 shows the spectrum of virgin low density polyethylene (LDPE), LDPE/ Mfensi clay nanocomposites of 98, 96, 94, 92, 90 wt% LDPE and 2, 4, 6, 8, 10 wt% Mfensi clay respectively, and organically modified Mfensi clay. The characteristic bands of C-H vibrational motions at 2919 cm^{-1} , 2850 cm^{-1} , 1460 cm^{-1} , and 725 cm^{-1} for symmetric stretch, asymmetric stretch, bending and rocking (Coats, 2000; Zhao *et al*, 2005; Wahit *et al*, 2011) can be respectively observed in the virgin LDPE (100P0C), and all the nanocomposites formed.

The modified Mfensi clay has only the symmetric and asymmetric stretch of C-H vibrations present. It can therefore be inferred that, the rocking and bending motions of C-H vibrations are hindered in the modified Mfensi clay.

Comparing C-H symmetric stretch peaks in virgin 100P0C spectrum to that of 96P4C and 90P10C LDPE/Mfensi clay nanocomposites, it can be observed that, there is a gradual increase in the absorbance of this peak with increasing clay content. As shown in Table 4.4, the absorbance at 0 wt% clay content is 0.5831 whereas that for 4 wt% and 10 wt% clay content increases to 1.0059 and 1.7575 respectively. This increment is suspected to be due to the presence of octadecylamine in the modified clay.

Table 4.4: Changes in C-H symmetric stretch absorbance with increasing clay content

Clay content (wt%)	C-H symmetric stretch absorbance	Si-O peak absorbance
	LDPE/ Mfensi clay nanocomposite	LDPE/ Mfensi clay nanocomposite
0	0.5831	0.0000
4	1.0059	0.2298
10	1.7575	0.4348

The modified Mfensi clay inevitably has the highest Si-O peak absorbance intensity. While the least Si-O peak absorbance intensity is observed in 96P4C LDPE/Mfensi clay nanocomposite.

The presence of Si-O vibrations between 1100 cm^{-1} and 970 cm^{-1} (Nascimento *et al*, 2002; Zhang *et al*, 2011) in all the spectra except for the virgin LDPE-100P0C confirms the presence of clay in the LDPE/ Mfensi clay nanocomposites formed. It is also observed that, the absorbance of the Si-O peak increases with increasing clay content.

Individual spectrum of the LDPE/Mfensi clay nanocomposites are shown on Appendix 3.

4.2.4.: Influence of modified Mfensi Clay on the Si-O and C-H functional groups of Low Density Polyethylene (LDPE)/ Mfensi clay nanocomposite

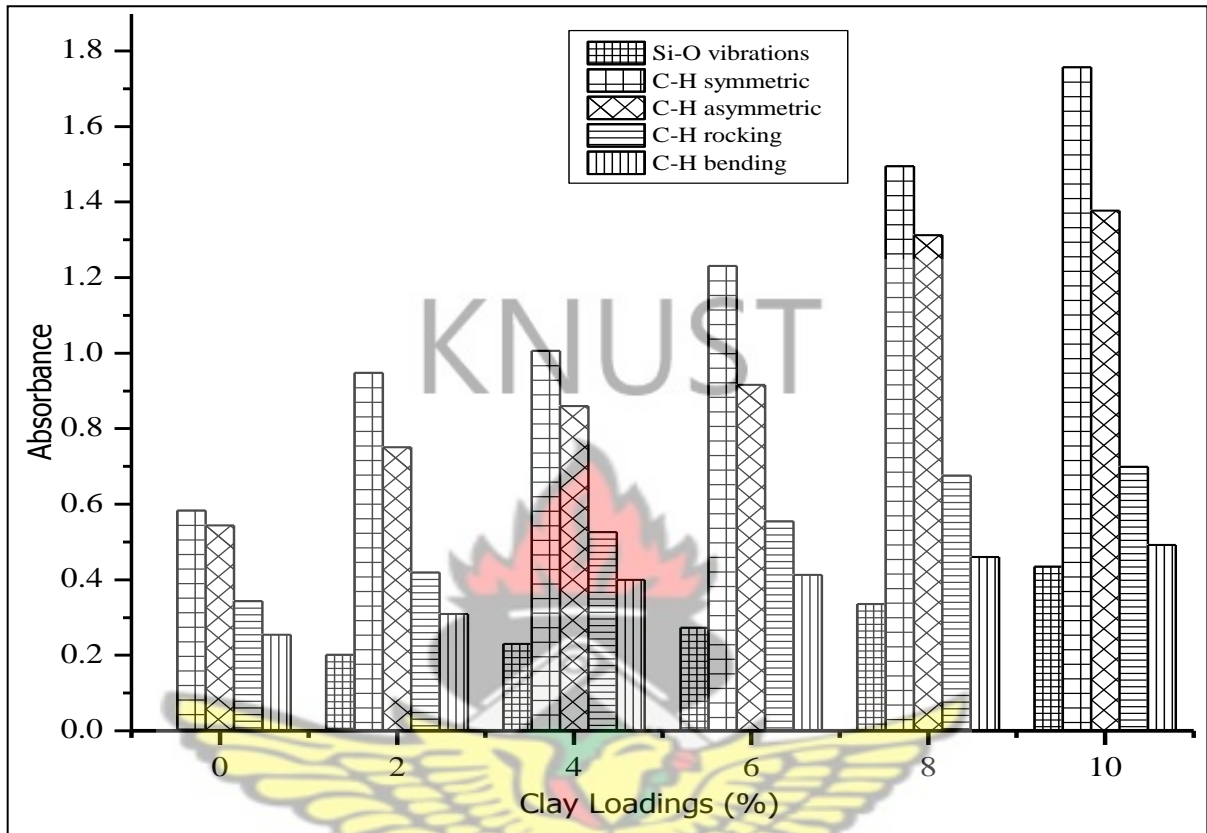


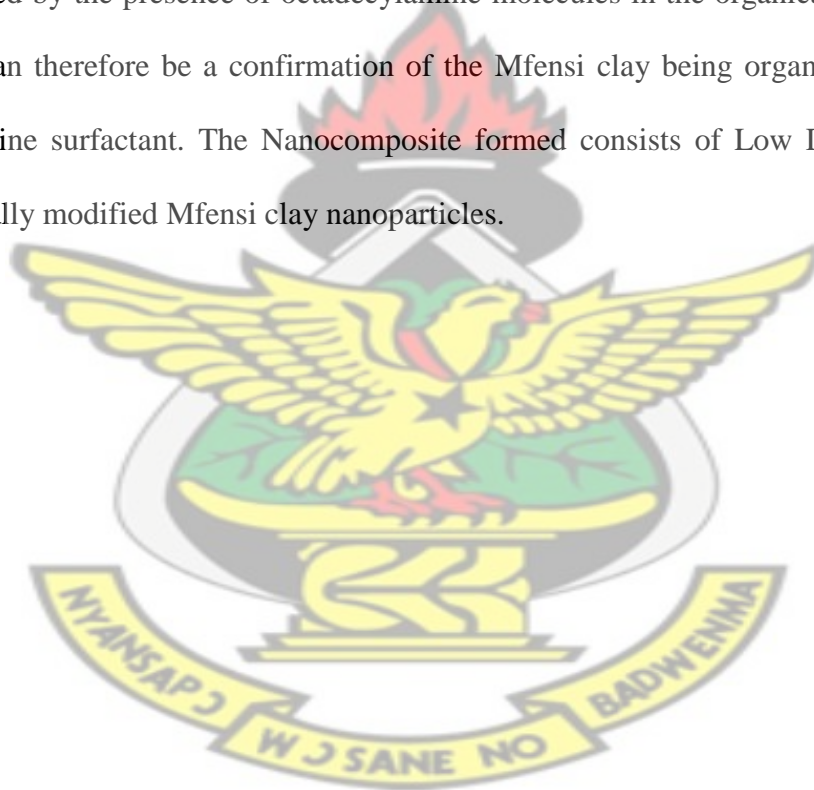
Figure 4.4: Functional group absorbance versus percentage clay loadings of LDPE/ Mfensi clay nanocomposites

Absorbance of Si-O vibrations, C-H symmetric stretch, C-H asymmetric stretch, C-H rocking and C-H bending absorbance intensities observed in the LDPE/ Mfensi clay nanocomposite spectra at different clay loadings are compared in Figure 4.4 above.

At 0 wt% clay loadings, C-H symmetric stretch is observed to have the highest absorbance intensity at 0.5831 followed by, C-H asymmetric stretch, C-H rocking and C-H bending respectively with absorbance intensities of 0.5831, 0.5437, 0.3430, and 0.2542 respectively. This order in absorbance intensities at 0 wt% modified Mfensi clay loadings is also observed the LDPE/ Mfensi clay nanocomposites at 2 wt%, 4 wt%, 6 wt%, 8 wt%, and 10 wt% modified Mfensi clay loadings. Even though the trend is same at different loadings of modified Mfensi

clay, the absorbance intensities are different. Absorbance intensity increases with increasing modified Mfensi clay contents of the LDPE/ Mfensi clay nanocomposites. The highest absorbance intensities of Si-O vibrations, C-H symmetric stretch, C-H asymmetric stretch, C-H rocking and C-H bending are observed at 10 wt% clay loadings. On the other hand, the least absorbance intensities are observed at 2 wt% clay loadings.

This increase in absorbance intensity of C-H molecular vibrations of the LDPE/ Mfensi clay nanocomposites, with corresponding increase in modified Mfensi clay loadings is suspected to be contributed by the presence of octadecylamine molecules in the organically modified Mfensi clay. This can therefore be a confirmation of the Mfensi clay being organically modified with octadecylamine surfactant. The Nanocomposite formed consists of Low Density Polyethylene and organically modified Mfensi clay nanoparticles.



4.2.5 FT-IR Spectra of Low Density Polyethylene/ Aferi clay nanocomposite at different clay loadings

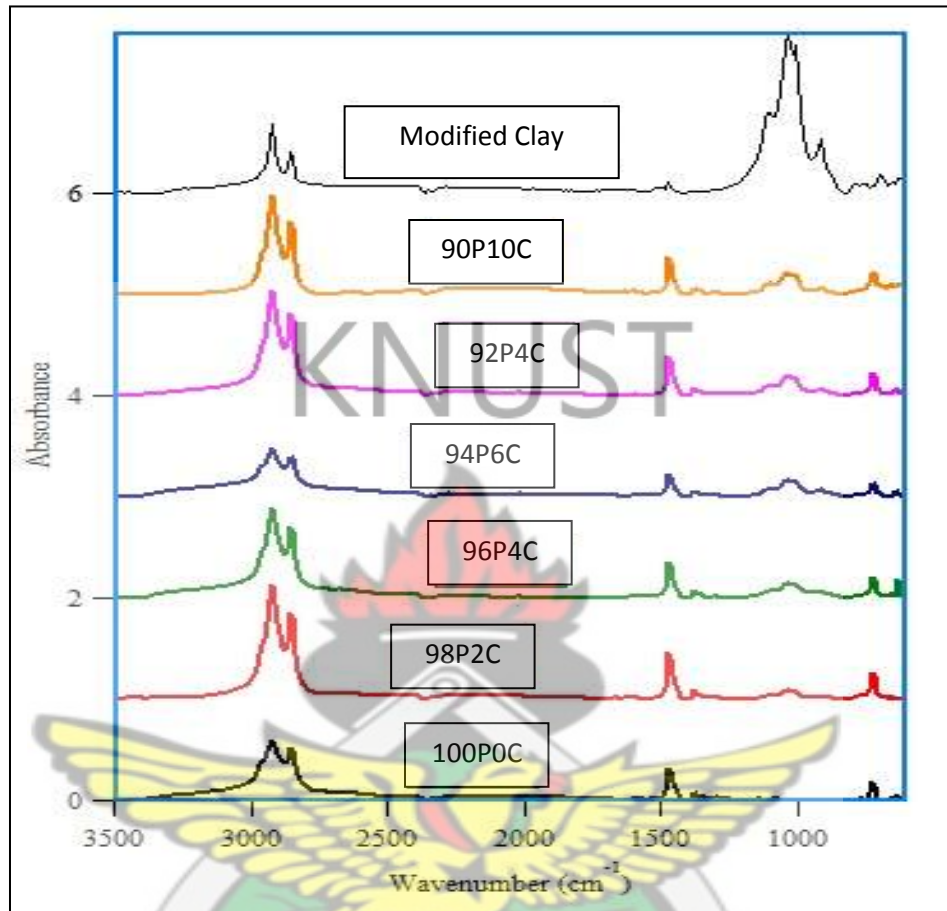


Figure 4.5: FT-IR Spectra comparing LDPE/ Aferi clay nanocomposites of different percentage clay loadings to virgin LDPE (P-Polymer, C-clay.)

Figure 4.5 shows FT-IR spectra of virgin Low Density Polyethylene (LDPE), LDPE/ Aferi clay nanocomposites of 98, 96, 94, 92, 90 wt% LDPE and 2, 4, 6, 8, 10 wt% Aferi clay respectively, and organically modified Aferi clay from bottom to up. The characteristic bands of C-H vibrational motions at 2919 cm⁻¹, 2850 cm⁻¹, 1460 cm⁻¹, and 725 cm⁻¹ for symmetric stretch, asymmetric stretch, bending and rocking (Coats, 2000; Zhao *et al*, 2005; Wahit *et al*, 2011) can be observed respectively in the virgin LDPE (100P0C), 96P4C, and 90P10C spectra. The modified Aferi clay has only symmetric and asymmetric stretch of C-H present. It can therefore be inferred that, the rocking and bending motions of the C-H are hindered in the modified Aferi clay.

Comparing C-H symmetric stretch peaks in 100P0C spectrum, to that of 96P4C and 90P10C LDPE/ Aferi clay nanocomposites, it can be observed in Table 4.5 that, the absorbance intensity increased in 4 wt% clay loadings, at a value of 1.1625 whereas 0 wt% Aferi clay loadings had a value of 0.5831. But it did decrease in 10 wt% Aferi clay loadings to a value of 0.6126 which is marginally larger than 0.5831 absorbance intensity of 0 wt% Aferi clay loadings. It can therefore be inferred that, the octadecylamine contribution to C-H absorbance intensities in LDPE/clay nanocomposites are relative to the type of clay particles involved. The absorbance intensity for LDPE/ Aferi clay nanocomposites drops at 10 wt% modified Aferi clay loadings, while that of LDPE/ Mfensi clay nanocomposites increase with increasing modified Mfensi clay content.

Table 4.5: Changes in C-H symmetric stretch absorbance with increasing clay content

Clay content (wt%)	C-H symmetric stretch absorbance	Si-O peak absorbance
	LDPE/ Mfensi clay nanocomposite	LDPE/ Mfensi clay nanocomposite
0	0.5831	0.0000
4	1.1625	0.3732
10	0.6126	0.4997

Further more, the presence of Si-O vibrations between 1100 cm^{-1} and 970 cm^{-1} (Nascimento *et al*, 2002; Zhang *et al*, 2011) in all the spectra except for the 100P0C confirms the presence of modified Aferi clay in the LDPE/ Aferi clay nanocomposites formed. It is also observed that, the absorbance intensity of the Si-O peak increases with increasing modified Aferi clay content. Modified Aferi clay inevitably has the highest Si-O peak absorbance intensity. While the least Si-O peak absorbance intensity is observed in 96P4C LDPE/Aferi clay nanocomposite.

Individual spectrum of the LDPE/Aferi clay nanocomposites are shown on Appendix 3.

4.1.6 Influence of Aferi Clay on the characteristic functional group vibrations of Low density Polyethylene (LDPE)

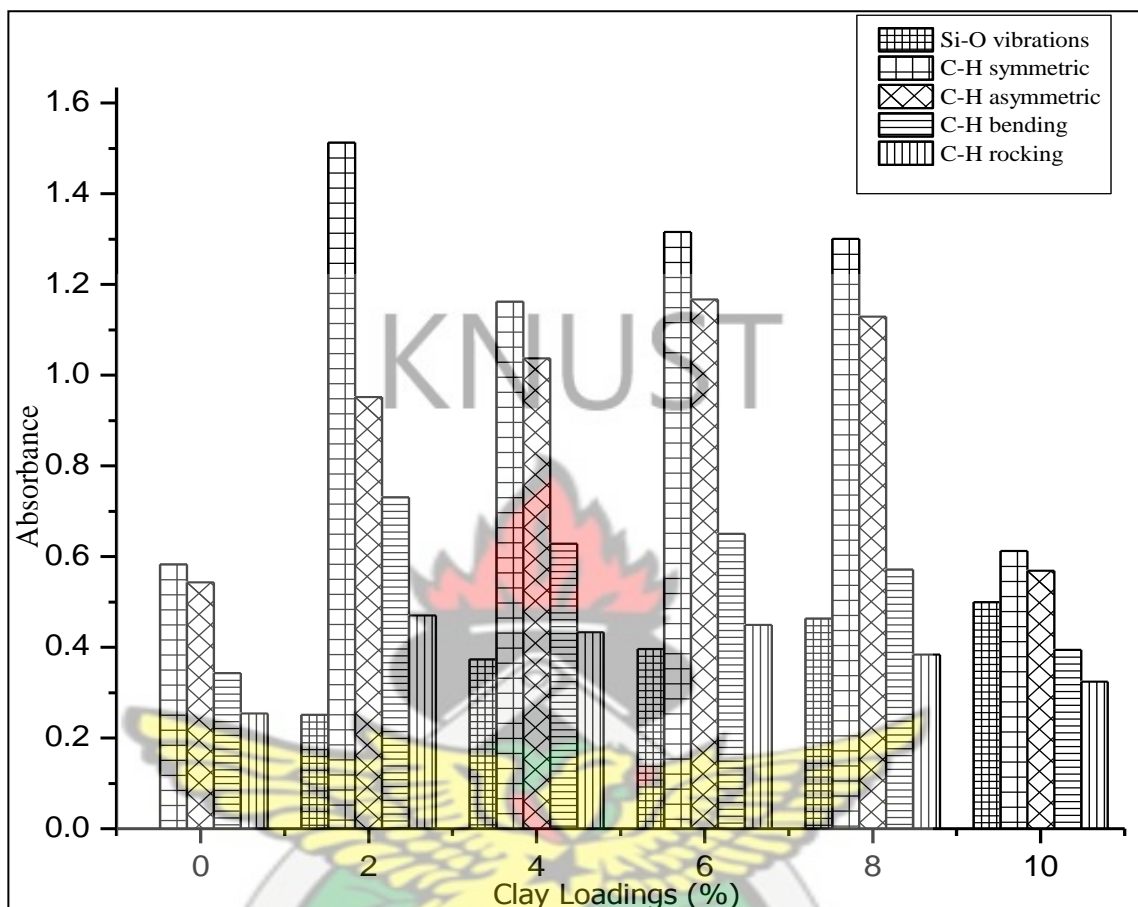


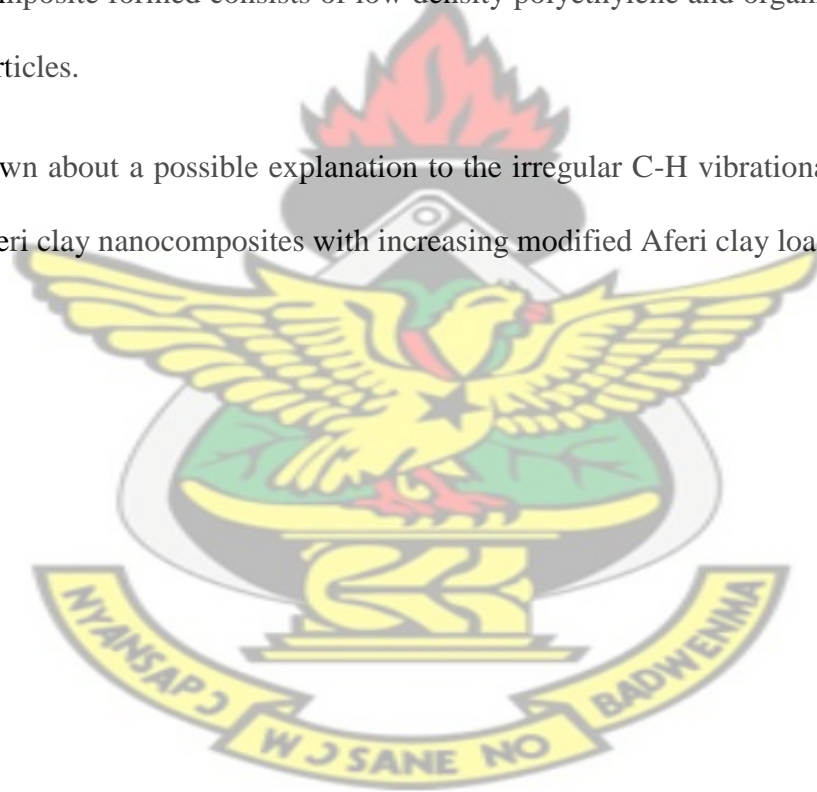
Figure 4.6: Functional group absorbance versus percentage clay loadings of LDPE/ Mfensi clay nanocomposites.

In Figure 4.6, the changes in C-H vibrational motions in virgin LDPE are compared to that of LDPE/Aferi clay nanocomposites at different modified Aferi clay loadings. From Figure 4.6, there is a general increase in the C-H symmetric stretch, asymmetric stretch, rocking and bending absorbance intensities of LDPE/Aferi clay nanocomposites, from 2 wt% to 10 wt% modified Aferi clay loadings compared to that of 0wt% modified Aferi clay loadings. This increment does not follow any trend relative to the percentage clay loadings. The highest C-H symmetric stretch absorbance intensity is observed at 2 wt% Aferi clay loadings. That for C-H asymmetric stretch absorbance intensity is observed at 6 wt% modified Aferi clay loadings. The highest absorbance intensity peak bending and rocking motions are both observed at 2 wt% modified Aferi clay

loadings. Only absorbance intensities of Si-O vibrations increased with increasing clay content with the highest peak being recorded at 10 wt% modified Aferi clay loadings and the least being at 2 wt% modified Aferi clay loadings.

This increase in absorbance intensity of C-H molecular vibrations of LDPE/ Aferi clay nanocomposites relative to the modified Aferi clay loadings is suspected to be contributed by the presence of octadecylamine molecules in the organically modified Aferi clay. This can therefore be a confirmation of the Aferi clay being organically modified with octadecylamine surfactant. The Nanocomposite formed consists of low density polyethylene and organically modified Aferi clay nanoparticles.

Little is known about a possible explanation to the irregular C-H vibrational motions increment in LDPE/Aferi clay nanocomposites with increasing modified Aferi clay loadings.



4.3 X-ray Diffractometric Characterization

4.3.1. XRD Characterization of organically modified Mfensi clay

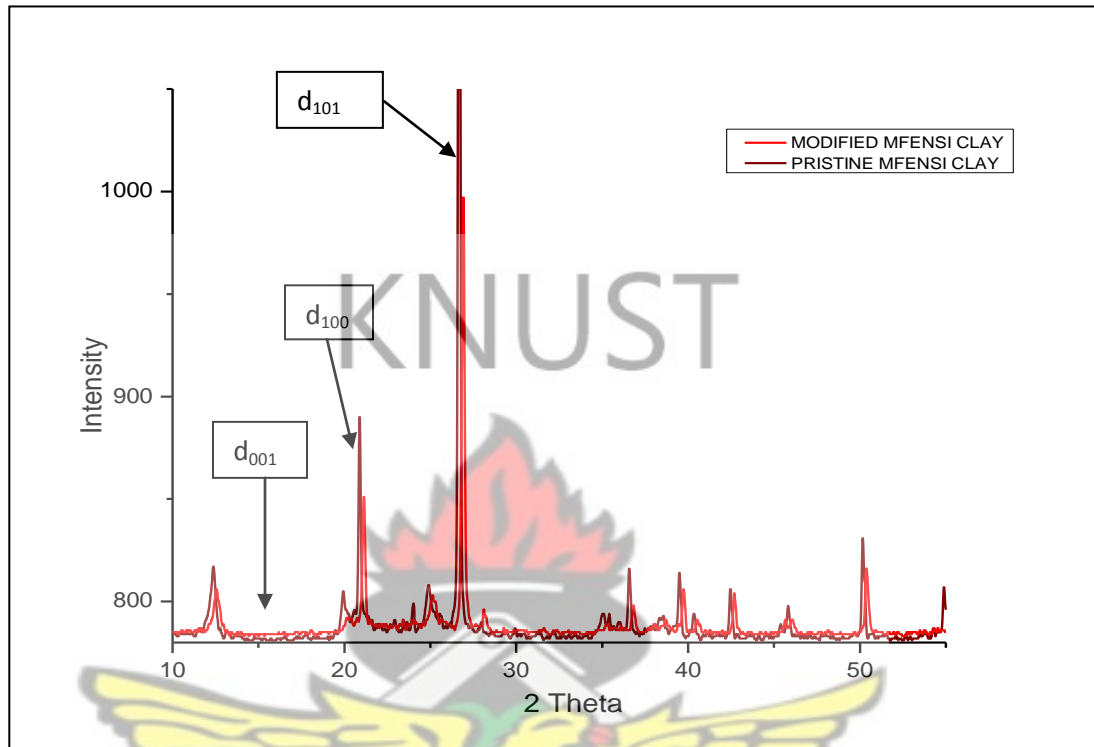
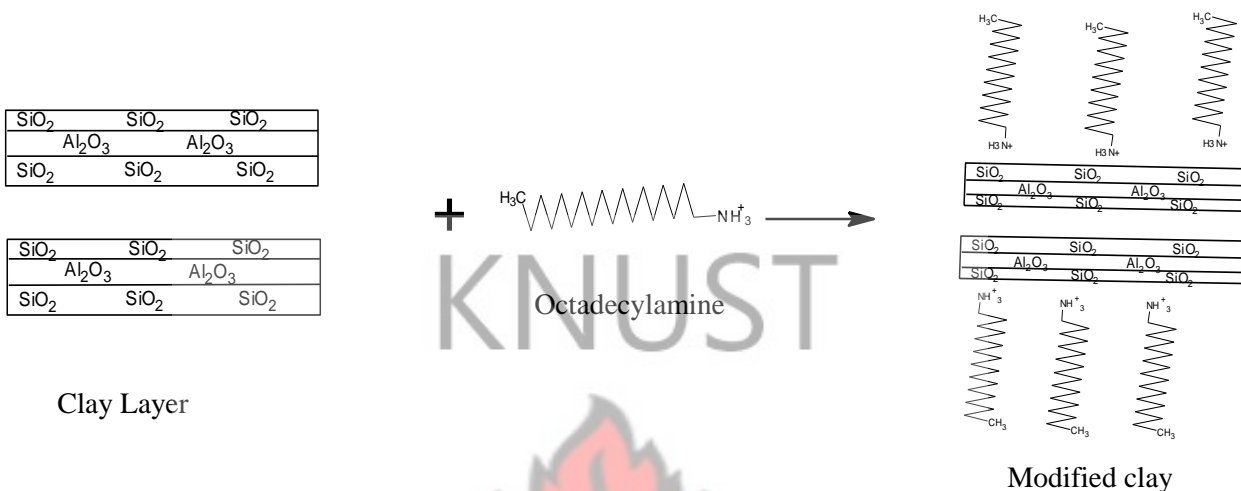


Figure 4.7: X-ray diffractogram comparing modified Mfensi clay to pristine Mfensi clay.

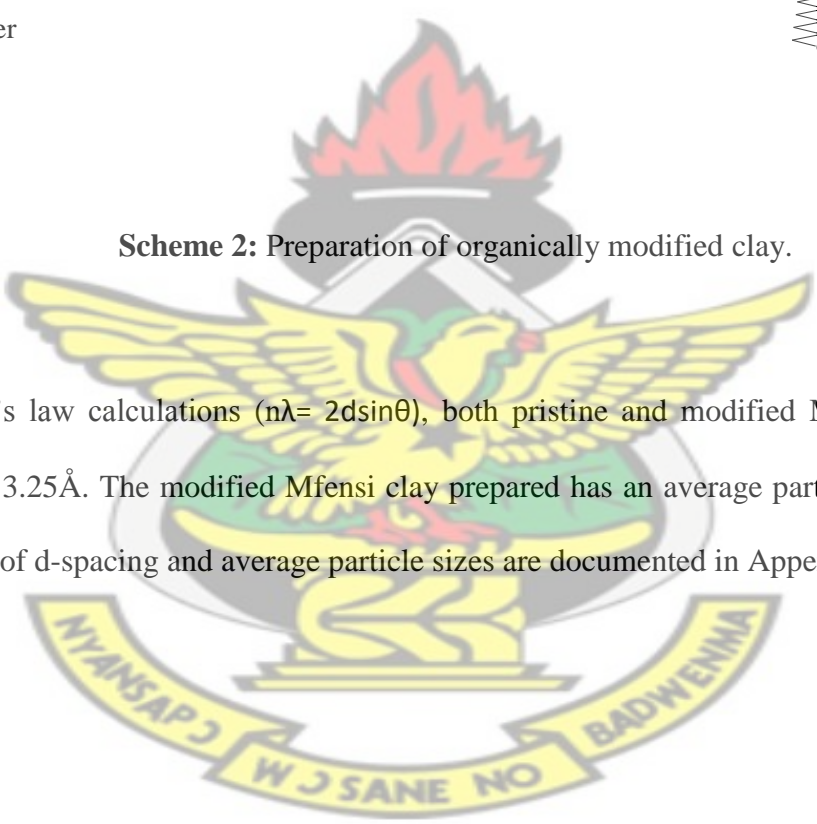
X-ray diffraction of the modified Mfensi clay compared to the pristine Mfensi clay showed no change in the d-spacing (d_{001} at $2\theta = 16.375^\circ$) of the modified clay in Figure 4.7. An increase in the d-spacing of the modified clay cause a shift in the position of the d_{001} phase to lower angles which indicates the formation of an intercalated structure (Ishida *et al*, 2000). The d_{001} phase of pristine Mfensi clay observed at 16.375° on the 2θ axis did not shift in modified Mfensi clay. It can therefore be inferred that, the surfactant was adsorbed to the surface of the clay particles only, but could not intercalate the clay galleries. Results obtained from FT-IR spectra in Figure 4.1 shows no peak for a possible ionic bond formed between the RNH_3^+ of the surfactant and localized negative charges of the clay particles. It can therefore be inferred that, the adsorption of surfactant molecules to the clay surfaces occurred by a physical process. This

means weak intermolecular forces hold the surfactant molecules to the clay surfaces, as shown in scheme 2.



Scheme 2: Preparation of organically modified clay.

From Bragg's law calculations ($n\lambda = 2d\sin\theta$), both pristine and modified Mfensi clays have a d-spacing of 3.25Å. The modified Mfensi clay prepared has an average particle size of 5.54nm. Calculations of d-spacing and average particle sizes are documented in Appendix 4.



4.3.2. XRD Characterization of organically modified Aferi clay

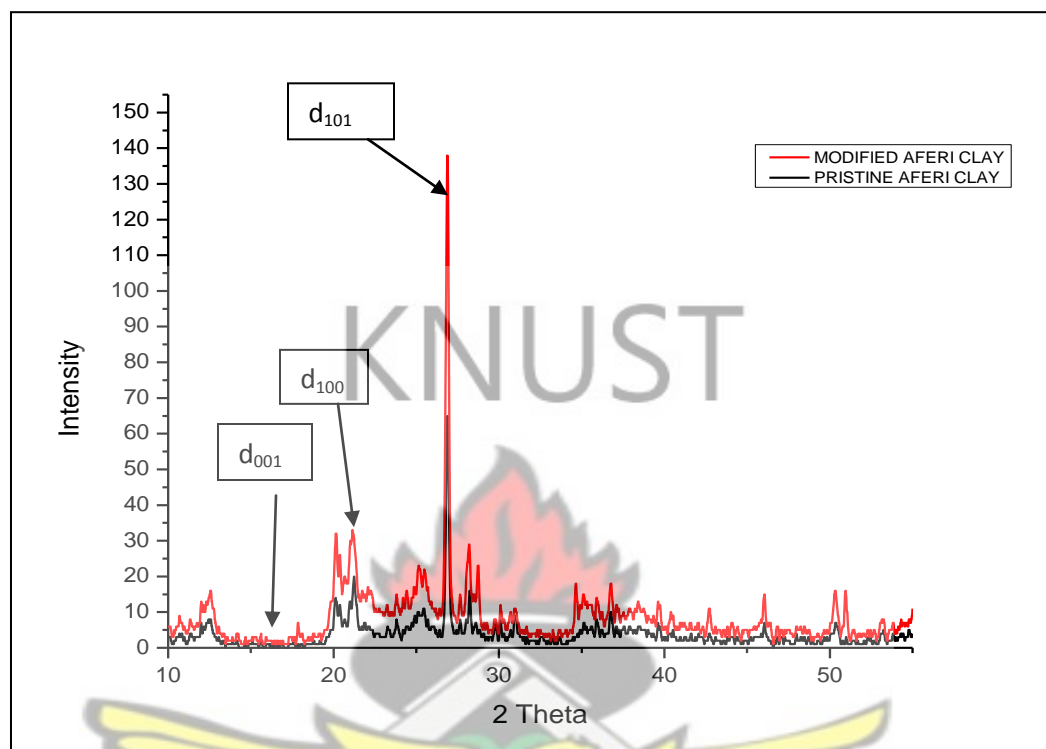


Figure 4.8: X-ray diffractogram comparing modified Aferi clay to pristine Aferi clay.

X-ray diffraction of the modified Aferi clay compared to the pristine Aferi clay in Figure 4.8 showed no change in the d-spacing (d_{001} at $2\theta = 16.375^\circ$) of the modified clay. An increase in the d-spacing of the modified clay cause a shift in the position of the d_{001} to lower angles which indicates the formation of an intercalated structure (Ishida *et al*, 2000). The d_{001} phase of pristine Aferi clay observed at 16.375° on the 2θ axis did not shift in modified Aferi clay. It can therefore be inferred that, the surfactant was adsorbed to the surface of the clay particles only, but could not intercalate the clay galleries. Results obtained from FT-IR spectra in Figure 4.2, reveals the absence of a peak for any ionic bond formed between the RNH_3^+ of the surfactant and localized negative charges of the clay particles. It can therefore be inferred that, the adsorption of surfactant molecules to the clay surfaces occurred by a physical process. Scheme 2 also describes organically modified Aferi clay. Pristine and modified Aferi clay samples have a common

d-spacing of 3.22Å, calculated from the Bragg's law ($n\lambda = 2d\sin\theta$). The organically modified Aferi clay has an average particle size of 5.55nm. Calculations of d-spacing and average particle sizes are documented in Appendix 4.

4.3.3 XRD Characterization of Low Density Polyethylene/ Mfensi clay nanocomposite

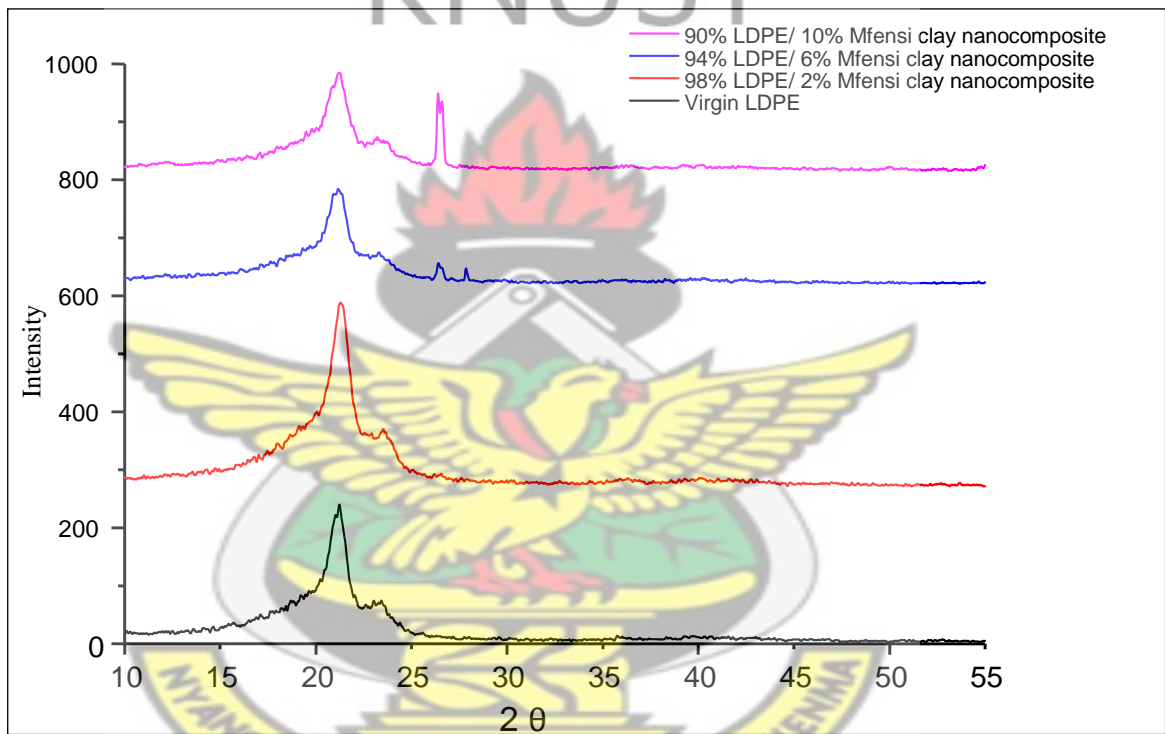


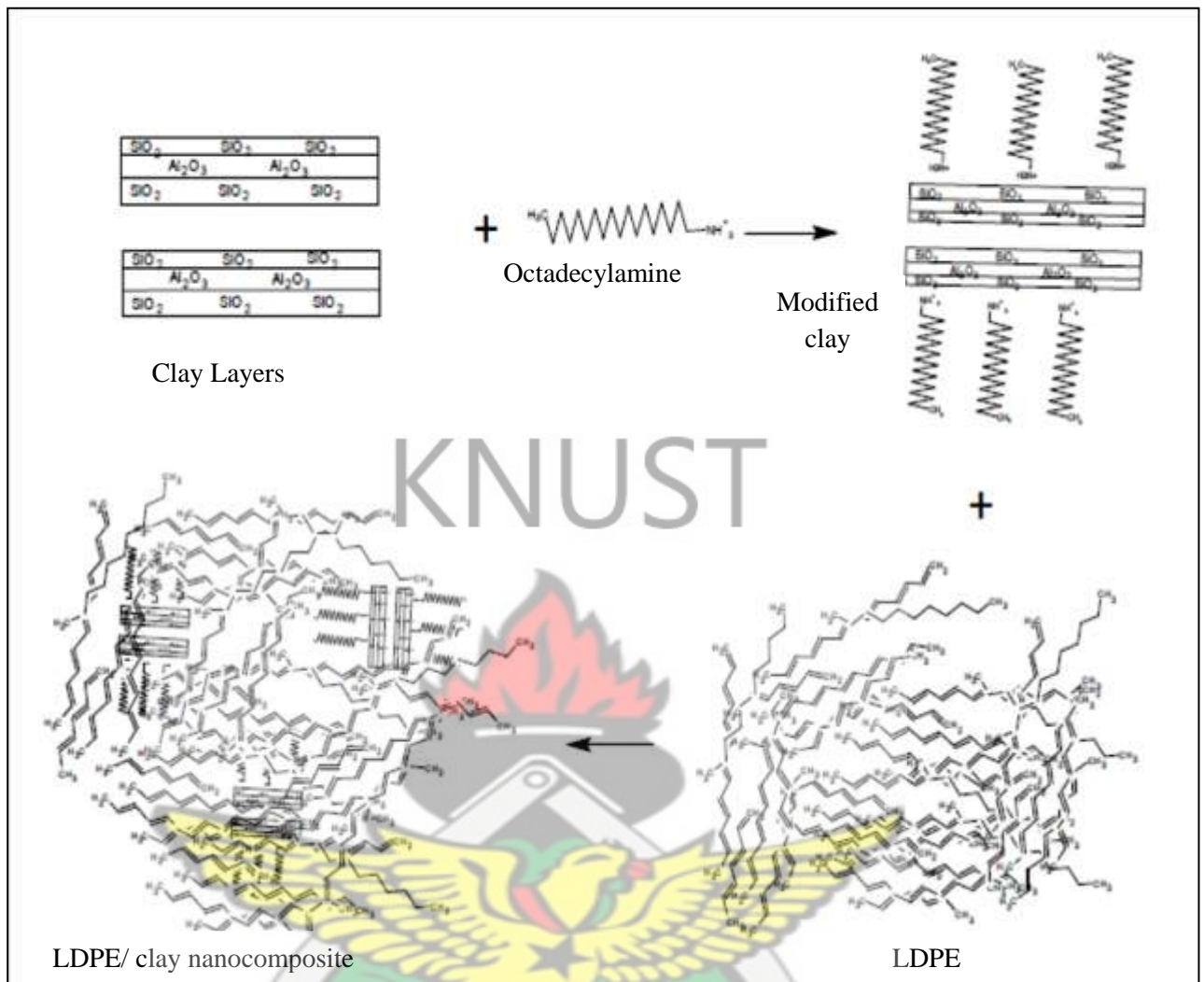
Figure 4.9: X-ray diffractogram comparing LDPE/ Mfensi clay nanocomposites at 2 wt%, 6 wt% and 10 wt% clay loadings to virgin LDPE

X-ray diffractograms of LDPE/Mfensi clay nanocomposites with 2 wt%, 6 wt% and 10 wt% modified Mfensi clay loadings are compared to that of virgin LDPE in Figure 4.9. The presence of a peak in an X-ray diffractogram indicates a measure of orderliness of particles at a corresponding angle on the 2θ axis (Weidong and Vaia, 2002).

It is therefore observed that, a broad peak at $2\theta = 21.16^\circ$ for both the amorphous and crystalline phases of the Low Density Polyethylene (LDPE) is dominant in the virgin LDPE diffractogram. This phase can also be observed in the three nanocomposites diffractograms stacked over that of the virgin LDPE.

Comparing the X-ray diffractogram for the 2 wt% modified Mfensi clay loadings to that of the virgin LDPE, shows a similar diffractogram, which has no new peak. This indicates that, even though there are clay particles in the material, as proven by the FT-IR spectrum of the same sample, Figure 4.3, the clay particles are completely dispersed in the LDPE matrix, as such could not diffract incident X-rays. On the other hand, it can be observed in diffractograms for LDPE/Mfensi clay nanocomposites with 6 wt% and 10 wt% modified Mfensi clay loadings that, a narrow peak is obtained at an angle of 26.52° on the 2θ axis. This peak is the dominant peak in the organically modified Mfensi clay diffractogram in Figure 4.7. This means that, the clay particles in these nanocomposites are clustered and so, they maintain their orderliness which enables them to diffract incident X-rays. This leads to the inference that complete dispersion of clay particles in the LDPE/Mfensi clay nanocomposites is best obtained at 2 wt% modified Mfensi clay loadings. This confirms similar observations made on Polymer/clay nanocomposite systems, by Okada *et al*, (2006).

Unlike montmorillonite clay, reported by literature (Zhao *et al*, 2005), the absence of intercalation of Aferi clay galleries by both the surfactant and LDPE molecules, make the structure of the LDPE/Mfensi clay nanocomposite formed be described as a phase separated structure. This structure is represented in scheme 3.



Scheme 3: Formation of Phase separated Structured LDPE/ clay nanocomposite.

4.3.4 XRD Characterization of Low Density Polyethylene/ Aferi clay nanocomposite

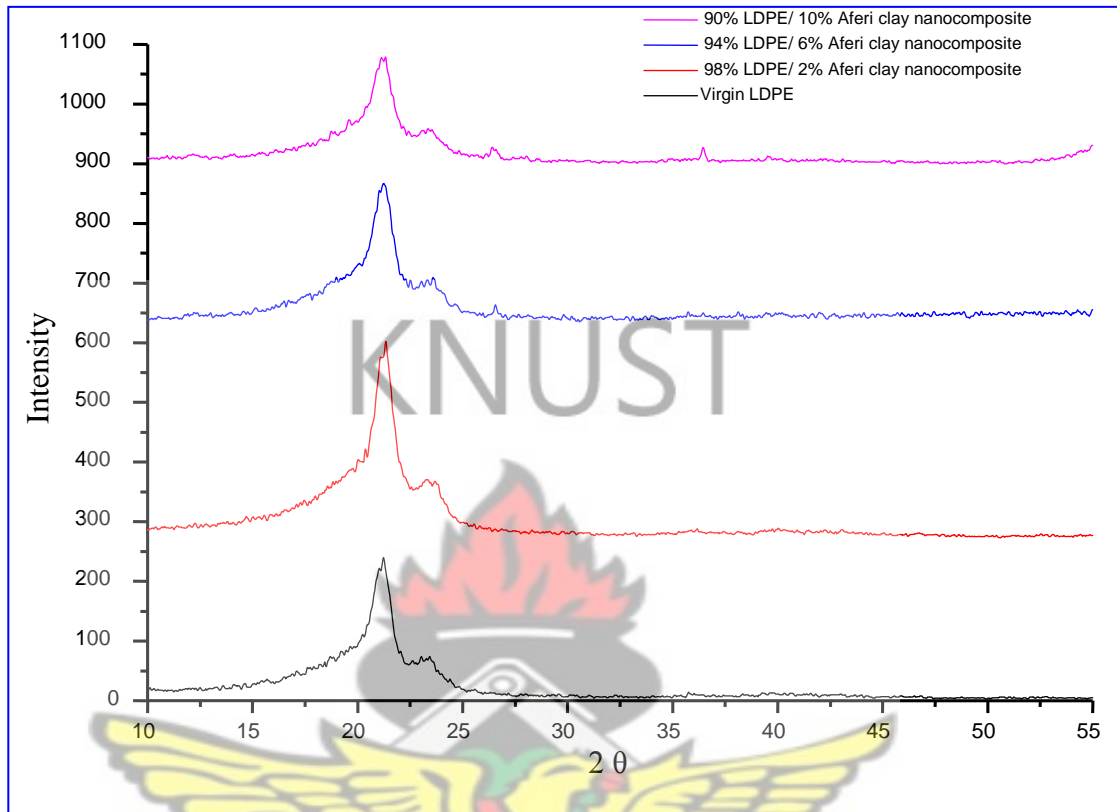


Figure 4.10: X-ray diffractogram comparing LDPE/ Aferi clay nanocomposites to virgin LDPE.

X-ray diffractograms of LDPE/ Aferi clay nanocomposites with 2 wt%, 6 wt% and 10 wt% modified Aferi clay loadings are compared to that of virgin LDPE in Figure 4.10. The presence of a peak in an X-ray diffractogram indicates a measure of orderliness of particles at a corresponding angle on the 2θ axis (Weidong and Vaia, 2002).

It is therefore observed that, a broad peak at 21.16° for both the amorphous and crystalline phases of the LDPE is dominant in the virgin LDPE. This phase can also be observed in the three LDPE/ Aferi clay nanocomposite diffractograms stacked over that of the virgin LDPE.

Comparing the X-ray diffractogram for the 2 wt% modified Aferi clay loadings to that of the virgin LDPE, shows a similar diffractogram. This indicates that, eventhough there are clay

particles in the material as proven by the FT-IR spectrum of the same sample, Figure 4.5, the clay particles are completely dispersed in the LDPE matrix. The dispersed clay particles could not diffract incident X-rays.

On the other hand, it can be observed in diffractograms for LDPE/ Aferi clay nanocomposites with 6 wt% and 10 wt% modified Aferi clay loadings that, a small peak is obtained at an angle of 26.52° on the 2θ axis. This is the dominant peak of the organically modified Aferi clay diffractogram in Figure 4.8. Which means, the clay particles in these nanocomposites are clustered. These clusters maintain their orderliness which enables them to diffract incident X-rays.

It is therefore inferred that, complete dispersion of clay particles in the LDPE/ Aferi clay nanocomposites is best obtained at 2 wt% modified Aferi clay loadings. A confirmation of similar observations made on Polymer/clay nanocomposite systems, by Okada *et al*, (2006).

Comparing LDPE/ Aferi clay nanocomposites to that of LDPE/ Mfensi clay nanocomposites, it is observed that, modified Aferi clay has the best particle dispersion in LDPE matrix than modified Mfensi clay.

Unlike modified montmorillonite, reported by literature (Zhao *et al*, 2005), X-ray diffractometry of LDPE/ Aferi clay nanocomposites confirm that, the clay particles were not intercalated by either the surfactant or the LDPE molecules. As such, the structure of LDPE/ Aferi clay nanocomposites can be described as a phase separated structure. This structure is illustrated in Scheme 3.

4.4 Influence of clay on crosslinking density of Low density polyethylene

4.4.1 Crosslinking density of the LDPE/ Mfensi clay nanocomposites.

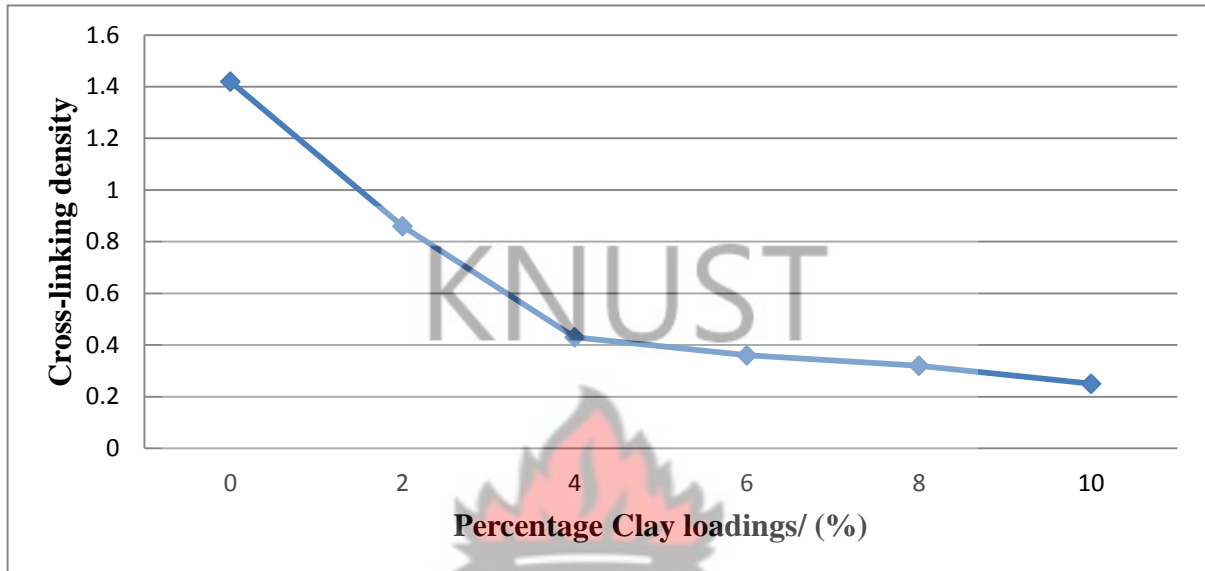


Figure 4.11: A Graph of Swelling Index of LDPE/ Mfensi Clay Nanocomposites against Percentage Clay Loadings.

Crosslinking density is the inverse value of measured swelling index of a material. The larger the swelling index, the less crosslinks there are in the material (Nicholson, 1994). From the graph in Figure 4.11, it is observed that, crosslinking density of the LDPE/ Mfensi clay nanocomposites decreased with increasing clay content, from 2 wt% to 10 wt% modified Mfensi clay loadings. This indicates that, modified clay loadings cannot improve the crosslinking density of LDPE, a similar observation made by Rezanejad *et al*, (2007).

It is therefore suspected that, the clay particles serve as barriers between adjacent LDPE chains. This hinders a possible covalent bond formation between the LDPE chains. FT-IR spectra in Figure 4.3, also reports the absence of a bond between modified Mfensi clay surfaces and the LDPE molecules as such, these chains are set free, making their surfaces available for solvent interactions.

The reduced crosslinking density of LDPE/ Mfensi clay nanocomposite supports the inference that, LDPE/Mfensi clay nanocomposites formed, have a phase separated structure.

4.4.2 Crosslinking density of the LDPE/ Aferi clay nanocomposites

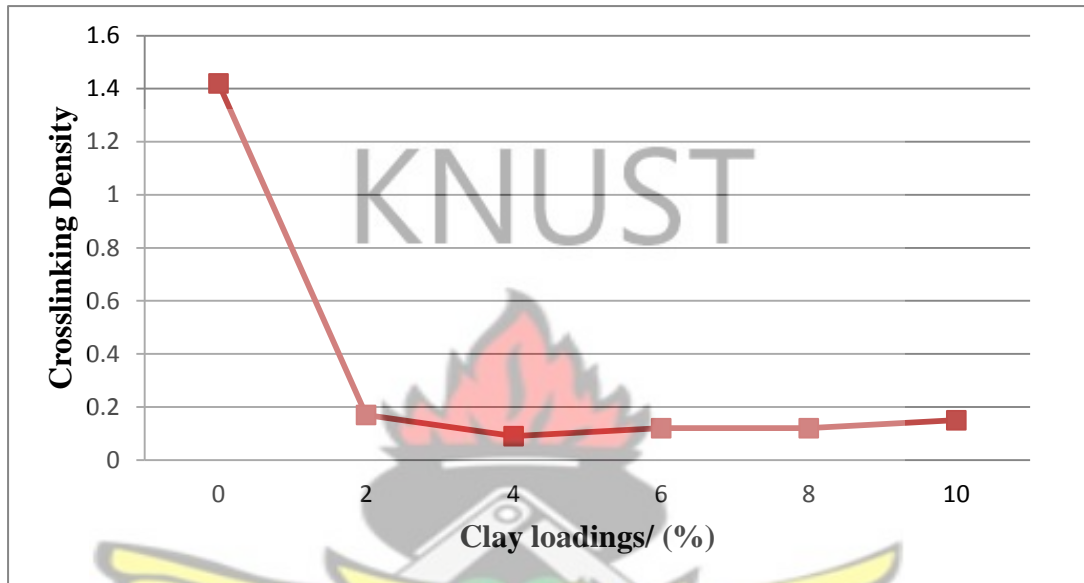


Figure 4.12: A graph of crosslinking density of LDPE/ Aferi clay nanocomposites against Percentage Clay Loadings

Crosslinking density is the inverse value of measured swelling index of a material. The larger the swelling index, the less crosslinks there are in the material (Nicholson, 1994). From the graph in Figure 4.12, it is observed that, crosslinking density of the LDPE/ Aferi clay nanocomposites decreased with increasing clay loadings, from 2 wt% to 4 wt% modified Aferi clay loadings and increased marginally from 4 wt% to 10 wt% modified Aferi clay loadings. This indicates that, modified clay loadings cannot improve the crosslinking density of LDPE, a similar observation made by Rezanejad *et al*, in 2007.

It is therefore suspected that, the modified Aferi clay particles serve as a barrier between adjacent LDPE chains. This hinders a possible covalent bond formation between the LDPE chains. FT-IR spectra in Figure 4.5, also reports the absence of a chemical bond between

modified Aferi clay surfaces and the LDPE molecules as such, these chains are set free, making their surfaces available for solvent interactions.

The reduced crosslinking density of LDPE/ Aferi clay nanocomposites supports the inference that, LDPE/ Aferi clay nanocomposites formed, have a phase separated structure.

KNUST



CHAPTER FIVE

5 CONCLUSIONS AND RECOMMENDATIONS

5.1 Conclusions

Clay particles were successfully modified with octadecylamine surfactant which was confirmed by the C-H symmetric and asymmetric stretch observed in FT-IR spectra for the modified Mfensi and Aferi clay particles.

Also, X-ray diffractograms of the modified Mfensi clay and Aferi clay showed that, the clay galleries were not intercalated by the surfactant molecules. This supports the inferences made from FT-IR spectra of the modified clays that, the surfactants were physically adsorbed to the clay surfaces.

The presence of Si-O vibrational motions peak observed in FT-IR spectra of LDPE/Mfensi clay nanocomposites and LDPE/Aferi clay nanocomposites confirms the successful incorporation of modified Mfensi and Aferi clays into the Low Density Polyethylene matrix.

Again, observation made on FT-IR spectra of the LDPE/Mfensi clay nanocomposites and LDPE/Aferi clay nanocomposites showed that, the octadecylamine surfactant was responsible for the increase in absorbance intensities of C-H vibrational motions of the LDPE/Mfensi clay nanocomposites and LDPE/ Aferi clay nanocomposites.

X-ray diffractograms of the LDPE/Mfensi clay nanocomposites as well as that of LDPE/ Aferi clay nanocomposites showed the best modified clay dispersion in LDPE matrix at 2 wt% clay loadings. But comparing LDPE/ Mfensi clay nanocomposites to LDPE/ Aferi clay nanocomposites, X-ray diffractogram showed LDPE/ Aferi clay nanocomposite to have the best modified clay dispersion in the LDPE matrix.

Finally, results from FT-IR spectra, X-ray diffractograms and crosslink density plots of the LDPE/Mfensi clay nanocomposites and LDPE/Aferi clay nanocomposites, showed that, modified Mfensi and Aferi clay particles did not form any chemical bond with the LDPE molecules, also, the clay galleries were not intercalated by both the surfactant and LDPE molecules, which resulted in the decrease in crosslink densities of the nanocomposites formed. Therefore it is concluded that, the structure of LDPE/Mfensi clay nanocomposites and LDPE/Aferi clay nanocomposites formed, is a phase separated structure.

Even though clay layers were not intercalated by both surfactant and LDPE molecules, the composite formed is regarded as a nanocomposite because, average particle size of fillers used was in the nanometer scale.

5.2 Recommendations

From discussions and conclusions made, the following suggestions are given as recommendations.

Dispersion of modified clay particles in polymer matrix should be confirmed using other techniques such as microscopy, TEM and SEM. The extent of dispersion using processing methods such as high shear melt mixing (such as extrusion) will improve the behavior of the composites and may lead to increased loadings of the clays.

Also further research should be conducted to explore the influence of dispersion on the mechano-physico properties of the nanocomposites formed.

REFERENCES

Ahmad M.B., Hoidy W.H., Ibrahim N.A.B. and Al-Mulla E.A.J. (2009). Modification of montmorillonite by new surfactants, *Journal of Engineering and Applied Science*, Vol. 4, No.3, pp184-188.

Alexandre M., Beyer G., Henrist C., Clout R., André R., Robert J., and Philippe D. (2001). "One-Pot" Preparation of Polymer/Clay nanocomposites starting from Na⁺ Montmorillonite: Melt Intercalation of Ethylene-Vinyl Acetate Copolymer, *Chemistry Mater*, Vol. 13, No.11, pp3831.

Al-Saleh M.H. and Sundararaj U. (2010). Processing-microstructure-property relationship in conductive polymer nanocomposites, *Journal of Polymer*, Vol. 51, pp2740-2747.

Amanda M., Damião L.E., Maria A., Rene A., Osanildo D.P., Hélio L.L., and Edson N.I. (2009). Structure and Mechanical Properties of Polyamide 6/ Brazilian Clay Nanocomposites, *Journal of Materials Research*, Vol. 12, No. 2, pp165-168.

Amit B. and Paramita R. (2009). Basic Features and Techniques, Polymer Grafting and Crosslinking. 1st edition, *John Wiley & Sons*, Inc. Hoboken, New Jersey, pp 8.

Aráujo E.M., Barbosa R., Rodrigues A.W.B., Melo T.J.A., and Ito E.N. (2007). Processing and characterization of polyethylene/Brazilian clay nanocomposites, *Materials Science and Engineering*, Vol. A, pp141–147.

Armentano, I., Dottori, M., Fortunati, E., Mattioli, S. and Kenny, J.M. (2010). Biodegradable polymer matrix nanocomposites for tissue engineering: A review. *Polymer Degradation and Stability*, Vol. 104, In Press.

Arunvisut S., Sutthipat P., and Anongnat S. (2007). Effect of Clay on Mechanical and Gas Barrier Properties of Blown Film LDPE/Clay Nanocomposites, *Journal of Applied Polymer Science*, Vol. 106, pp 2210–2217.

Billmeyer F. W., Jr. (1984). Crosslinking, Textbook of Polymer Science. 3rd edition, *John Wiley and Sons*, New York, pp 120.

Borden, D., and Giese, R.F. (2001). Baseline studies of the Clay Minerals Society source clays: cation exchange capacity measurements by the ammonia-electrode method, *Clays and Clay Minerals*, Vol. 49, No.5, pp 444–445.

Bottino F. A., Pasquale Di G., Fabbri E., Orestano A., and Pollicino A. (2009). Influence of montmorillonite nano-dispersion on polystyrene photo-oxidation, *Polymer Degradation and Stability*, Vol. 94, pp369-374.

Buhrke V. E., Jenkins R, and Smith D. K. (1998). A Practical Guide for the Preparation of Specimens for X-ray Fluorescence and X-ray Diffraction Analysis, *John Wiley & Sons Incorporated*, pp 23-31.

Callister William (2007). Materials Science and Engineering: An Introduction, Seventh edition, *John Wiley and Sons Incorporated*, pp 66-70.

Camberato J.J. (2001). Cation Exchange Capacity – Everything You Want to Know and Much More, *South Carolina Turfgrass Foundation News*, pp 1-4.

Carlsson L.A., and Pipes, R.B. (1987), Experimental Characterization of Advanced Composite Materials, *Prentice-Hall Incorporated*, New Jersey, , pp. 91-93.

Chigwada G., Wang D., Jiang D.D. and Wilkie C.A. (2006). Styrenic nanocomposites prepared using a novel biphenyl-containing modified clay, *Polymer Degradation and Stability*, Vol. 91, pp 755-762.

Choi W.M., Tae W.K., Park O.O., Yong K.C., and Jin W.L., (2003). Preparation and Characterization of Poly(hydroxybutyrate-co-hydroxyvalerate)/Organoclay Nanocomposites, *Journal of Applied Polymer Science*, Vol. 90, pp 525–529.

Coats J. (2000). Interpretation of Infrared Spectra; A Practical Approach. *Encyclopedia of Analytical Chemistry*, R.A.Meyers Edition, pp 10815-10837.

Coleman P.B. (1993), Practical Sampling Techniques for Infrared Analysis, *CRC Press, Boca Raton*, pp 49–91.

Cosoli P.S.G., Pricl, S. and Fermaglia M., (2008). Many-scale molecular simulation for ABS-MMT nanocomposites: Upgrading of industrial scraps, *Microporous and Mesoporous Materials*, Vol. 107, 169-179.

Cunyue G., Zhi M., Mingge Z., Aihua H., Yucai K. and Youliang H., (2002). Preparation of PE/MMT nanocomposite by monomer intercalation and in situ copolymerization, *Chinese Science Bulletin*, Vol. 47, No. 15, pp 1267-1269.

Dhruba J.H., and Nikhil K.S., (2011). Synthesis of Poly(2-ethylhexyl acrylate)/ Clay Nanocomposite by In Situ Living Radical Polymerization, *Journal of Polymer Science, Part A: Polymer Chemistry*, Vol. 49, pp 1564–1571.

Flohr J.K.M., (1997). X-ray Powder Diffraction, *USGS Science for a Changing World*, Vol. 23, pp 1-2.

Gacitua W.E., Ballerini A.A. and Zhang J. (2005). Polymer nanocomposites: synthetic and natural fillers; A review. *Ciencia tecnologia*, Vol. 7, No. 3, pp 159-178.

Giannelis E.P. (1996). Polymer layered silicate nanocomposites. *Advances in Materials*, Vol. 8, pp 29–35.

Giesecking J. (1975), Soil Components - Inorganic Components, *Springer-Verlag, New York*, Vol. 2, pp 156-183.

Gilman J. W. (1999), Flammability and thermal stability studies of polymer layered-silicate (clay) nanocomposites, *Journal of applied clay science*, Vol. 15, pp 31-35.

Greenland D.J. and Hayes M.H.B. (1978). The Chemistry of Soil Constituents, 1st edition, *John Wiley, New York*, pp 46-53.

Grieken R., and Markowicz A. (2002). Handbook of X-ray Spectrometry, 2nd edition, *CRC Press, Boca Raton, FL*, pp 35-42.

Groosjord N., Loos J., Laake L., Maugey M., Zakri C., Koning C.E. and Hart A.J. (2008). High-conductivity polymer nanocomposites obtained by tailoring the characteristics of carbon nanotube fillers, *Advances in Functional Materials*, Vol. 18, pp 3226-3234.

Gupta R.K. and Bhattacharya S.N. (2008). Polymer-clay Nanocomposites: Current Status and Challenges, *Journal of Indian Chemical Engineers*, Vol. 50 No. 3, pp 243-244.

Haraguchi K. (2011). Synthesis and properties of soft nanocomposite materials with novel organic/inorganic network structures. *Polymer Journal*, Vol. 43, pp 223–241.

Hess, P. R. (1994). A text book of soil chemical analysis. 2nd edition, *CBS Publishers and Distributors, Delhi-India*, pp 88-102.

Hussain F., Hojjati M., Okamoto M. and Gorga R.E. (2006). Review article: Polymer-matrix nanocomposites, processing, manufacturing, and Application: An Overview. *Journal of Composite Materials*, Vol. 40, No. 17, pp 1511-1565.

Ishida H., Sandi C., and John B. (2000). General Approach to Nanocomposite Preparation. *Chemical Material*, Vol. 12, No. 5, pp 1260-1261.

Jenkins R., Gould R.W., and Gedcke D. (2000). Applied Spectroscopy, *Applied Spectroscopy Reviews*. Vol. 35, No.1, pp 129-150.

Jordan, J., Jacob K.I., Tannenbaum R., Sharaf M. A. and Jasiuk I. (2005). Experimental trends in polymer nanocomposites-a review. *Material Science Engineering*, Vol. 393, pp1-11.

Jyh M.H., George J.J., Zong M.G., Wei X., Wei P.P. (2002). The Characterization of Organic Modified Clay and Clay-Filled PMMA Nanocomposite, *Journal of Applied Polymer Science*, Vol. 83, pp1702–1710.

Kandilioti G., Elenis A., Macchiarola A. K., and Gregoriou G. V. (2006). Photooxidative Degradation and Conformational Changes in Syndiotactic Polypropylene/Clay Nanocomposites. *Applied Spectroscopy*, Vol. 60, No.11, pp 1285-1292.

Kato M., Usuki A., Hasegawa N., Okamoto H. and Kawasumi M. (2011). Development and applications of polyolefin- and rubber-clay nanocomposites, *Polymer Journal*, Vol. 43, pp 583–593.

Keun-byoung Y., Ho-dong S., Young-young H., Seok K.N., and Dong-ho L. (2007). Modification of montmorillonite with oligomeric amine derivatives for polymer nanocomposite preparation. *Journal of Applied Clay Science*, Vol. 38, pp 1–8.

Kloprogge J.T., Komarneni S., and Amonette J.E. (1999). Synthesis of smectite clay minerals: a critical review. *Clay Minerals*, Vol. 47, pp 529.

Kornmann, X., Linderberg H., and Bergund, L.A. (2001). Synthesis of Epoxy-Clay Nanocomposites: Influence of the Nature of the Curing Agent on Structure. *Journal of Polymers*, Vol. 42, pp 4493–4499.

Kumar A.P., Depan D., Tomer N.S. and Singh R.P. (2009). Nanoscale particles for polymer degradation and stabilization-Trends and future perspectives. *Progress in Polymer Science*, Vol. 34, pp 479-515.

Lagaly, G. (1986). Interaction of alkylamines with different types of layered compounds. *Solid State Ionics*, Vol. 22, pp 43–51.

Lan T.; Kaviratna P.D. and Pinnavaia T.J. (1995). Mechanism of clay tactoid exfoliation in epoxy-clay nanocomposites. *Chemical Mater*, Vol. 7, No.11, pp 2144–2150.

LeBaron P.C., Wang Z. and Pinnavaia, T.J. (1999). Polymer-layered silicate nanocomposites: an overview. *Applied Clay Science*, Vol. 15, pp 11-29.

Lee Y. H., Wang K. H., Park C. B., and Sain M. (2007). Effects of Clay Dispersion on the Foam Morphology of LDPE/Clay Nanocomposites. *Journal of Applied Polymer Science*, Vol. 103, pp 2129–2134.

López-Manchado M.A., Herrero B. and Arroyo M. (2003). Preparation and characterization of organoclay nanocomposites based on natural rubber. *Journal of Polymer International*, Vol. 52, pp 1070–1077

Ma, H., Xu Z., Tong L., Gu A. and Fang Z. (2006). Studies of ABS-graft-maleic anhydride/clay nanocomposites: Morphologies, thermal stability and flammability properties. *Polymer Degradability and Stability*, Vol. 91, pp 2951-2959.

Mark J.E. (1996). Ceramic reinforced polymers and polymer-modified ceramics. *Polymer Engineering Science*. Vol. 36, pp 2905-2920.

Masaya K., Naoki H., Makoto K., Arimitsu U., and Akane O. (1997). Preparation and Mechanical Properties of Polypropylene-Clay Hybrids. *Macromolecules*, Vol.30, pp 6333-6338.

Meneghetti, P. and Qutubuddin, S. (2006). Synthesis, thermal properties and applications of polymer-clay nanocomposites, *Thermochemical Acta*, Vol. 442, pp 74-77.

Mishra K.J., Il K., and Chang-Sik H. (2003), New Millable Polyurethane/Organoclay Nanocomposite: Preparation, Characterization and Properties, *Macromolecules, Rapid Communication*, Vol. 24, No. 11, pp 671–675.

Mittal, V. (2007), Polypropylene-layered silicate nanocomposites: Filler matrix interactions and mechanical properties. *Journal of Thermoplastic Composite Materials*, Vol. 20, pp 575-599.

Mittal, V. (2009). Polymer Layered Silicate Nanocomposites: A Review. *Materials*, Vol. 2, pp 992-1057.

Morgan B. A., Gilman W. J., and Jackson L. C. (2001), Characterization of the Dispersion of Clay in a Polyetherimide Nanocomposite. *Macromolecules*, Vol. 34, No.8, pp 2735-2738.

Nantana J., Sirirat P., Tossaporn P. (2004). Preparation of Organophilic Montmorillonite and its Application in Alkyd Coatings. *Journal of Metals, Materials and Minerals*, Vol. 13, No.2, pp 65-70.

Nascimento do G.M., Constantino V.R.L., and Temperini M.L.A. (2002). Spectroscopic Characterization of a New Type of Conducting Polymer-Clay Nanocomposite. *Macromolecules*, Vol. 35, pp 7535-7537.

Nicholson J. W. (1994). Crosslinking, The Chemistry of Polymers, 2nd edition, *The Royal Society of Chemistry*, pp 62-65.

Okada A. and Usuki A. (2006), Twenty Years of Polymer-Clay Nanocomposites. *Macromolecular Material Engineering*, Vol. 291, pp 1449–1476.

Olad Ali (2010), Polymer/Clay Nanocomposites: Advances in Diverse Industrial Applications of Nanocomposites, *Progress in Polymer Science*, Vol. 60, pp 115-125.

Pandey J.K., Reddy K.R., Kumar A.P. and Singh R.P. (2005), An overview on the degradability of polymer nanocomposites. *Polymer Degradation and Stability*, Vol. 88, pp 234-250.

Pandey K.J., Reddy K.R., Kumar A.P., and Singh R. P. (2004). An Overview on the degradation of Polymer nanocomposites. *Polymer Degradability and Stability*, Vol. 88, pp 234-250.

Paula, D.R. and Robeson L.M. (2008). Polymer nanotechnology: Nanocomposites, *Polymer*, Vol. 49, pp 3187-3204.

Pavlidou, S. and Papaspyrides, C.D. (2008). A review on polymer-layered silicate nanocomposites, *Progress in Polymer. Science*, Vol. 32, pp1 119-1198.

Quang T. N., and Donald G. B. (2006), Preparation of Polymer–Clay Nanocomposites and Their Properties, *Advances in Polymer Technology*, Vol. 25, No. 4, pp 270–285.

- Ray, S.S. and Okamoto, M. (2003). Polymer/layered silicate nanocomposites: a review from preparation to processing. *Progress in Polymer Science*, Vol. 28, pp 1539-1641.
- Reynaud E., Gauthier C., and Perez J. (1999), Nanophases in polymers, *Information Technology*, Vol. 96, pp 169-176.
- Rezanejad S., and Kokabi M. (2007), Shape memory and Mechanical Properties of cross-linked polyethylene/clay nanocomposites, *European Polymer Journal*, Vol. 43, pp 2856-2865.
- Roelofs J.C.A., and Berben P.H. (2006), Preparation and performance of synthetic organoclays, *Applied Clay Science*, Vol. 33, pp 13–20.
- Salawudeen T. O., Isam Y. Q., Nassereldeem A. K., Ma'an A., Suleyman A. M., Faridah Y., Qasim H. S. (2008), Effect of Modification on the Physicochemical and Thermal Properties of Organophilic Clay Modified with Octadecylamine, *International Journal of Engineering and Technology*, Vol.10, No.1, pp27-34.
- Sánchez-Valdés S., Martínez C. J. G., López-Quintanilla M. L., Yañez F. I., García-Salazar M. L. and González C. C. (2008), Preparation and UV weathering of polyethylene nanocomposites, *Polymer Bulletin*, Vol. 60, pp 829–836.
- Sheng, N., Boyce, M.C., Parks, D.M., Rutledge, G.C., Abes, J.I. and Cohen R.E.. (2004). Multiscale micromechanical modeling of polymer/clay nanocomposites and the effective clay particle. *Polymer*, Vol. 45, pp 487-506.
- Sinha S. R., and Okamoto M. (2003), Polymer/layered silicate nanocomposites: a review from preparation to processing, *Journal of Progress in Polymer Science*, Vol.28, pp 1544.
- Smith B. (1996), *Fundamentals of Fourier Transform Infrared Spectroscopy*. CRC Press, Washington, D.C., pp 23-24.
- Smith B. (1999), *Infrared Spectral Interpretation, A Systematic Approach*. CRC Press, Washington, D.C., pp 34-36.
- Song K. and Sand G. (2001), Characterization of montmorillonite surfaces after modification by organosilane, *Journal of clays and clay minerals*, Vol. 49, No.2, pp 119–125.
- Sposito Garrison (1989). *The Chemistry of Soils, Soil Science*, 3rd Edition, Oxford University Press, pp 23-39.
- Szymanski H.A., and Erickson R.E. (1970), *Infrared Band Handbook*, Plenum Press edition, New York, Vol. 2, pp 1-10.
- Thostenson, E.T., Li C., and Chou T.W. (2005). Nanocomposites in context. *Composite Science and Technology*, Vol. 65, pp 491-516.

Usuki, A., Kawasumi M., Kojima Y., Okada, A., Kurauchi T. and Kamigaito O. J. (1993). Swelling behavior of montmorillonite cation exchanged for V-amino acids by Ecaprolactam. *Material Research*, Vol. 8, No.5, pp 1174.

Vaia R.A., Liu W.D., and Koerner H. (2003). Analysis of small-angle scattering of suspensions of organically modified montmorillonite: implications to phase behavior of polymer nanocomposites. *Journal of Polymer Science, Bulletin of Polymer Physics*, Vol. 41, pp 3214–3236.

Vaia, R.A. and Liu, W.D. (2002). X-ray powder diffraction of polymer/layered silicate nanocomposites: model and practice. *Journal of Polymer Science, Bulletin of Polymer Physics*, Vol. 40, pp 1590–1600.

Wahit M. U., Balakrishnan H., Muthmirah L., and Azman H. (2011). Improved polypropylene / clay nanocomposites, *Society of Plastics Engineers, plastic research online*, pp 1-3.

Wang K., Liang S., Du R.N., Zhang, Q., and Fu Q. (2004). The interplay of thermodynamics and shear on the dispersion of polymer nanocomposite. *Polymer*, Vol. 45, pp 7953–7960.

Wang Z. M., Chung T. C., Gilman J. W., and Manias E. (2003). Melt-Processable Syndiotactic Polystyrene/Montmorillonite Nanocomposites, *Journal of Polymer Science: Part B: Polymer Physics*, Vol. 41, pp 3173–3187.

Wentao L., Xingyou T., Ping C., Yong L., Kang Z., and Ye Y. (2004). Preparation and Characterization of PET/Silica Nanocomposites, *Journal of Applied Polymer Science*, Vol. 91, pp 1229–1232.

Werne T. V., and Patten T.E. (1999). Preparation of structurally well defined polymer±nanoparticle hybrids with controlled/ living radical polymerization, *Journal of American Chemical Society*, Vol. 121, pp 7409-7410.

Xu W. B., Zhai H. B., Guo H. Y., Zhou Z. F., Whitely N. and Pan W.P. (2004). PE/ORG-MMT Nanocomposites: Non-isothermal crystallization kinetics, *Journal of Thermal Analysis and Calorimetry*, Vol. 78, pp 102.

Yixiang X., and Milford A. H. (2006). Chitosan/Clay Nanocomposite Film Preparation and Characterization, *Journal of Applied Polymer Science*, Vol. 99, pp 1684–1691.

Yong-Hyun J., Hong-Jo P., Seung-Soon I., Seung-Yeop K., and Soonjong K. (2002). Polyethylene/Clay Nanocomposite by In-Situ Exfoliation of Montmorillonite during Ziegler-Natta Polymerization of Ethylene. *Macromolecules, Rapid Communications*. Vol. 23, No. 2, pp 135-140.

Zhang J., Manias E., and Wilkie C. A. (2008). Polymerically Modified Layered Silicates: An Effective Route to Nanocomposites, *Journal of Nanoscience and Nanotechnology*, Vol. 8, pp 1608.

Zhang X., Bhuvana S., and Loo L. S. (2011). Characterization of Layered Silicate Dispersion in Polymer Nanocomposites Using Fourier Transform Infrared Spectroscopy, *Journal of Applied Polymer Science*, Vol. 000, pp 000–000, Wiley Periodicals, Incorporated.

Zhang, R., Ni, Q., Natsuki, T. and Iwamoto, M. (2007). Mechanical properties of composites filled with SMA particles and short fibers. *Composite Structures*, Vol. 79, pp90-96.

Zhang, Z. and Friedrich, K. (2003). Artificial neural networks applied to polymer composites: a review”. *Composite Science and Technology*, Vol. 63, pp2029-2044.

Zhao C., Meng F., Fangling G., Huaili Q., and Mingshu Y. (2004). Preparation and Characterization of Polyethylene–Clay nanocomposites by Using Chlorosilane-Modified Clay, *Journal of Applied Polymer Science*, Vol. 93, pp 676–680.

Zhao C., Qin H., Fangling G., Feng M., Zhang S., and Mingshu Y. (2005). Mechanical, thermal and flammability properties of polyethylene/clay nanocomposites, *Polymer Degradation and Stability*, Vol. 87, pp 183-189.

Zheng H., Zhang Y., Peng Z., and Zhang Y. (2004). Influence of the Clay Modification and Compatibilizer on the Structure and Mechanical Properties of Ethylene–Propylene–Diene Rubber/ Montmorillonite Composites, *Journal of Applied Polymer Science*, Vol. 92, pp 638–646.



APPENDIX

APPENDIX 1: Properties of pristine and modified Aferi and Mfensi clay samples.

Appendix 1.1. Major and minor elements of Pristine Mfensi and Aferi clay samples.

Table A.1.1: Major oxides of Pristine Mfensi Clay, (PMC) and Pristine Aferi Clay, (PAC).

Element	Dimension	PMC	PAC
Na ₂ O	%	2.34	3.19
MgO	%	1.91	3.48
Al ₂ O ₃	%	15.77	24.41
SiO ₂	%	74.49	59.98
P ₂ O ₅	%	0.09	0.21
SO ₃	%	0.16	0.11
Cl	%	0.00	0.00
K ₂ O	%	1.28	0.59
CaO	%	0.11	1.32
TiO ₂	%	0.95	1.07
MnO	%	0.02	0.04
Fe ₂ O ₃	%	3.21	5.94
L.O.I	%	0.50	0.50
TOTAL	%	100.84	100.84

Table A.1.2: Minor elements of Pristine Mfensi Clay, (PMC) and Pristine Aferi Clay, (PAC).

Element	Dimension	PMC	PAC
V	Ppm	500	114
Cr	Ppm	288	266
Co	Ppm	30	69
Ni	Ppm	26.3	126.6
Cu	Ppm	10.8	39.5
Zn	Ppm	55.9	102.6
Ga	Ppm	24	30.5
As	Ppm	1	1.9
Rb	Ppm	67.7	27.9
Sr	ppm	53.8	411.8
Y	ppm	13.8	45.5
Zr	ppm	484.2	470.7
Nb	ppm	15.2	15.5
Mo	ppm	4.3	4.8
Sb	ppm	1.5	1.9
I	ppm	4.5	4.9
Cs	ppm	6.9	7.5
Ba	ppm	350.1	669.8
La	ppm	18.4	114.5
Ce	ppm	58.2	232
Hf	ppm	22.6	8.8
Ta	ppm	6	9.8
Pb	ppm	14.4	22.8

Bi	ppm	2.1	4.6
Th	ppm	8.8	9.6
U	ppm	16.1	19.2

Appendix 1.2 Calculation of Cation Exchange Capacity of clay samples

Below is table A.1.3 showing exchangeable cations of Mfensi and Aferi clay and their total Cation Exchange Capacity.

Table A.1.3.: Calculations of total cation exchange capacity

Sample	Exchangeable Cations meq/ 100g						Total Cation Exchange Capacity (meq/100g)
	Ca	Mg	K	Na	Al	H	
Mfensi	2.00	2.80	0.38	1.89	0.40	2.40	9.87
Aferi	11.00	14.80	0.20	1.33	0.40	2.30	30.03
Modified Mfensi	1.00	1.20	0.25	0.31	0.20	1.10	4.06
Modified Aferi	7.32	7.50	0.13	0.10	0.31	0.95	16.31

APPENDIX 2: Fourier Transform-Infra Red (FT-IR) spectra of octadecylamine, Pristine and Modified, Mfensi and Aferi clay Samples.

Figure A.2.1.: FT-IR Spectrum of Octadecylamine



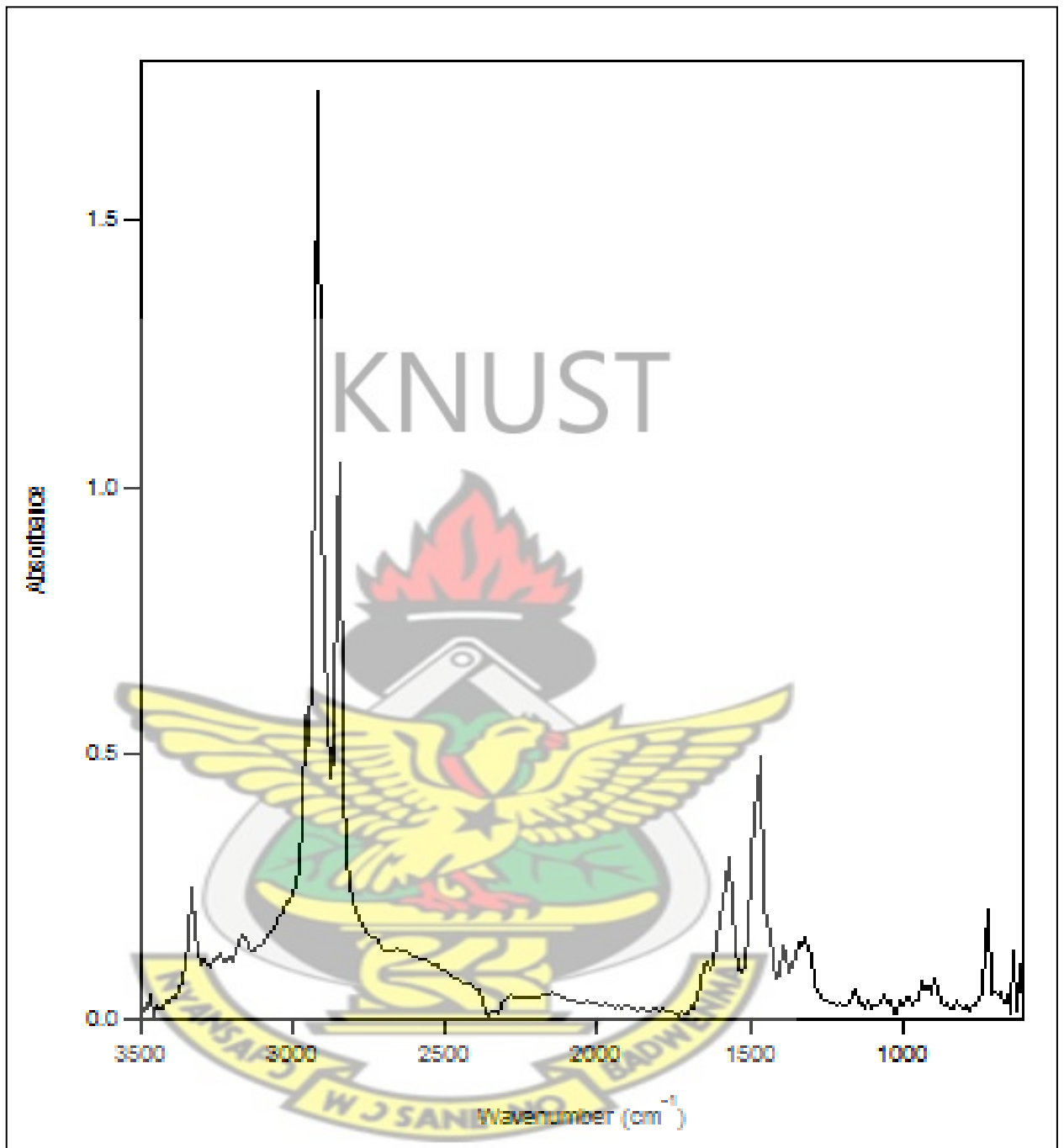


Figure A.2.2: FT-IR Spectrum of Pristine Mfensi Clay.

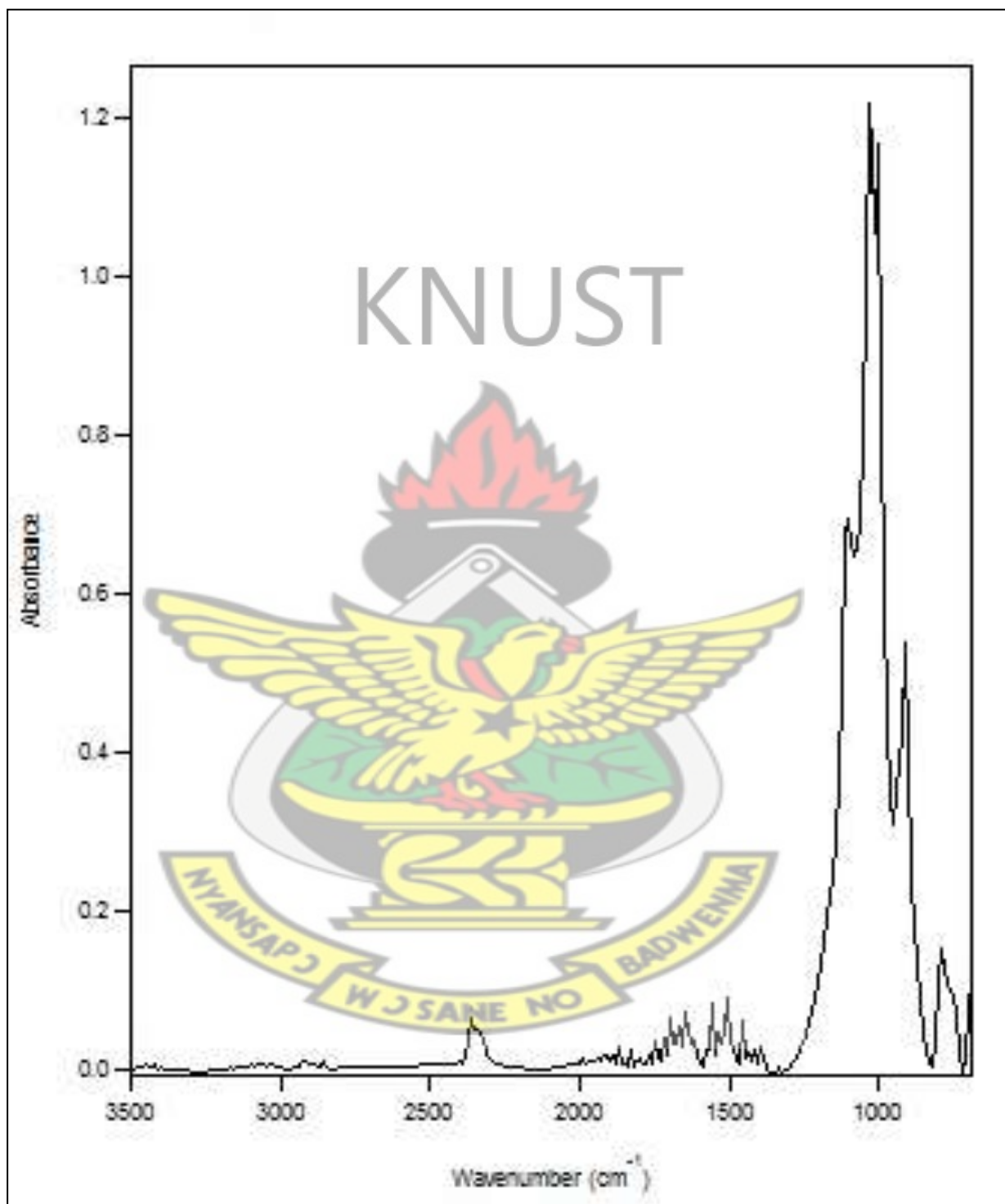
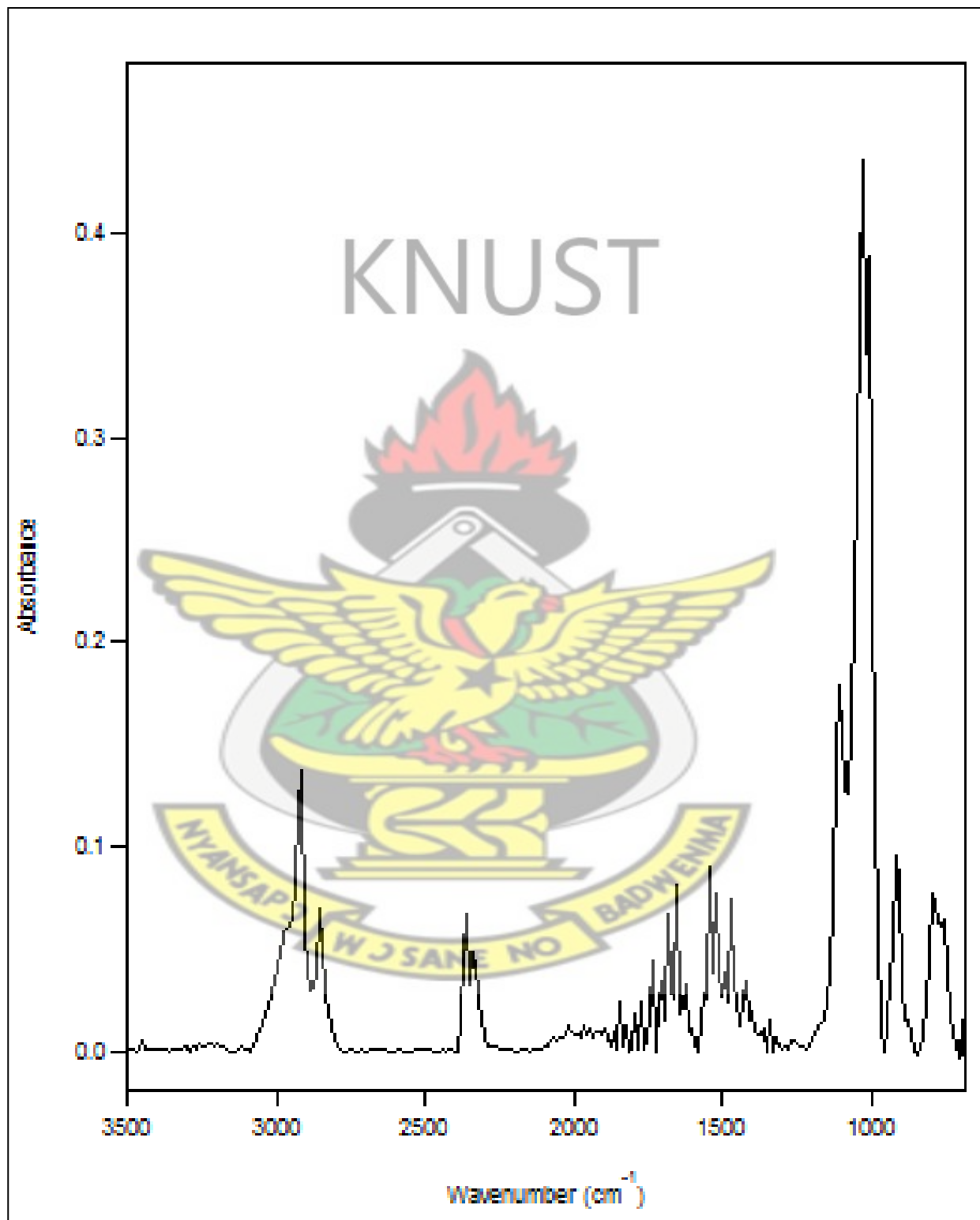


Figure A.2.3.: FT-IR Spectrum of Modified Mfensi Clay.



Appendix 2.1 Absorbance of C-H and Si-O peaks in Modified Mfensi and Aferi clays compared to pristine Mfensi and Aferi clays

Table A.2.1: A table comparing the Absorbance of Characteristic Functional Groups in the Octadecylamine, Pristine and Modified Mfensi and Aferi Clay Samples.

SAMP.		ODA	PMC	MMC	PAC	MAC
FGA	Si-O	0.0000	1.2921	0.1810	2.1638	1.5047
	C-H	1.7325	0.0000	0.1650	0.0000	0.6890

KEY

- Functional Group Absorbance – FGA
- Sample – SAMP.
- Pristine Mfensi Clay - PMC
- Octadecylamine – ODA
- Modified Mfensi Clay – MMC
- Pristine Aferi Clay – PAC
- Modified Aferi Clay - MAC

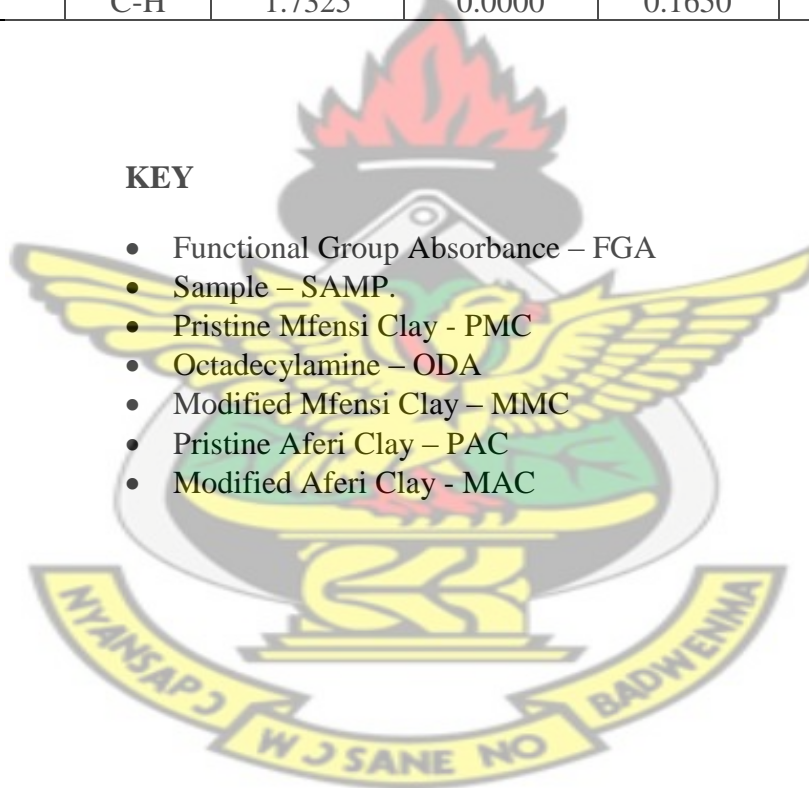


Figure A.2.4. : FT-IR Spectrum of Pristine Aferi Clay.

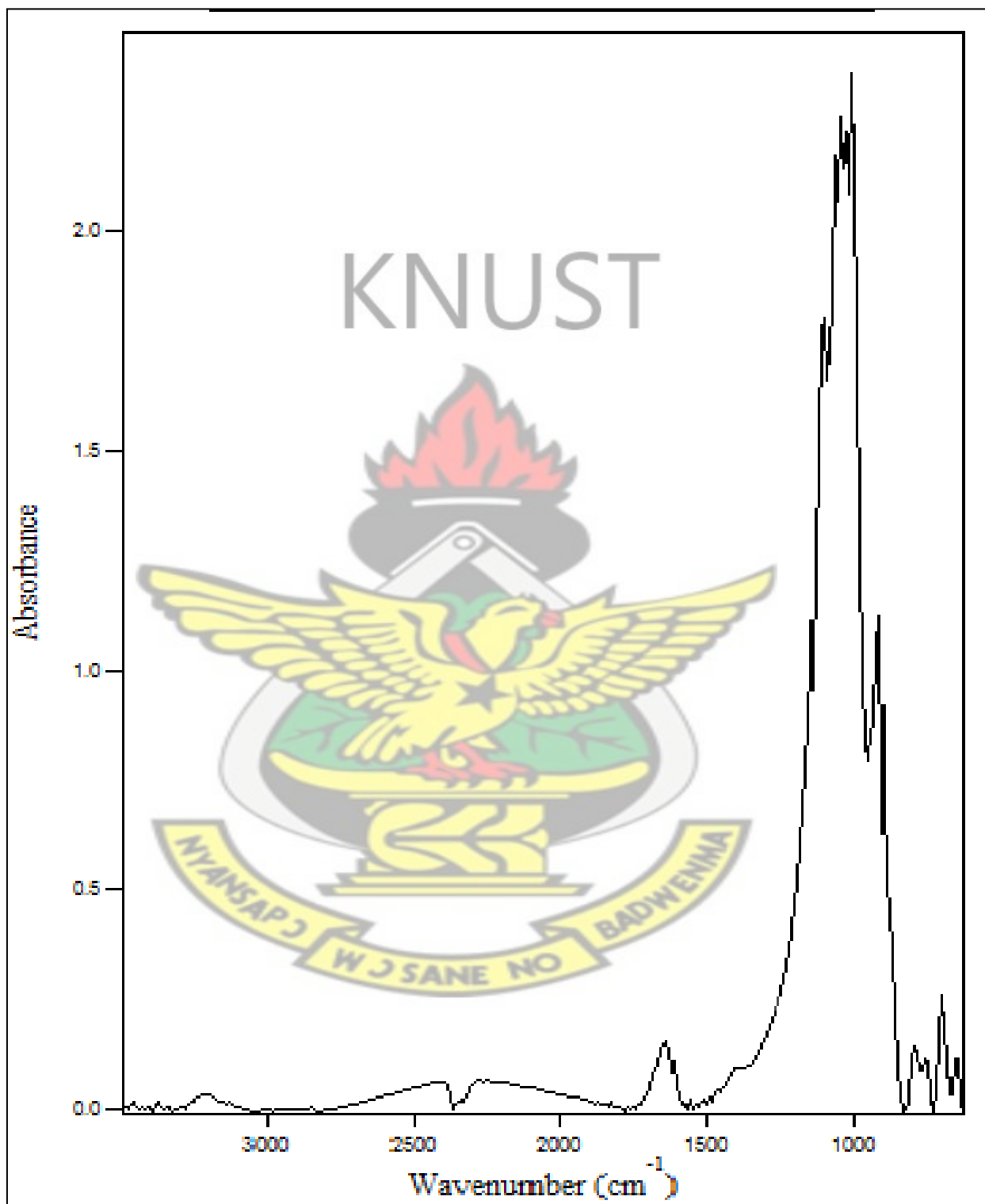
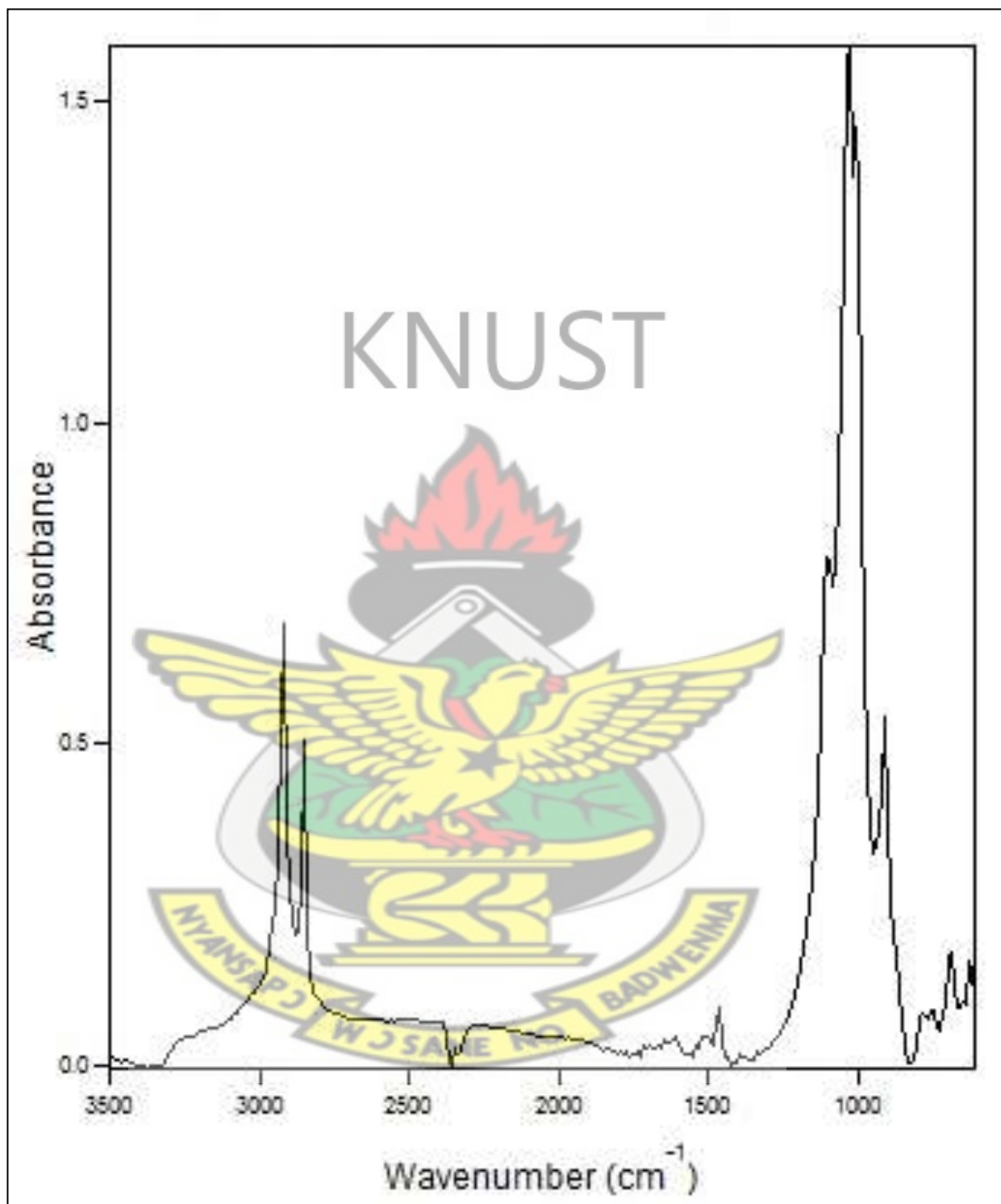


Figure A.2.5. : FT-IR Spectrum of Modified Aferi Clay.

KNUST





APPENDIX 3: Fourier Transform-Infra Red spectra, (FT-IR), of Low Density Polyethylene (LDPE) / Mfensi clay nanocomposites and Low Density Polyethylene/ Aferi clay nanocomposites at different clay loadings.

Figure A.3.1: FT-IR Spectrum of Low Density Polyethylene, (100 wt% P / 0 wt% C).

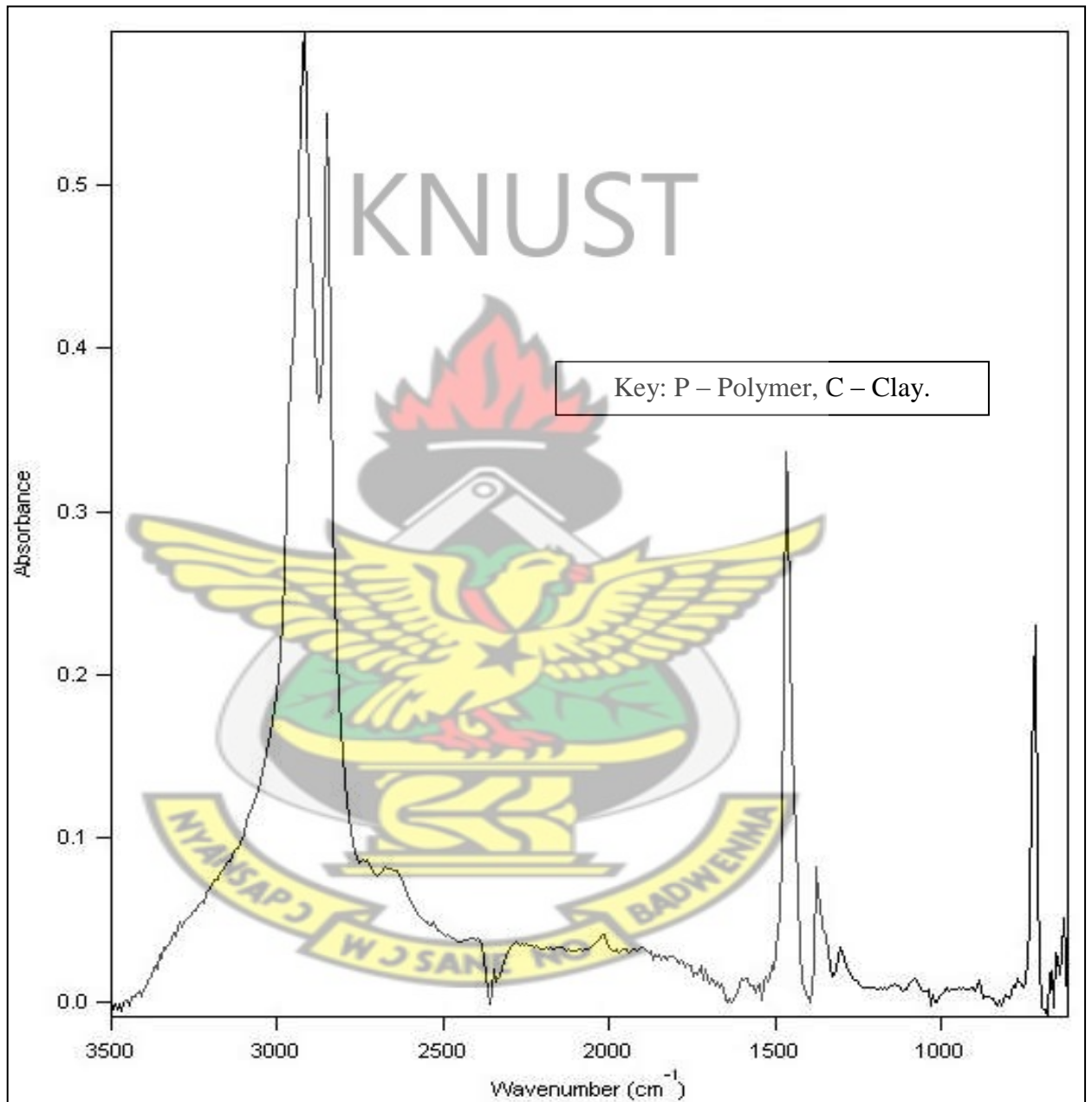


Figure A.3.2: FT-IR Spectrum of 98 wt% LDPE / 2 wt% Mfensi Clay nanocomposite.

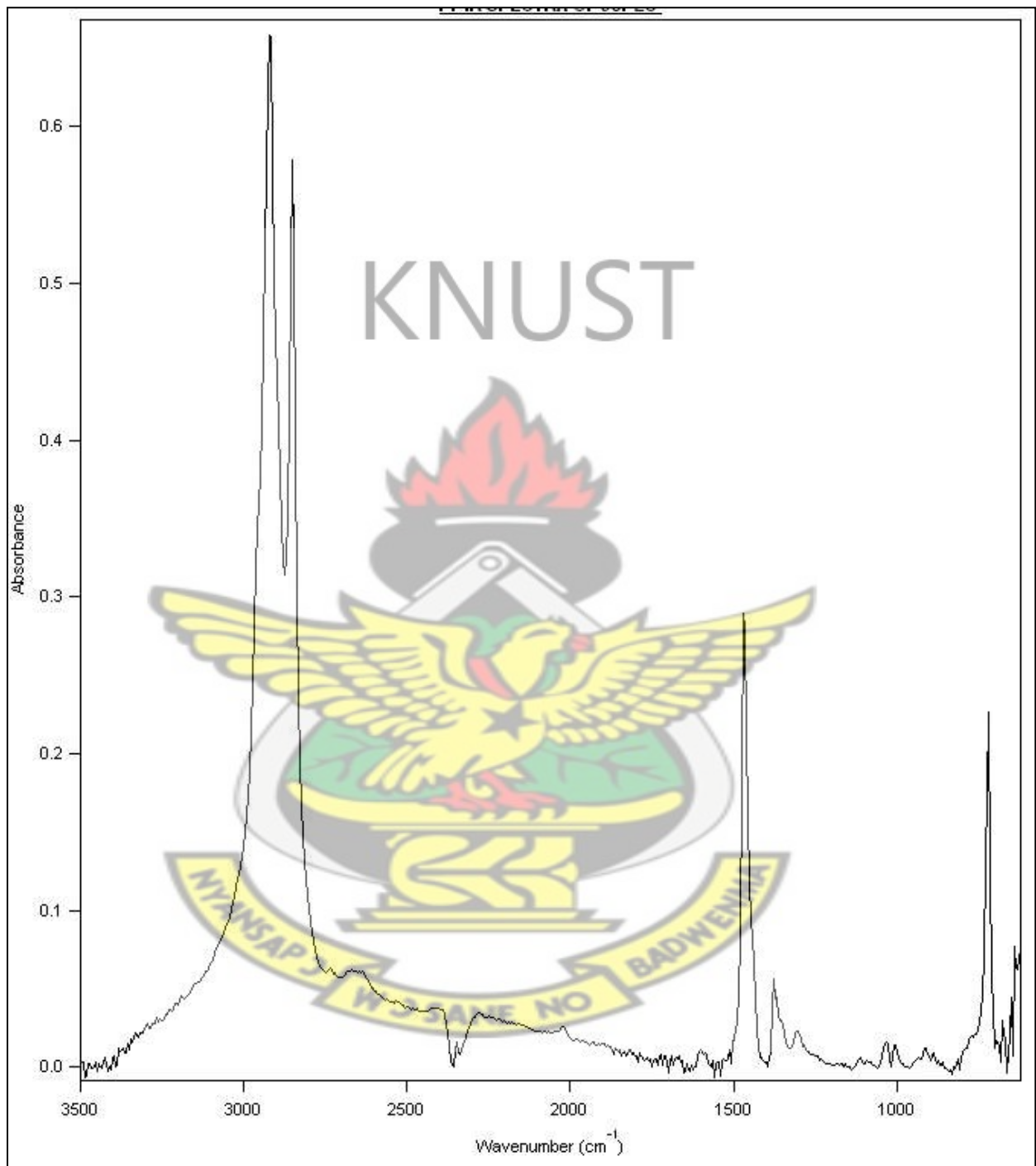


Figure A.3.3: FT-IR Spectrum of 96 wt% LDPE / 4wt% Mfensi Clay nanocomposite.

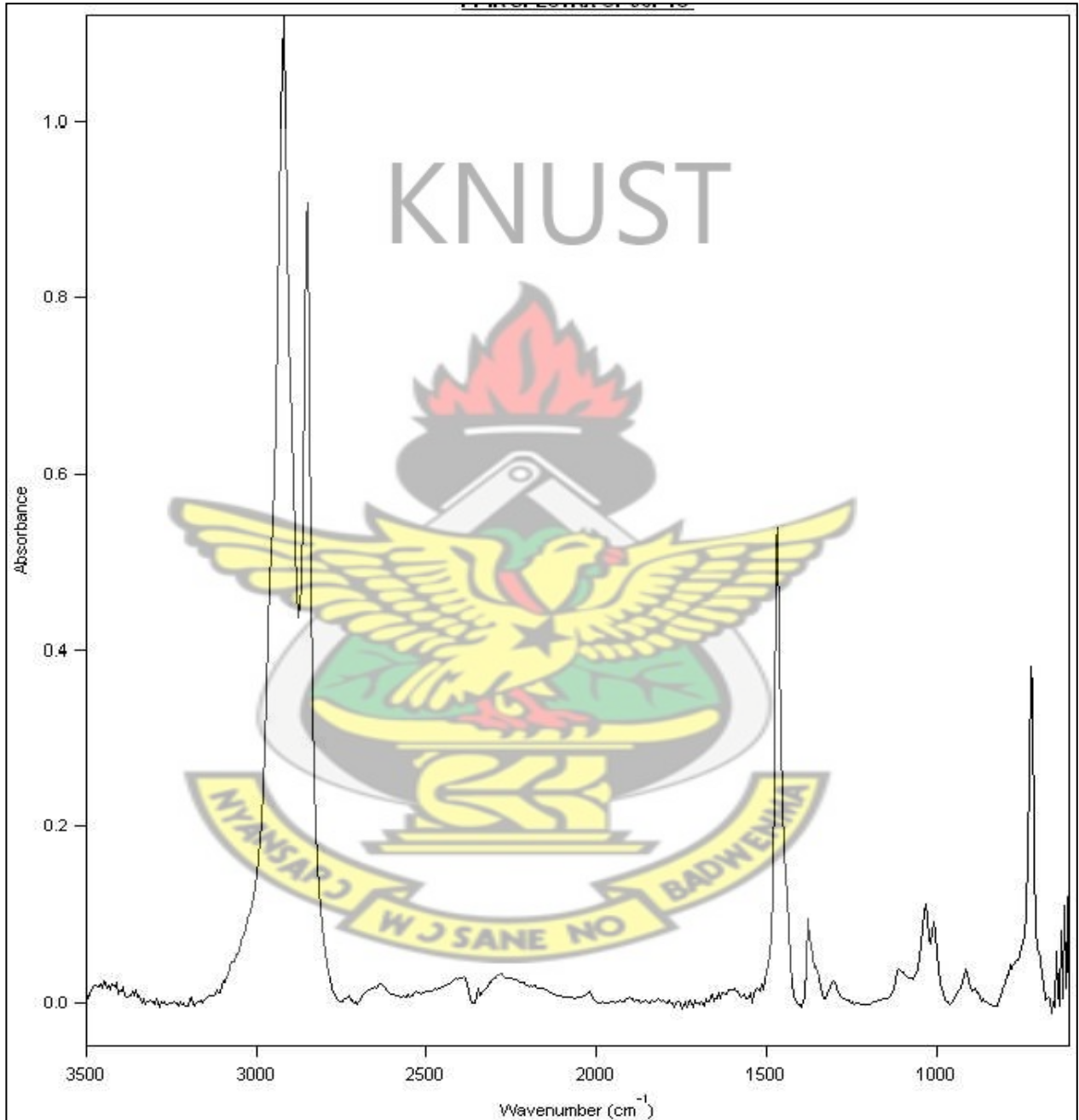


Figure A.3.4: FT-IR Spectrum of 94 wt% LDPE / 6 wt% Mfensi Clay nanocomposite.

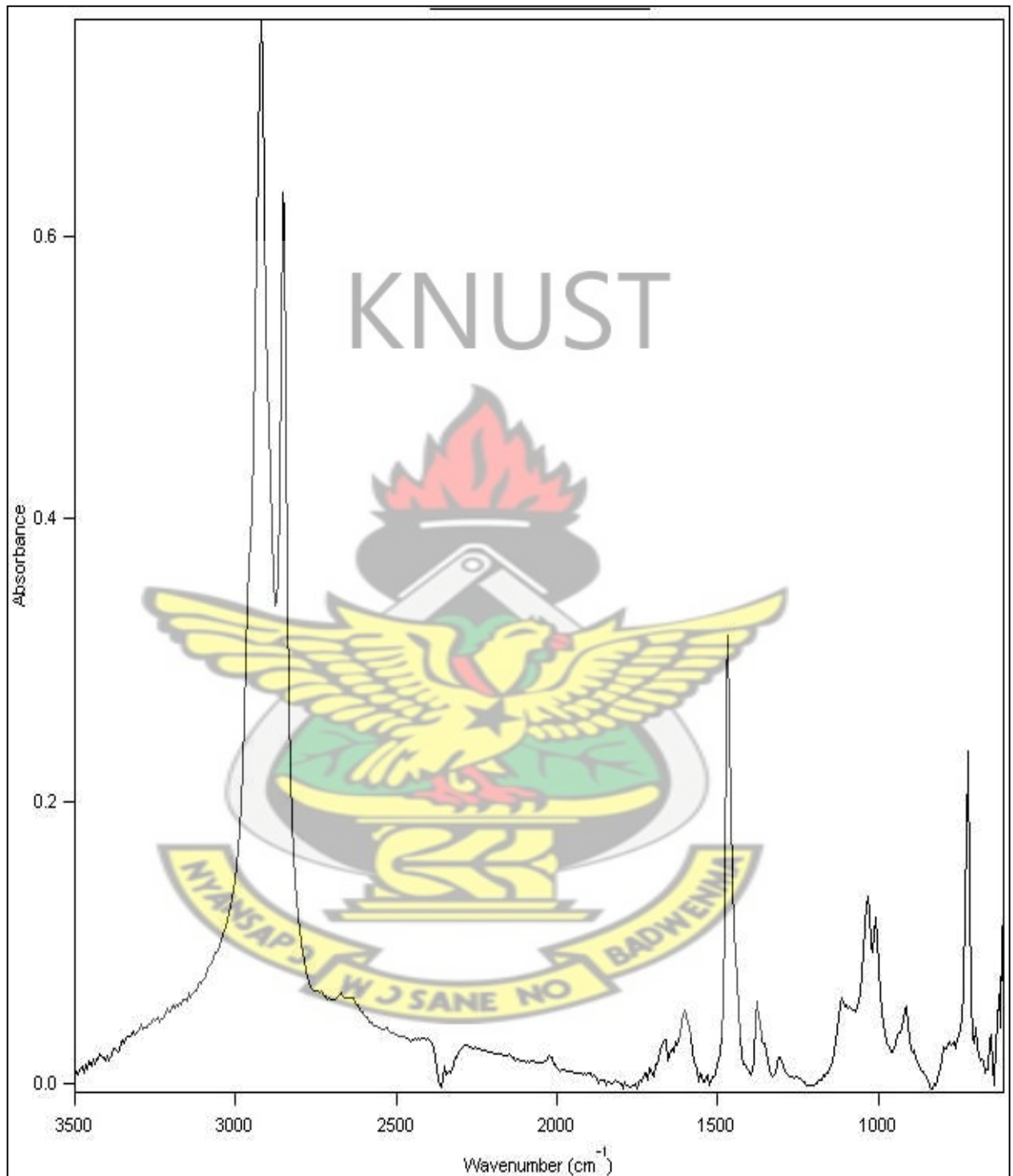


Figure A.3.5: FT-IR Spectrum of 92 wt% LDPE / 8 wt% Mfensi Clay nanocomposite.

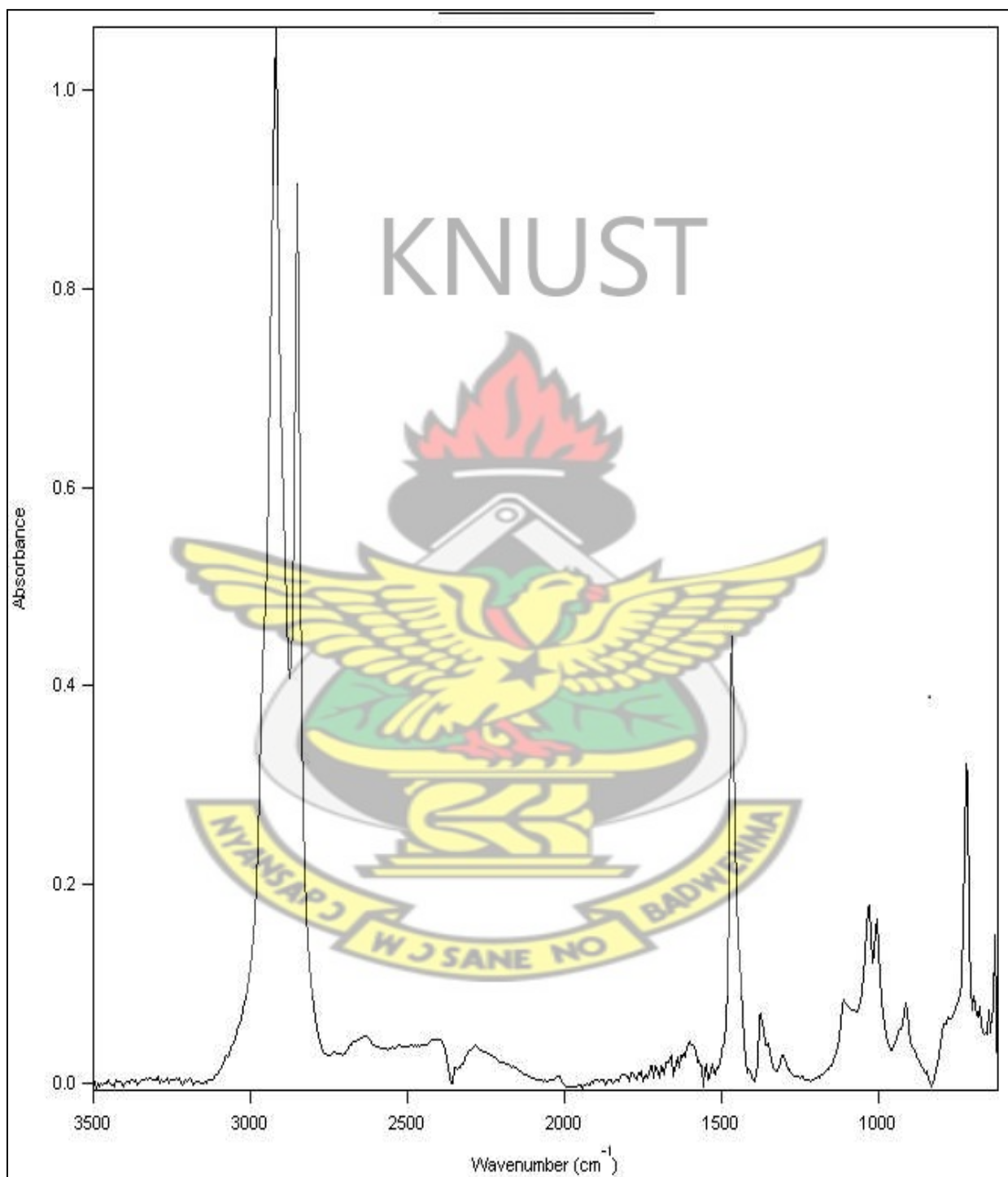
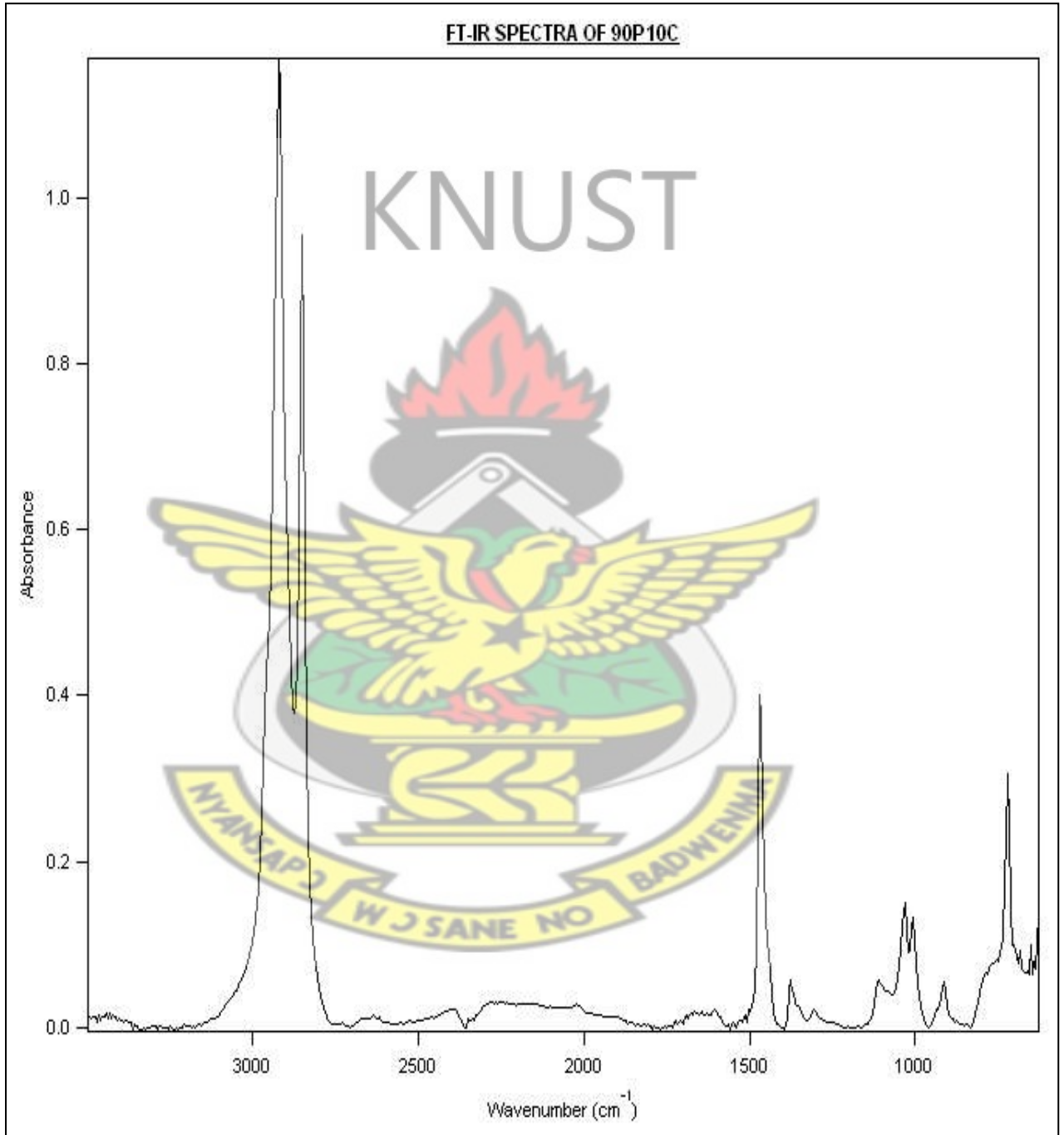


Figure A.3.6: FT-IR Spectrum of 90 wt% LDPE / 10 wt% Mfensi Clay nanocomposite.



Appendix 3.1: Comparison of C-H and Si-O peak absorbance in LDPE/ Mfensi clay nanocomposites at different percentage clay loadings.

Table A.3.1: Absorbance of the C-H and Si-O peaks of LDPE/ Mfensi clay nanocomposites at different percentage Mfensi clay loadings.



ABSORBANCE OF CHARACTERISTIC FUNCTIONAL GROUPS

CLAY LOADINGS (%)	Si-O vibrations	C-H symmetric	C-H asymmetric	C-H bending	C-H rocking
0	0.0000	0.5831	0.5437	0.3430	0.2542
2	0.2016	0.9475	0.7504	0.4198	0.3089
4	0.2298	1.0059	0.8604	0.5264	0.3993
6	0.2727	1.2311	0.9155	0.5549	0.4134
8	0.3354	1.4953	1.3128	0.6756	0.4601
10	0.4348	1.7575	1.3775	0.6994	0.4922

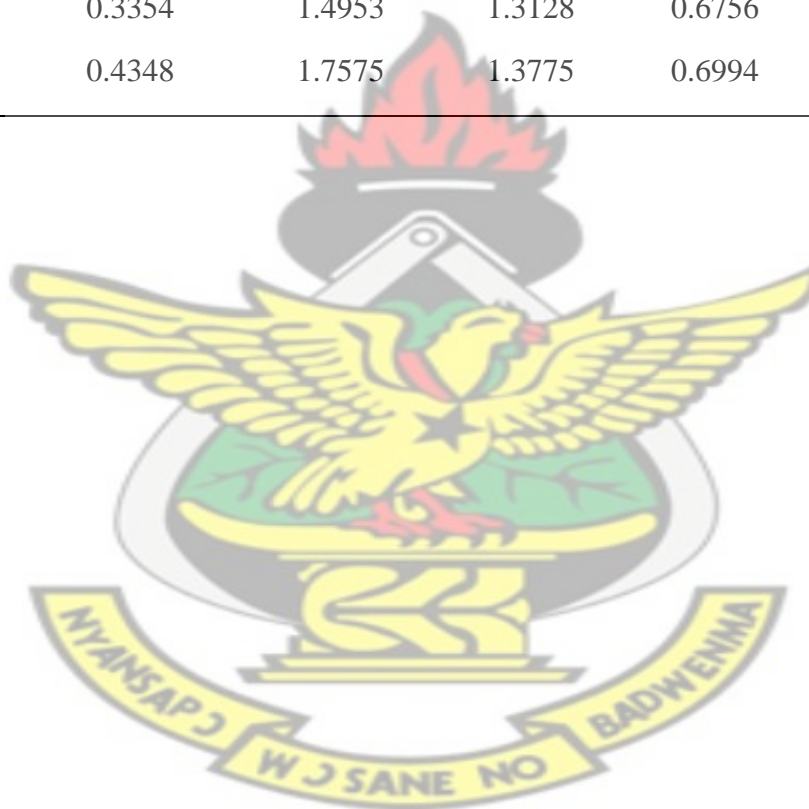


Figure A.3.7: FT-IR Spectrum of 98 wt% LDPE / 2 wt% Aferi Clay nanocomposite.

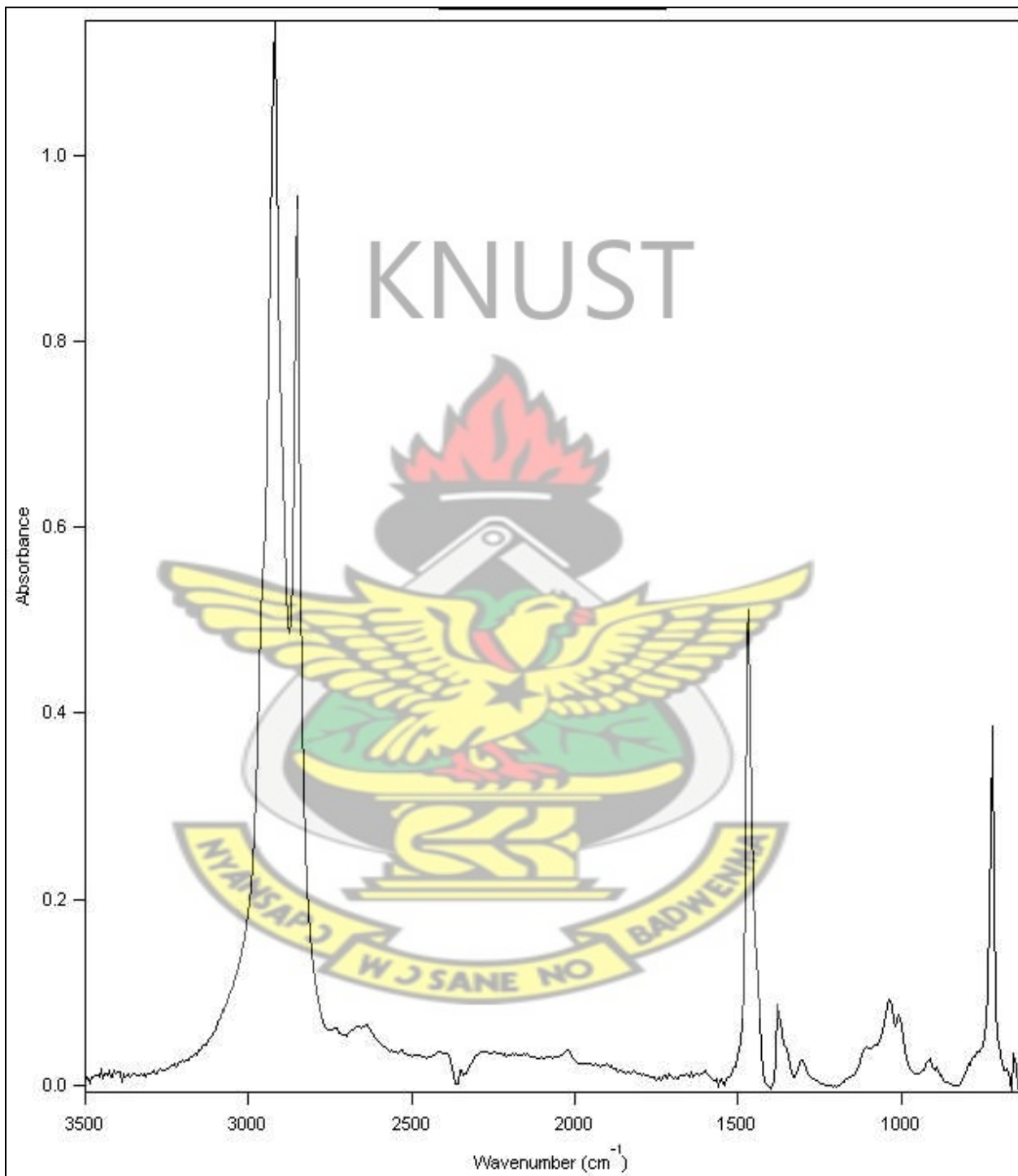


Figure A.3.8: FT-IR Spectrum of 96 wt% LDPE / 4 wt% Aferi Clay nanocomposite.

KNUST



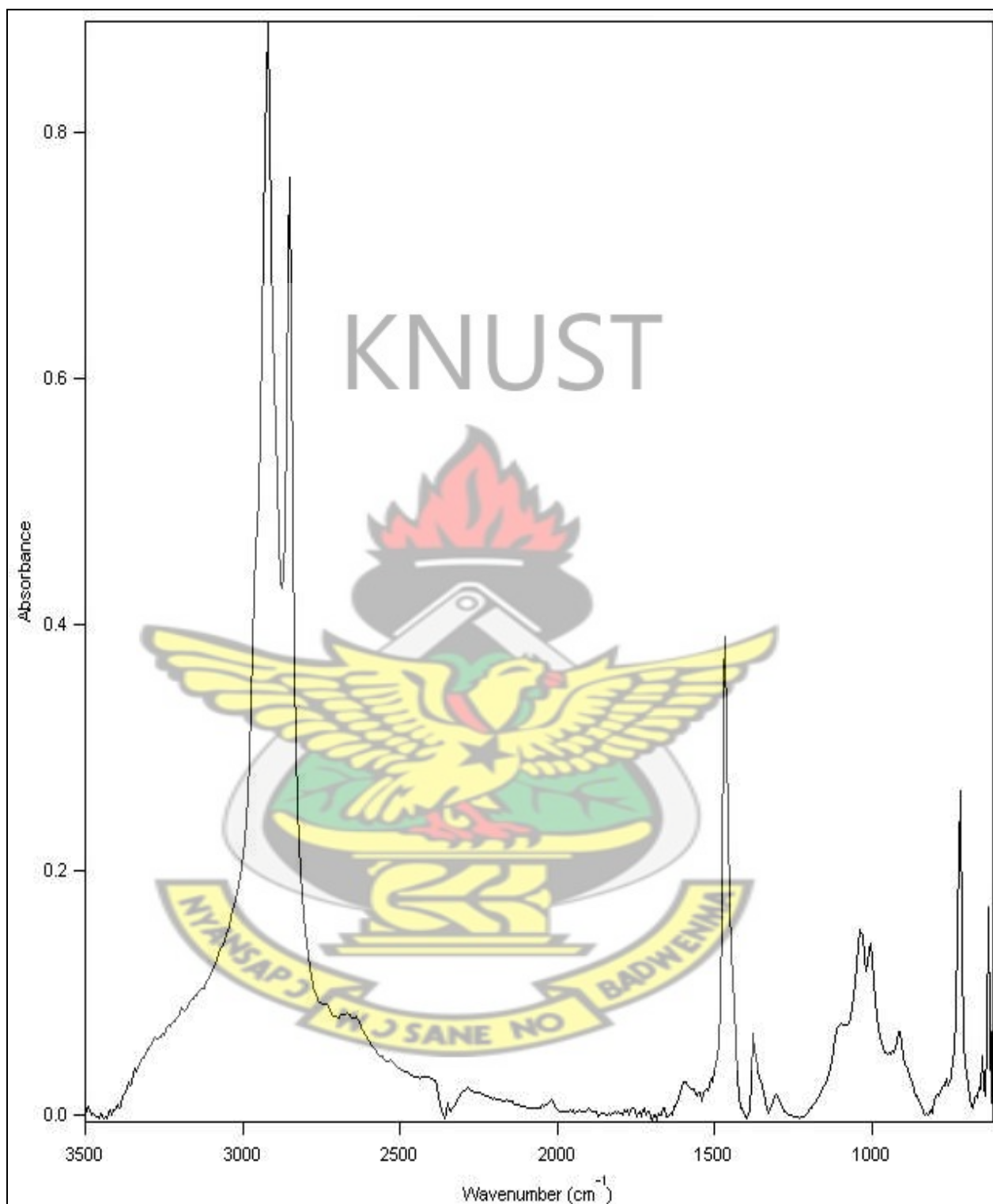


Figure A.3.9: FT-IR Spectrum of 94 wt% LDPE / 6 wt% Aferi Clay nanocomposite.

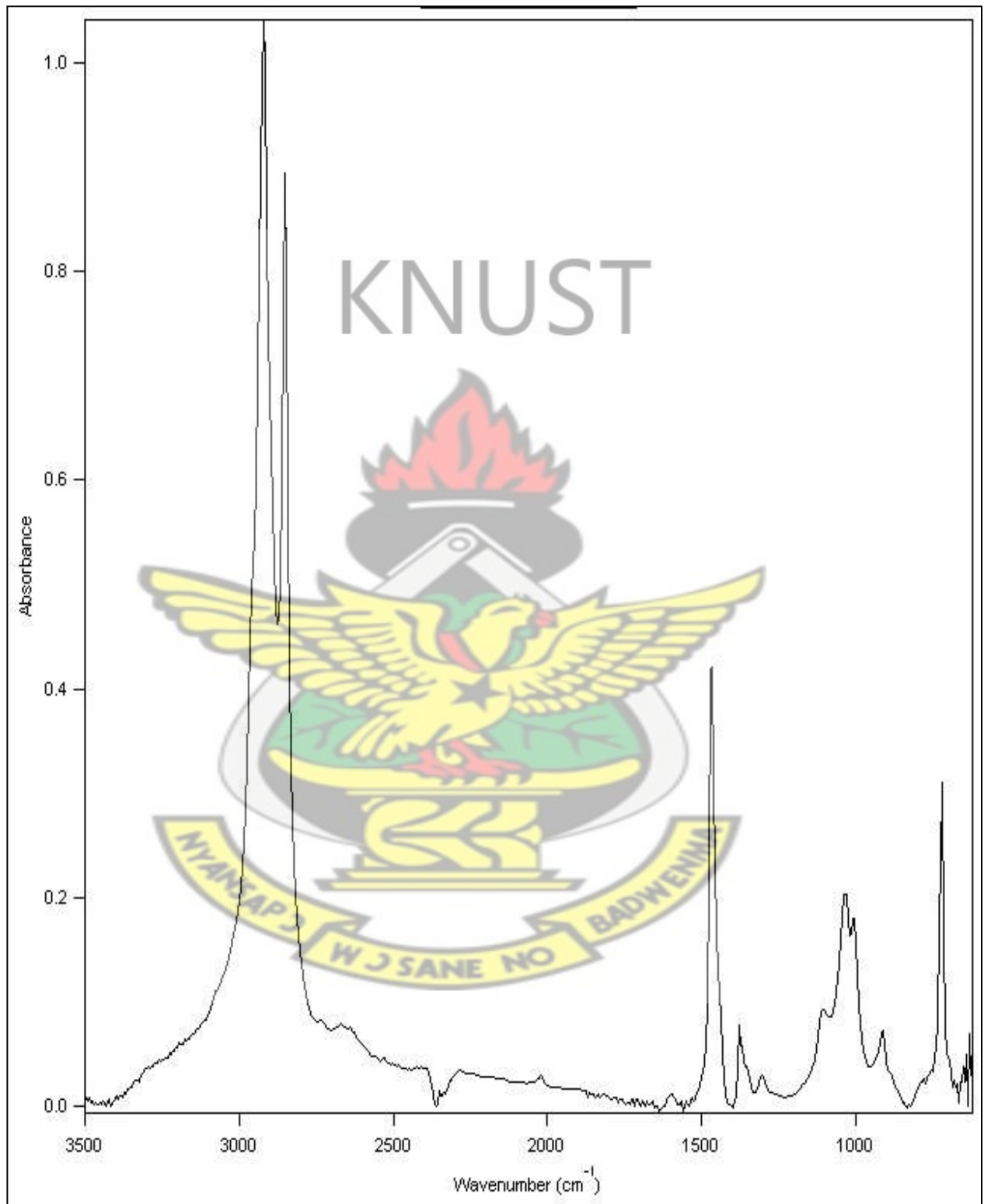


Figure A.3.10: FT-IR Spectrum of 92 wt% LDPE / 8 wt% Aferi Clay nanocomposite.

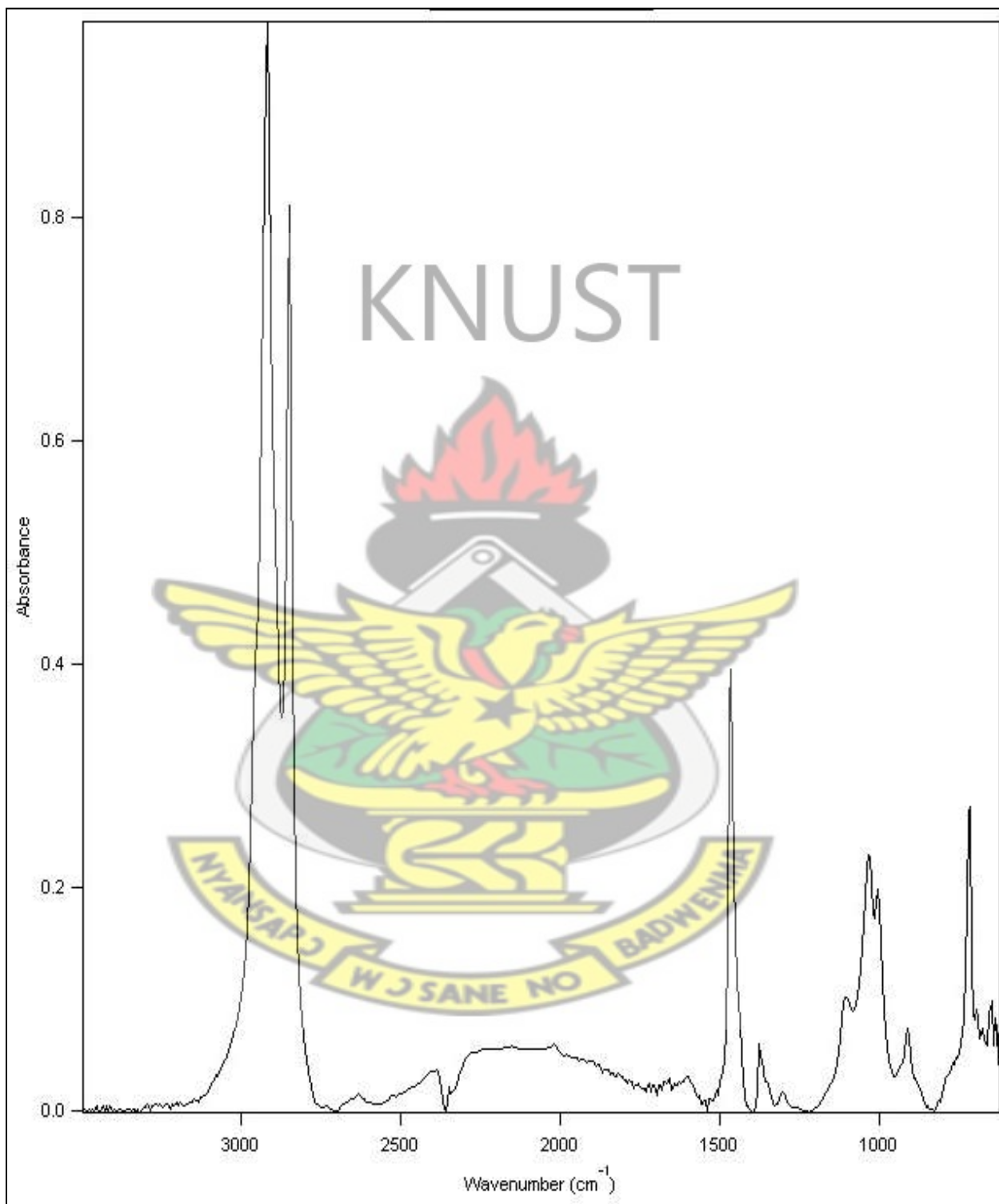
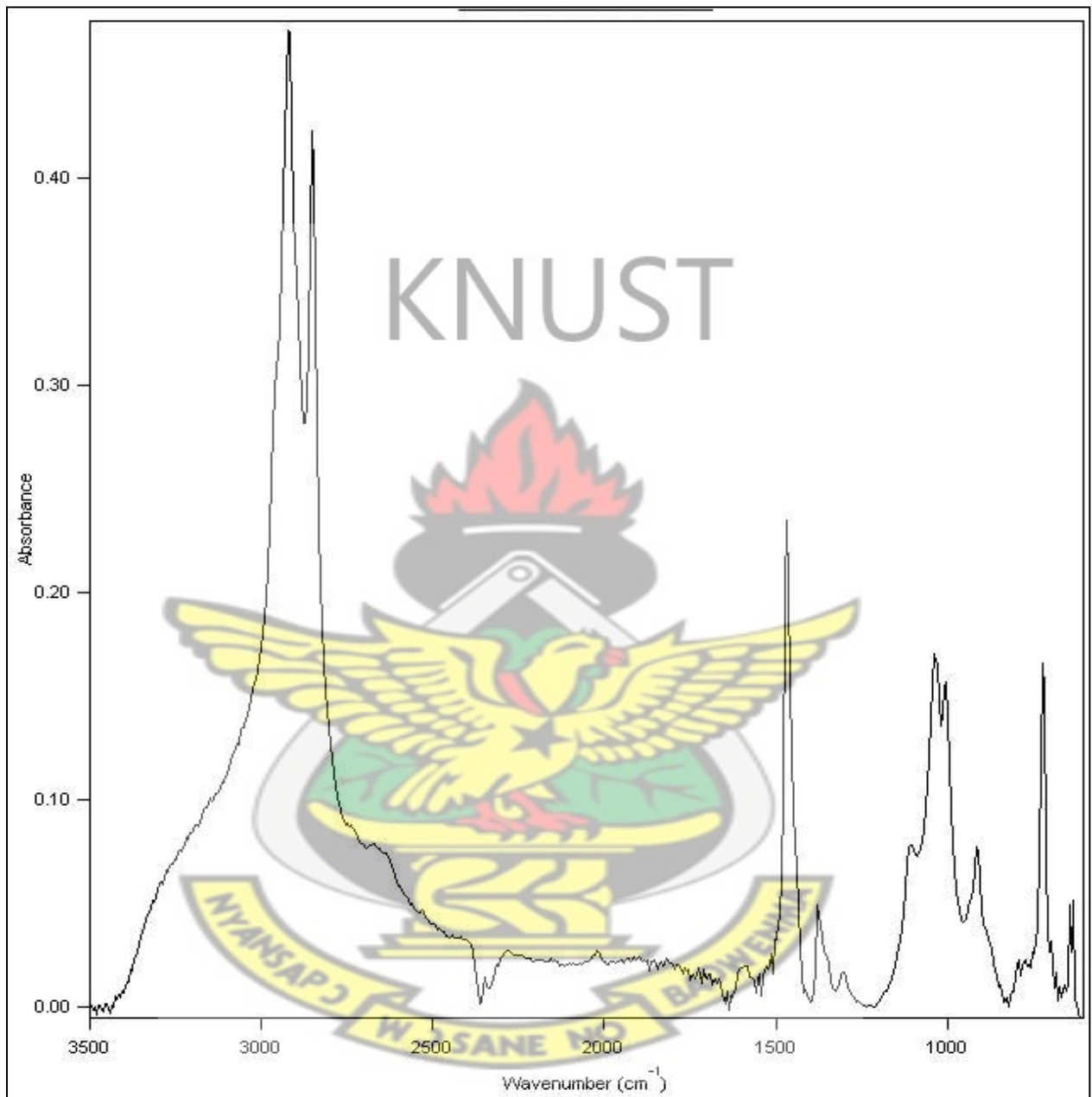


Figure A.3.11: FT-IR Spectrum of 90 wt% LDPE / 10 wt% Aferi Clay nanocomposite.



Appendix 3.2: Comparison of C-H and Si-O peak absorbance in LDPE/ Aferi clay nanocomposites at different percentage clay loadings.

Table A.3.2: Absorbance of the characteristic functional group vibrations of LDPE/ Aferi clay nanocomposites at different percentage Aferi clay loadings.

CLAY LOADINGS (%)	ABSORBANCE OF CHARACTERISTIC FUNCTIONAL GROUPS				
	Si-O vibrations	C-H symmetric	C-H asymmetric	C-H bending	C-H rocking
0	0.0000	0.5831	0.5437	0.3430	0.2542
2	0.2515	1.5135	0.9517	0.7306	0.4703
4	0.3732	1.1625	1.0374	0.629	0.4332
6	0.3961	1.3164	1.1670	0.6507	0.4496
8	0.4639	1.3011	1.1290	0.5716	0.3839
10	0.4997	0.6126	0.5691	0.3948	0.3247

APPENDIX 4: calculations of d-spacing of pristine and modified Mfensi and Aferi clay samples, as well as average particle size of the clay samples.

Appendix 4.1: d-spacing calculations for pristine and modified Mfensi and Aferi clay samples.

Calculation from the Bragg's law, relating d-spacing of the crystalline material to the wavelength of incident radiation and the angle of diffraction, is found below.

$$d = \frac{n\lambda}{2 \sin \theta} \text{ ----- (1)}$$

Where d is the interplanar distance, the integer n is the order of diffracted beam, λ wavelength of the incident x-ray, and θ being the angle of incidence of the x-ray beam.

Table A.4.1: calculation of d-spacing for pristine and modified Mfensi and Aferi clays.

Clay	n	λ	$n\lambda$	θ	$\sin \theta$	2	2Sin θ	$d = (n\lambda / 2\sin\theta)$
PMC	1	1.5E-10	1.5 Å	13.33	0.2305	2	0.461	3.25Å
MMC	1	1.5E-10	1.5 Å	13.33	0.2305	2	0.461	3.25Å
PAC	1	1.5E-10	1.5 Å	13.45	0.2325	2	0.465	3.22Å
MAC	1	1.5E-10	1.5 Å	13.45	0.2325	2	0.465	3.22Å

Key

- PAC - Pristine Aferi Clay
- MAC - Modified Aferi clay

- PMC – Pristine Mfensi Clay
- MMC- Modified Mfensi Clay

Appendix 4.2: Calculating average particle size of modified (organo) Mfensi and Aferi clay samples prepared.

Calculations are made using Scherrer's equation as follows:

$$t = \frac{0.9\lambda}{B \cos \theta}$$

where:

t = Average particle size of organoclay

λ = wavelength of X-ray radiation = 1.54 Å

θ = diffraction angle

B = angular width of the extent of broadening of diffraction peak measured at half maximum intensity in radians.

$$\text{But, } B = \frac{1}{2} (2\theta_2 - 2\theta_1)$$

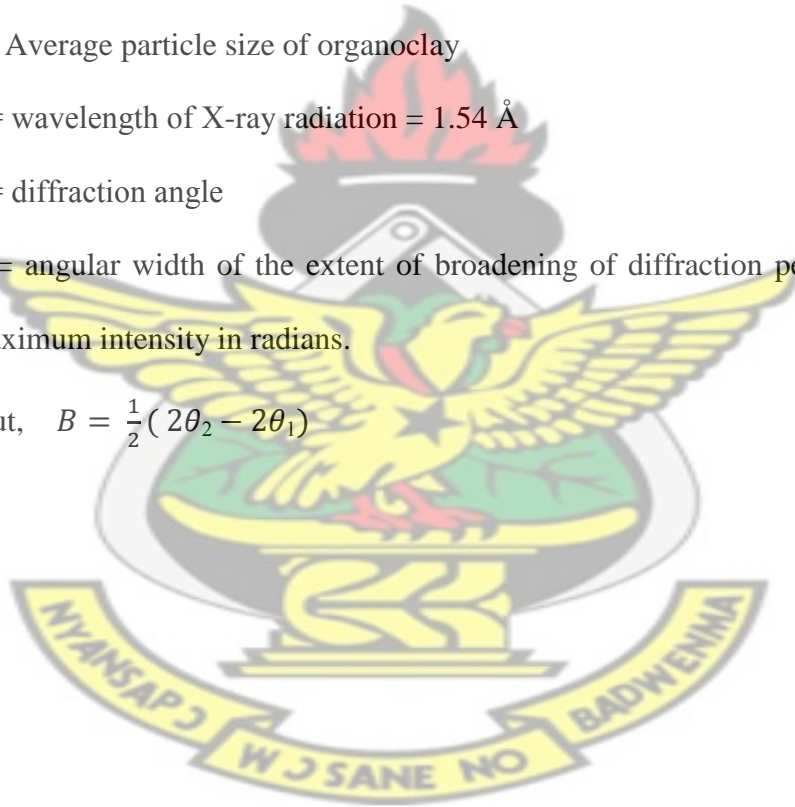
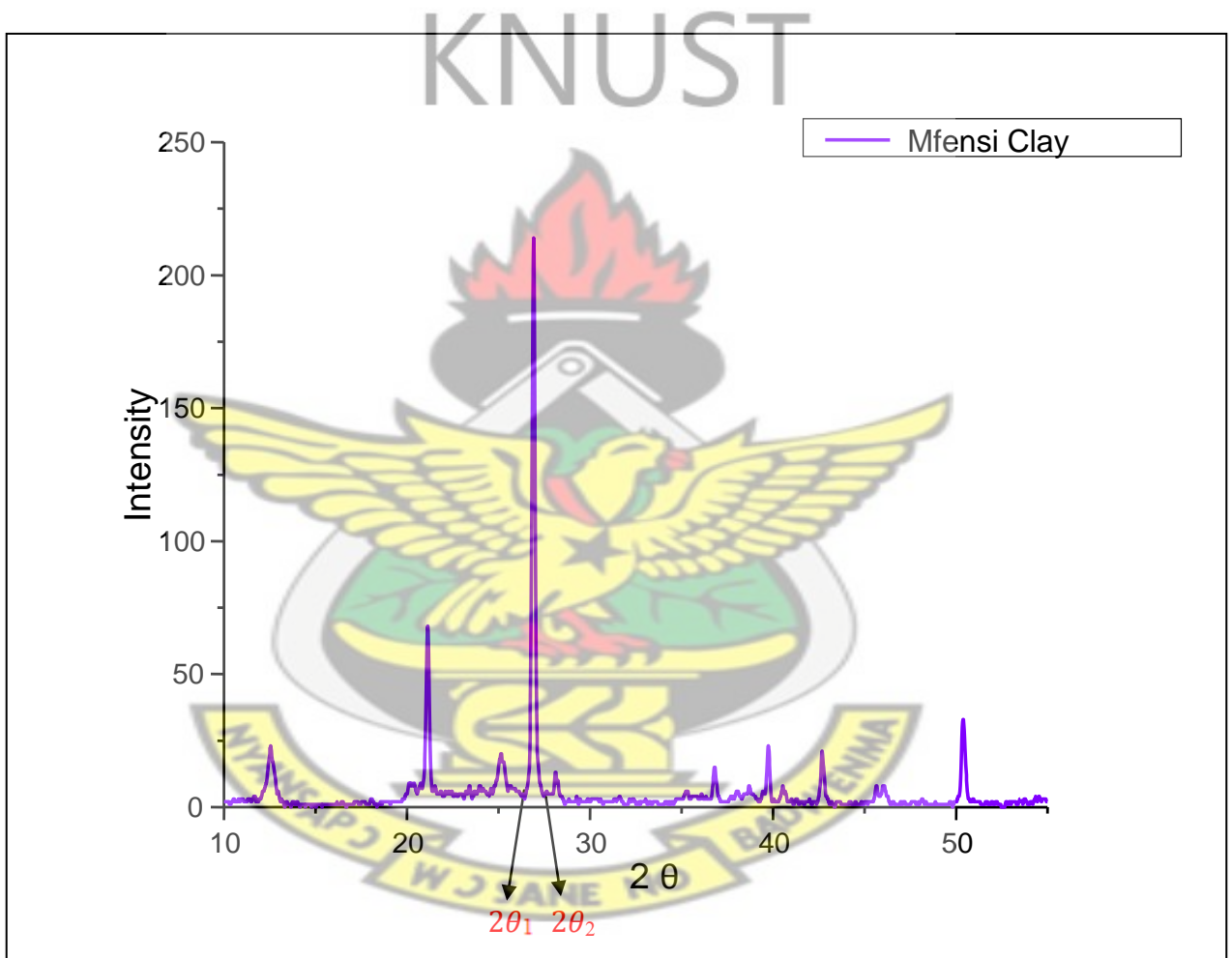


Figure A.4.1: calculations average particle size of Mfensi clay.



CLAY	0.9	λ	0.9λ	0.5	$2\theta_1$	$2\theta_2$	$(2\theta_2 - 2\theta_1)$	$B = 0.5(2\theta_2 - 2\theta_1)$	θ	$B\cos\theta$	$t = \frac{0.9\lambda}{B\cos\theta}$
------	-----	-----------	--------------	-----	-------------	-------------	---------------------------	----------------------------------	----------	---------------	--------------------------------------

Mfensi	0.9	1.5E-10	1.35E-10	0.5	26.52	26.57	0.05	0.025	13.33	0.024	5.54nm
--------	-----	---------	----------	-----	-------	-------	------	-------	-------	-------	--------

Table A.4.2: calculation of average particle size of Mfensi clay.

KNUST

Figure A.4.2: calculations of average particle size of Aferi clay.

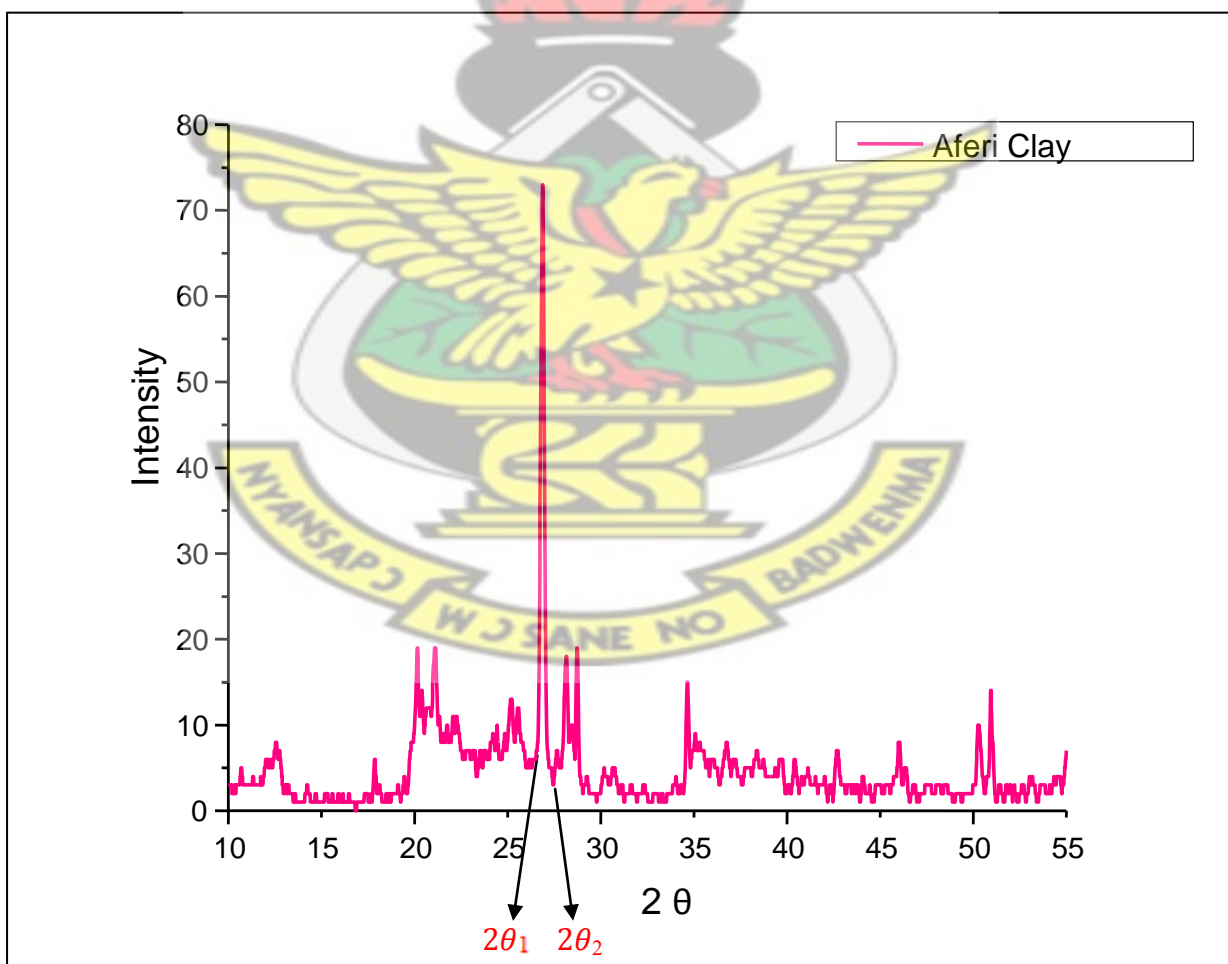


Table A.4.5: calculation of average particle size of Aferi clay.

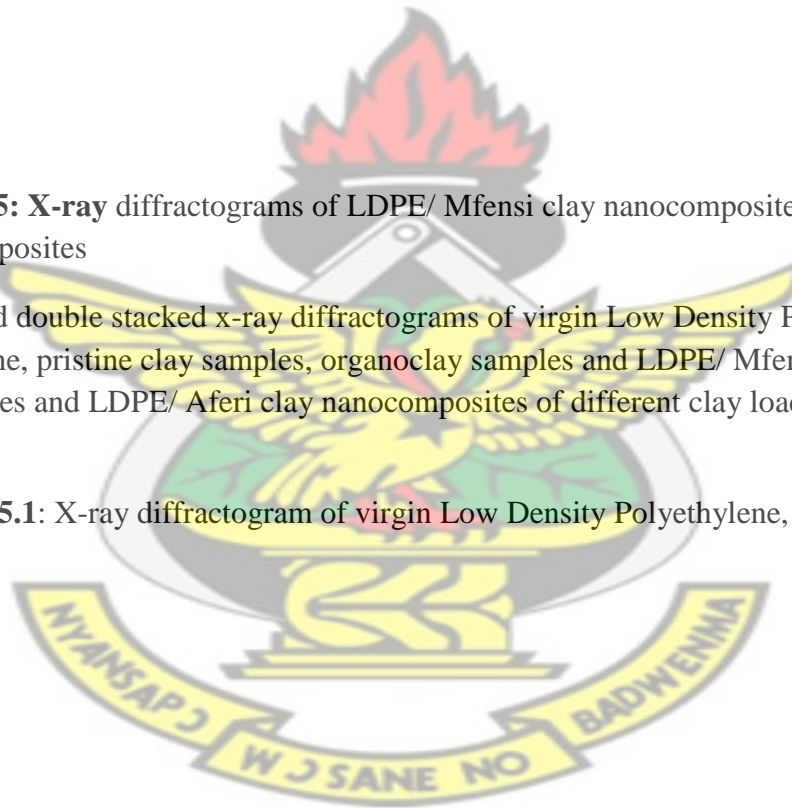
CLAY	0.9	λ	0.9λ	0.5	$2\theta_1$	$2\theta_2$	$(2\theta_2-2\theta_1)$	$B = 0.5(2\theta_2-2\theta_1)$	θ	$B\cos\theta$	$t = \frac{0.9\lambda}{B\cos\theta}$
Aferi clay	0.9	1.5E-10	1.35E-10	0.5	26.34	26.39	0.05	0.025	13.45	0.024	5.55nm

KNUST

APPENDIX 5: X-ray diffractograms of LDPE/ Mfensi clay nanocomposites and LDPE/ Aferi clay nanocomposites

The single and double stacked x-ray diffractograms of virgin Low Density Polyethylene, octadecylamine, pristine clay samples, organoclay samples and LDPE/ Mfensi clay nanocomposites and LDPE/ Aferi clay nanocomposites of different clay loadings are presented below.

Figure A.5.1: X-ray diffractogram of virgin Low Density Polyethylene, (LDPE).



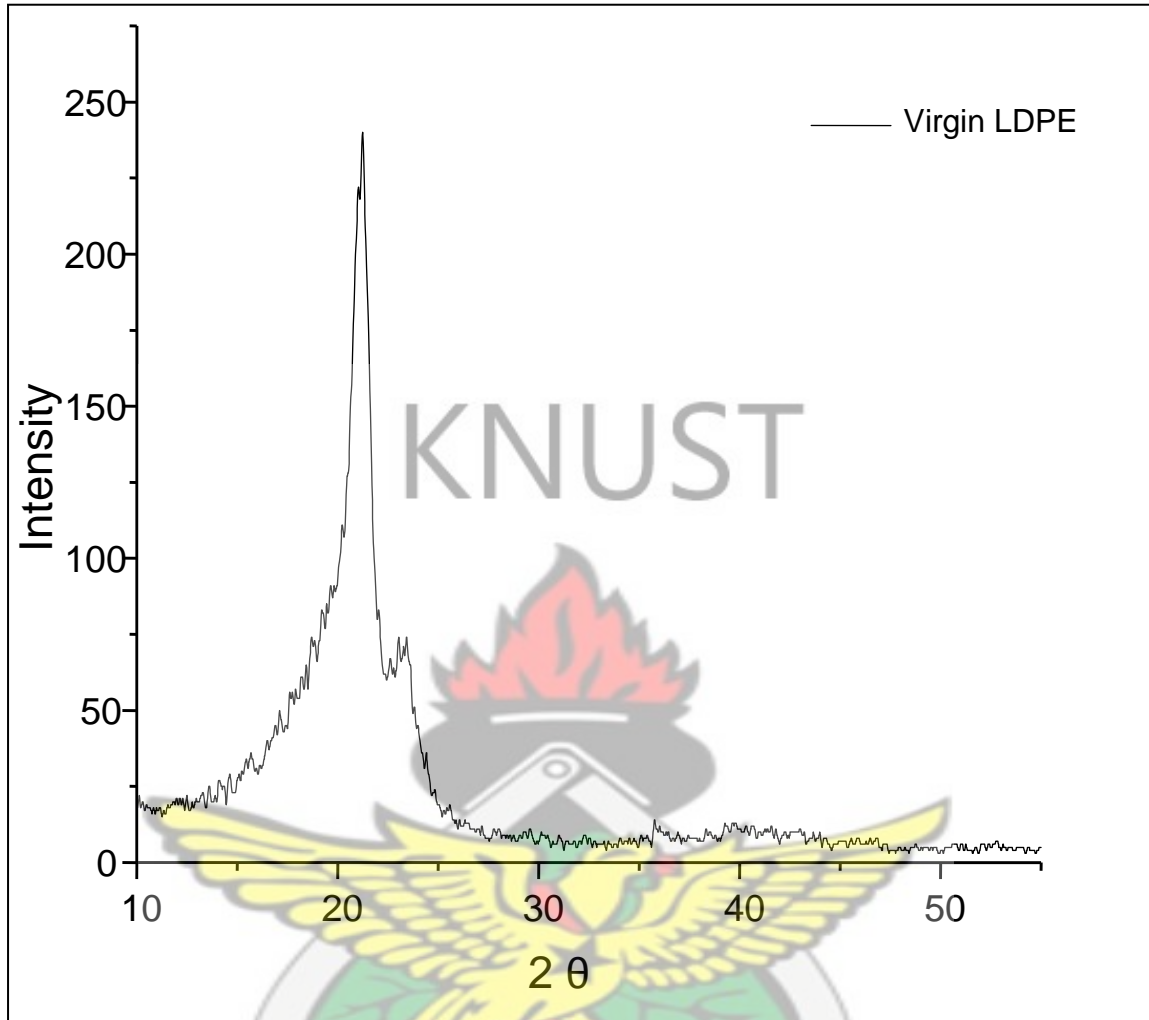
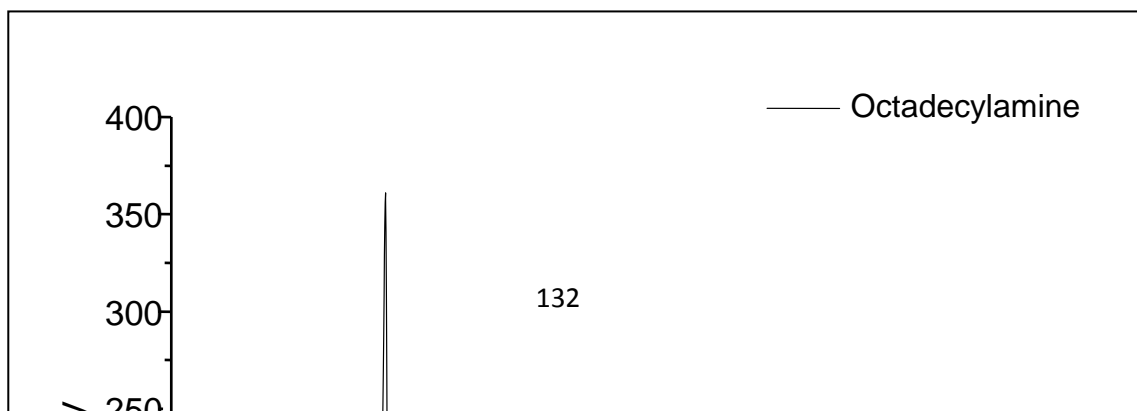


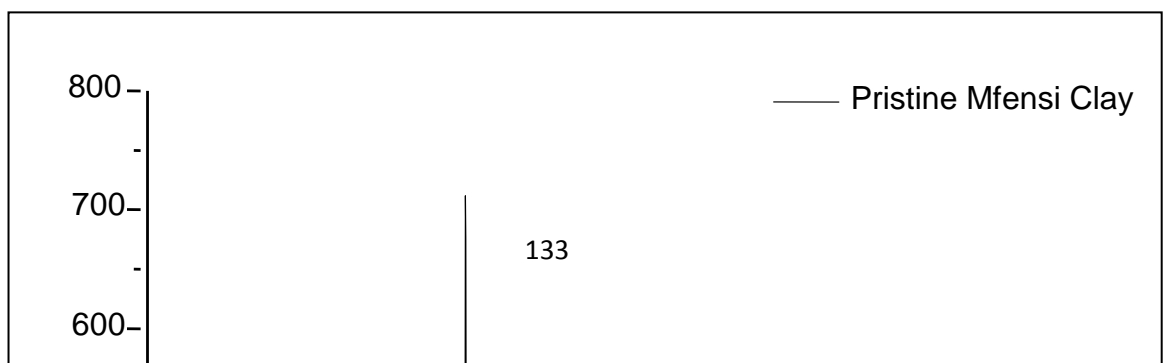
Figure A.5.2: X-ray diffractogram of octadecylamine.



KNUST



Figure A.5.3: X-ray diffractogram of pristine (raw) Mfensi Clay.



KNUST



Figure A.5.4: X-ray diffractogram of Modified Mfensi Clay

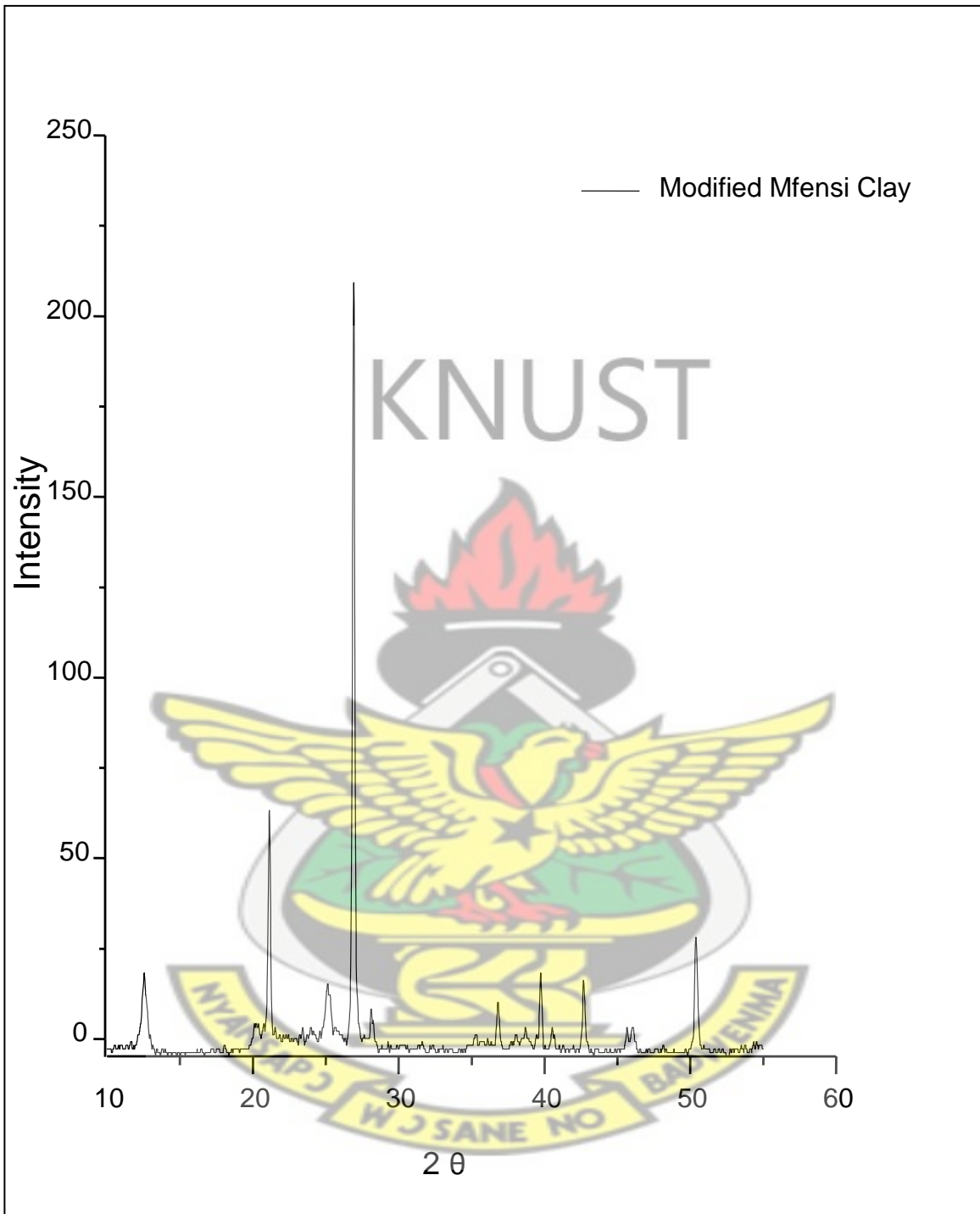


Figure A.5.5: X-ray diffractogram of Pristine Aferi Clay.

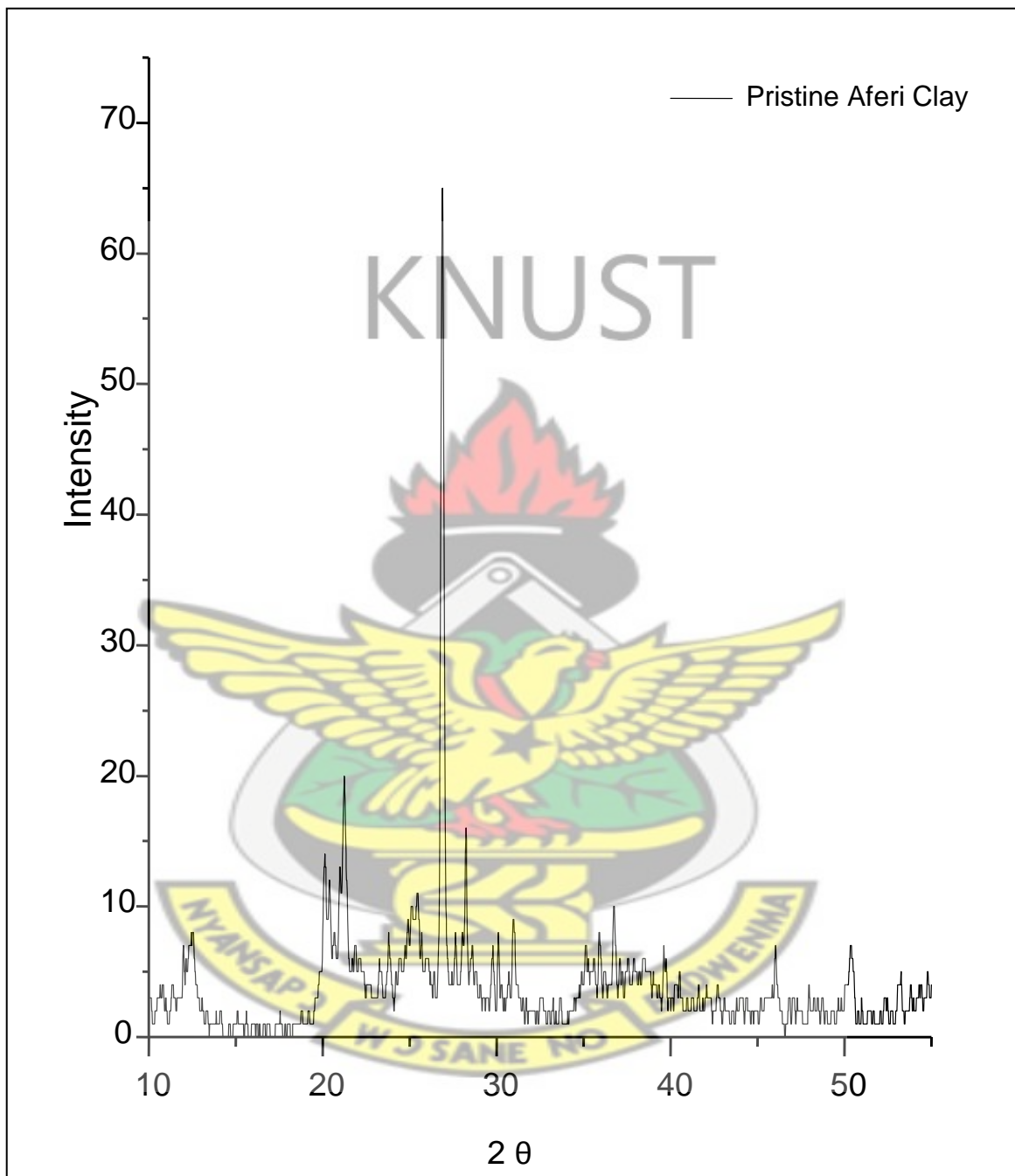


Figure A.5.6: X-ray diffractogram of Modified Aferi Clay.

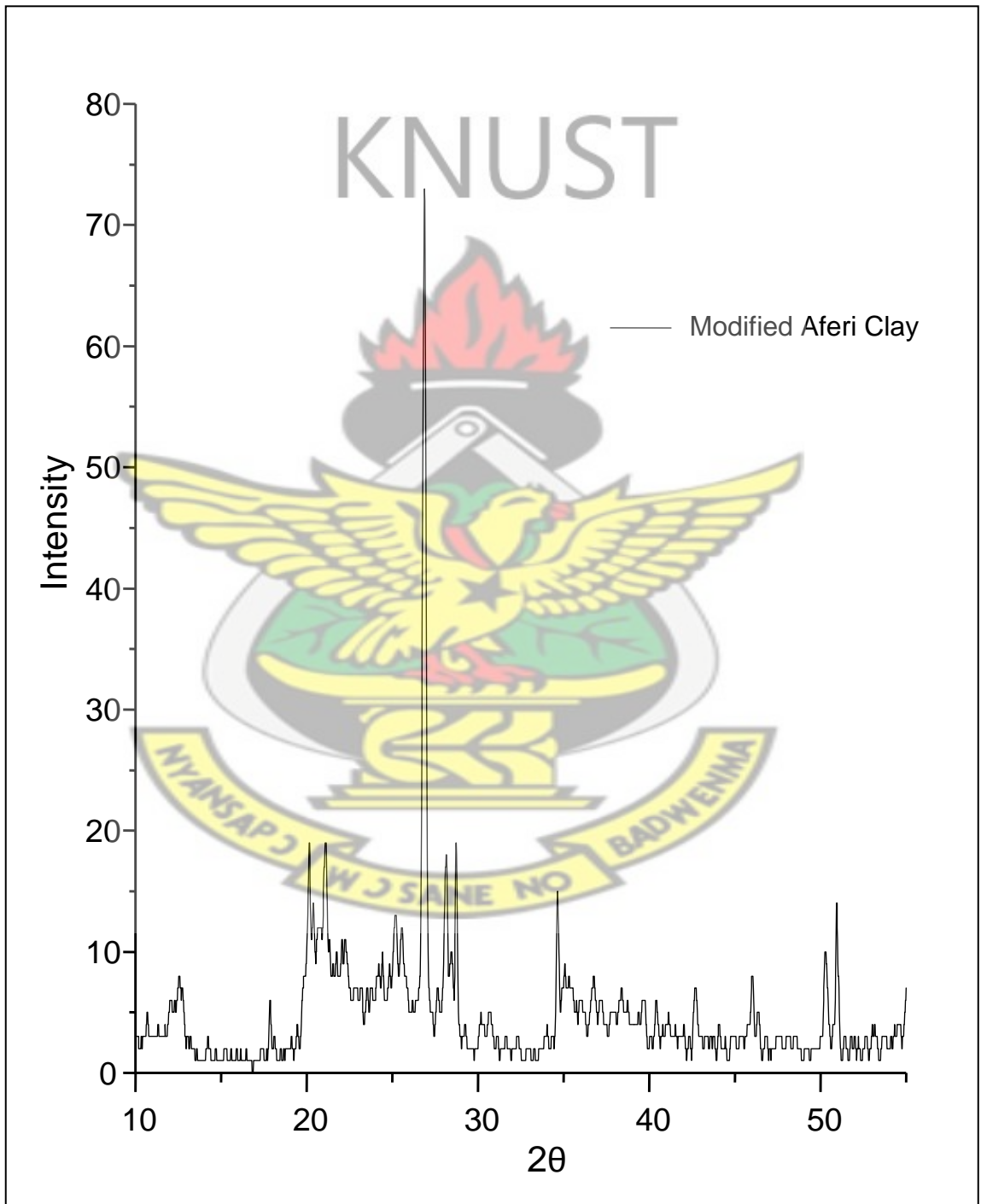


Figure A.5.7: X-ray diffractogram of 98 wt% LDPE/ 2 wt% Aferi clay nanocomposite.

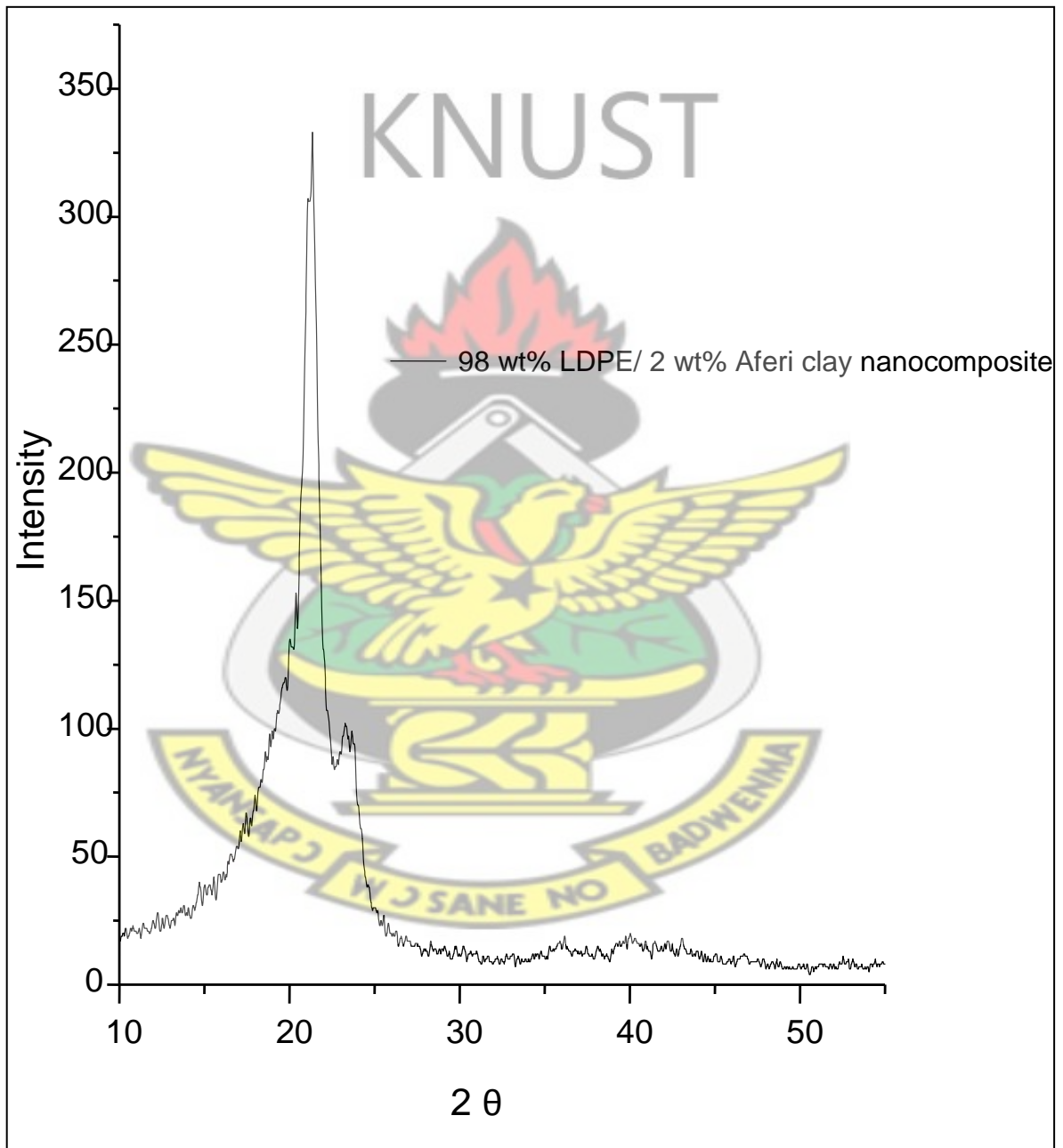


Figure A.5.8: X-ray diffractogram of 94 wt% LDPE/ 6 wt% Aferi clay nanocomposite.

KNUST



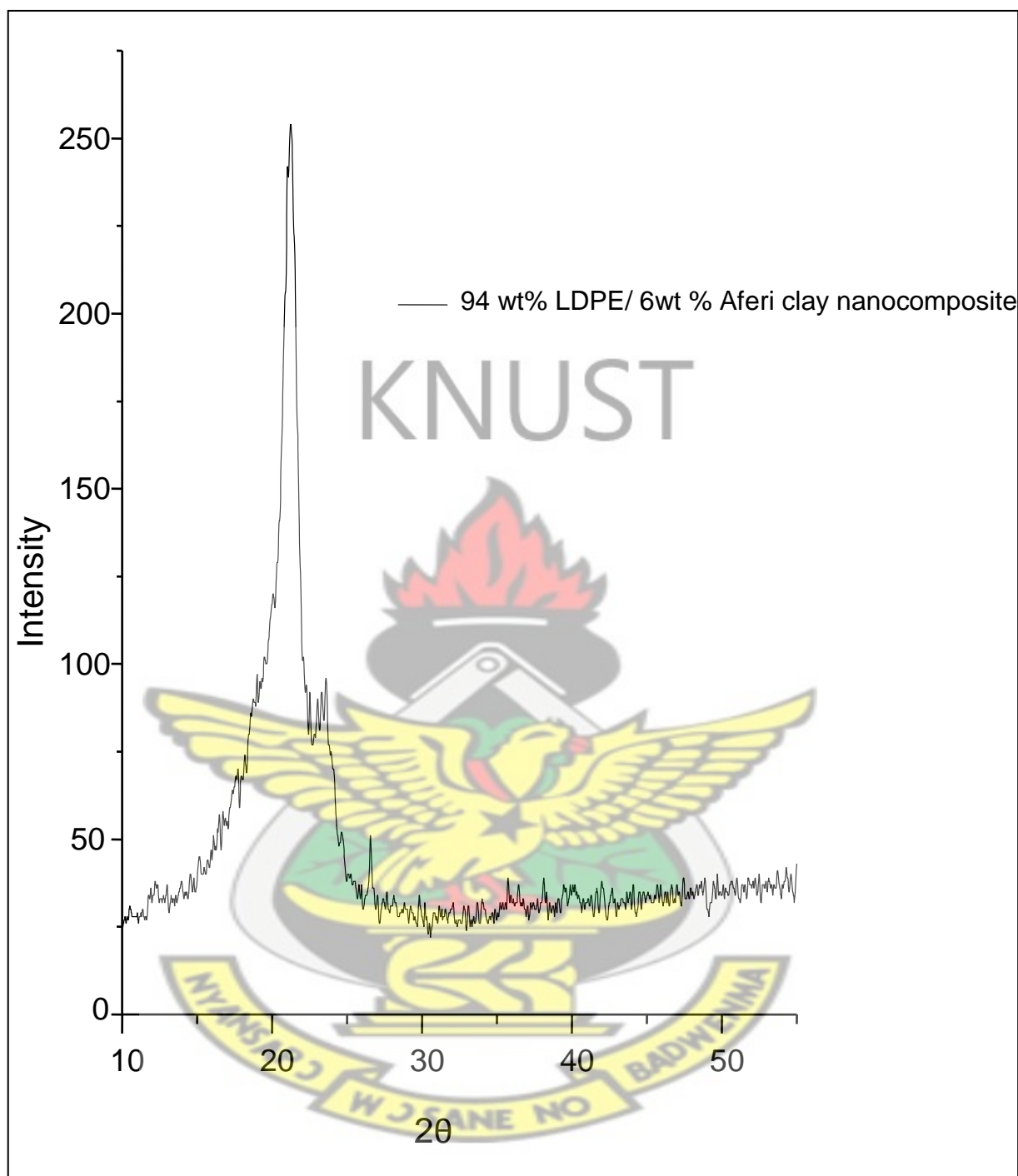


Figure A.5.9: X-ray diffractogram of 90 wt% LDPE/ 10 wt% Aferi clay nanocomposite.

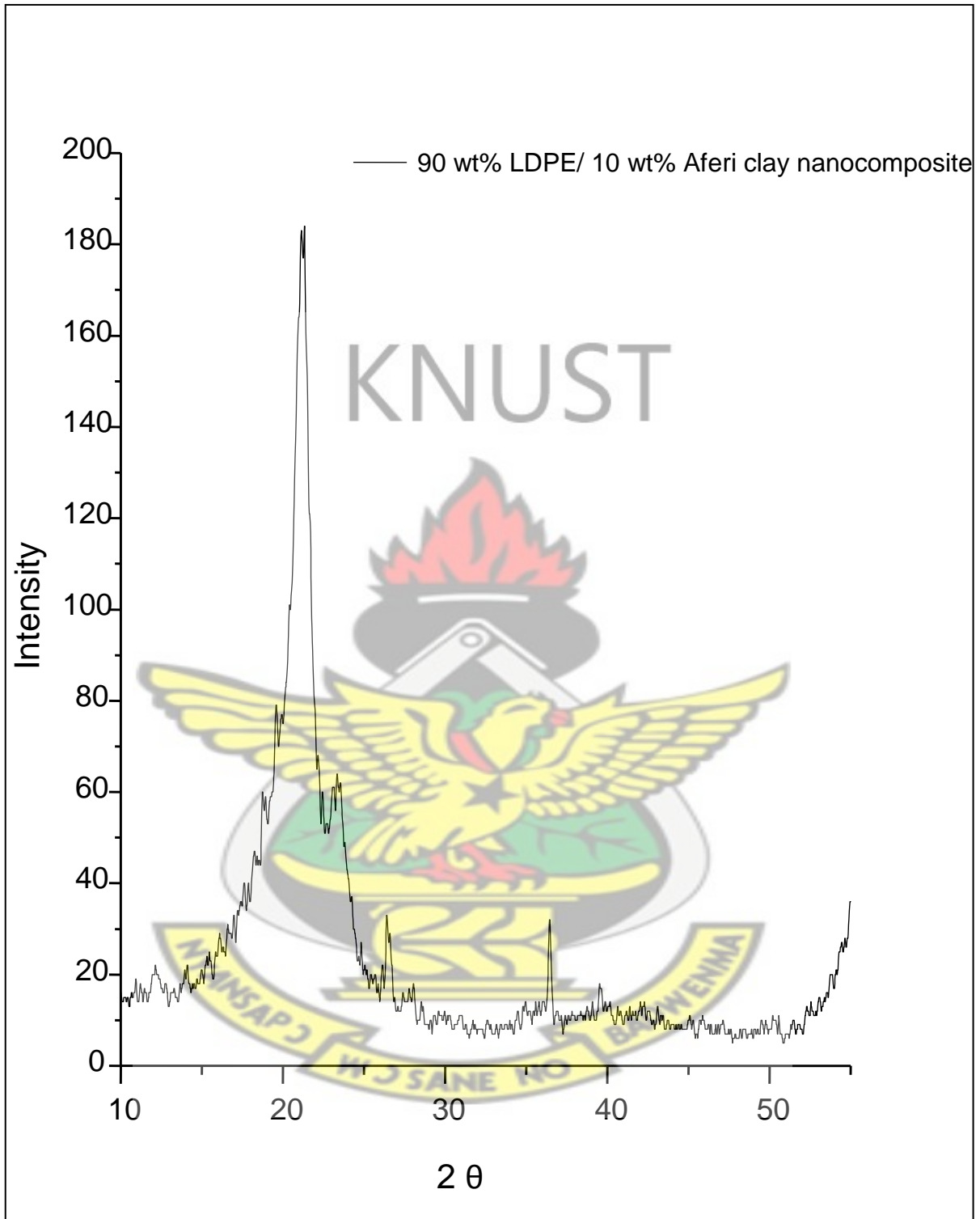


Figure A.5.10: X-ray diffractogram of 98 wt% LDPE/ 2 wt% Mfensi clay nanocomposite.

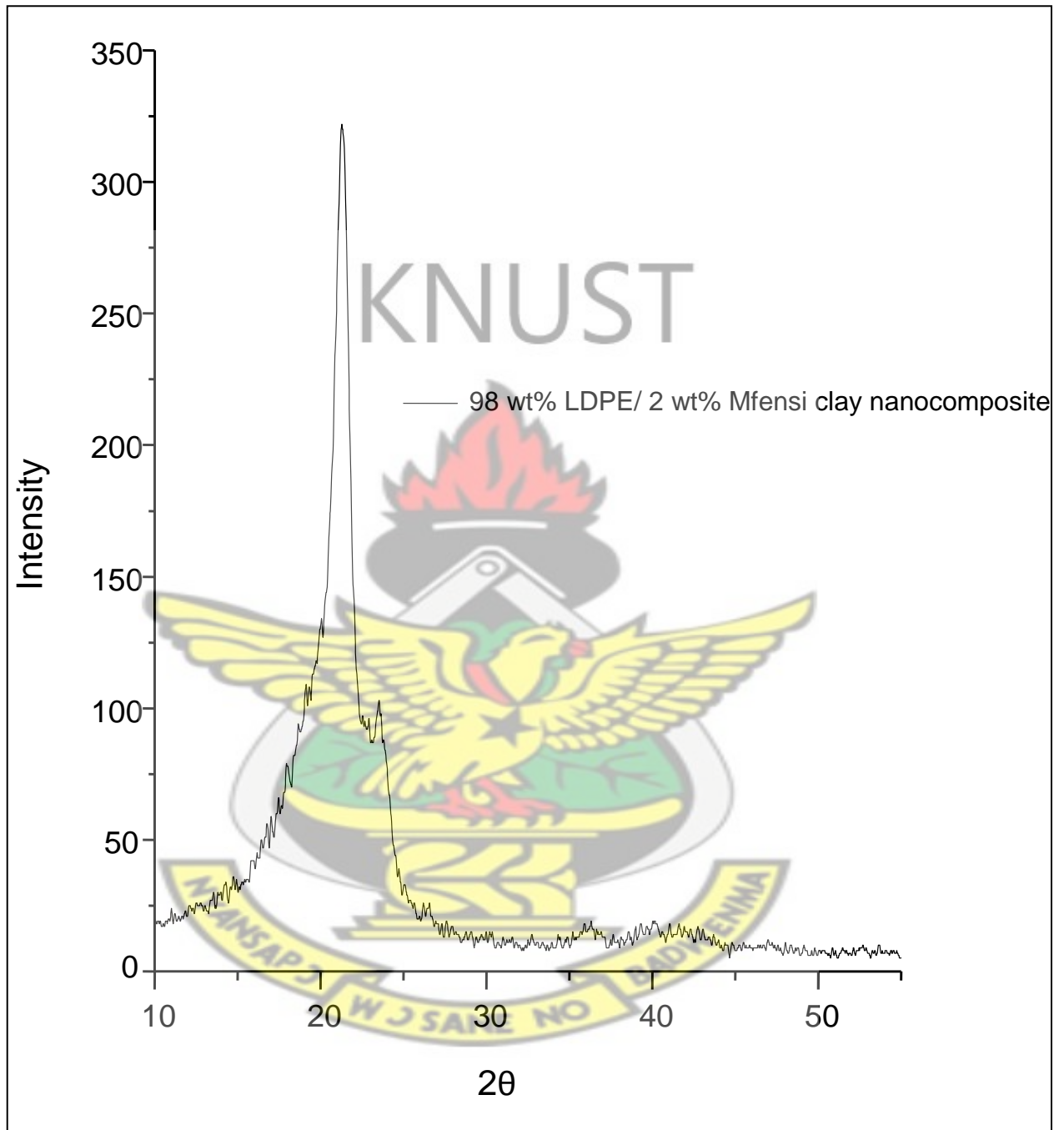


Figure A.5.11: X-ray diffractogram of 94 wt% LDPE/ 6 wt% Mfensi clay nanocomposite.

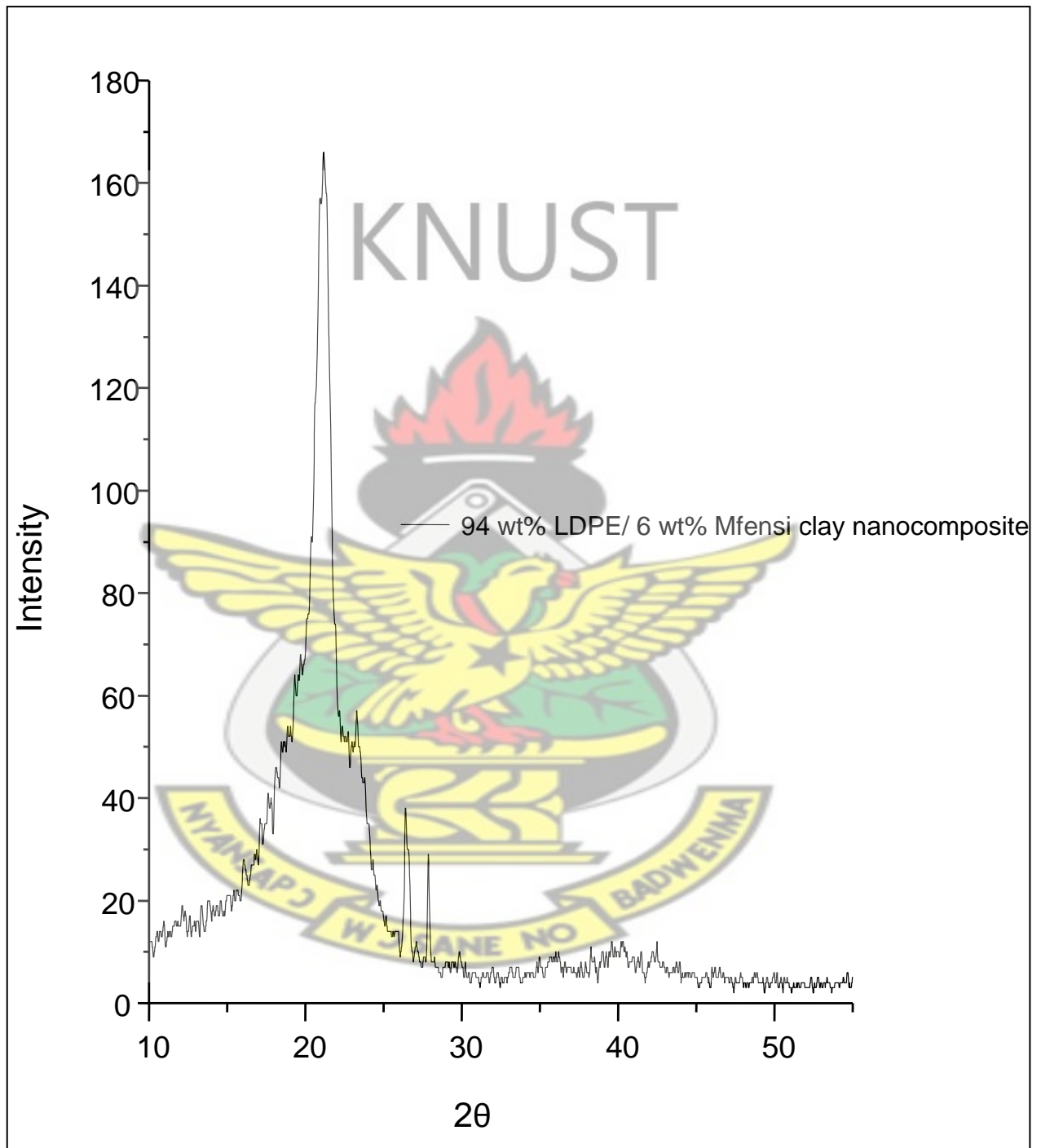


Figure A.5.12: X-ray diffractogram of 90 wt% LDPE/ 10 wt% Mfensi clay nanocomposite.

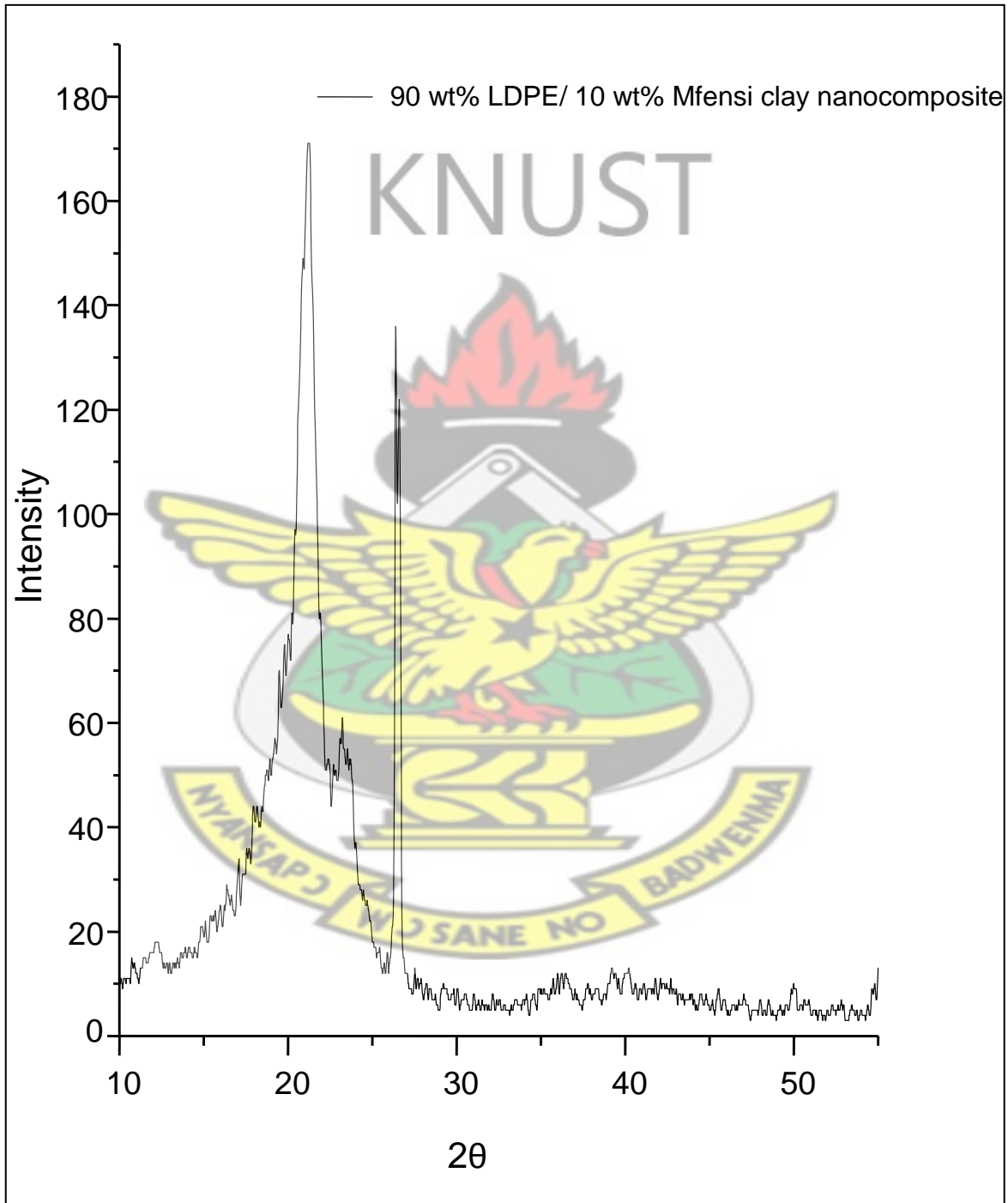


Figure A.5.13: Stacked x-ray diffractogram of virgin LDPE and modified Mfensi clay.

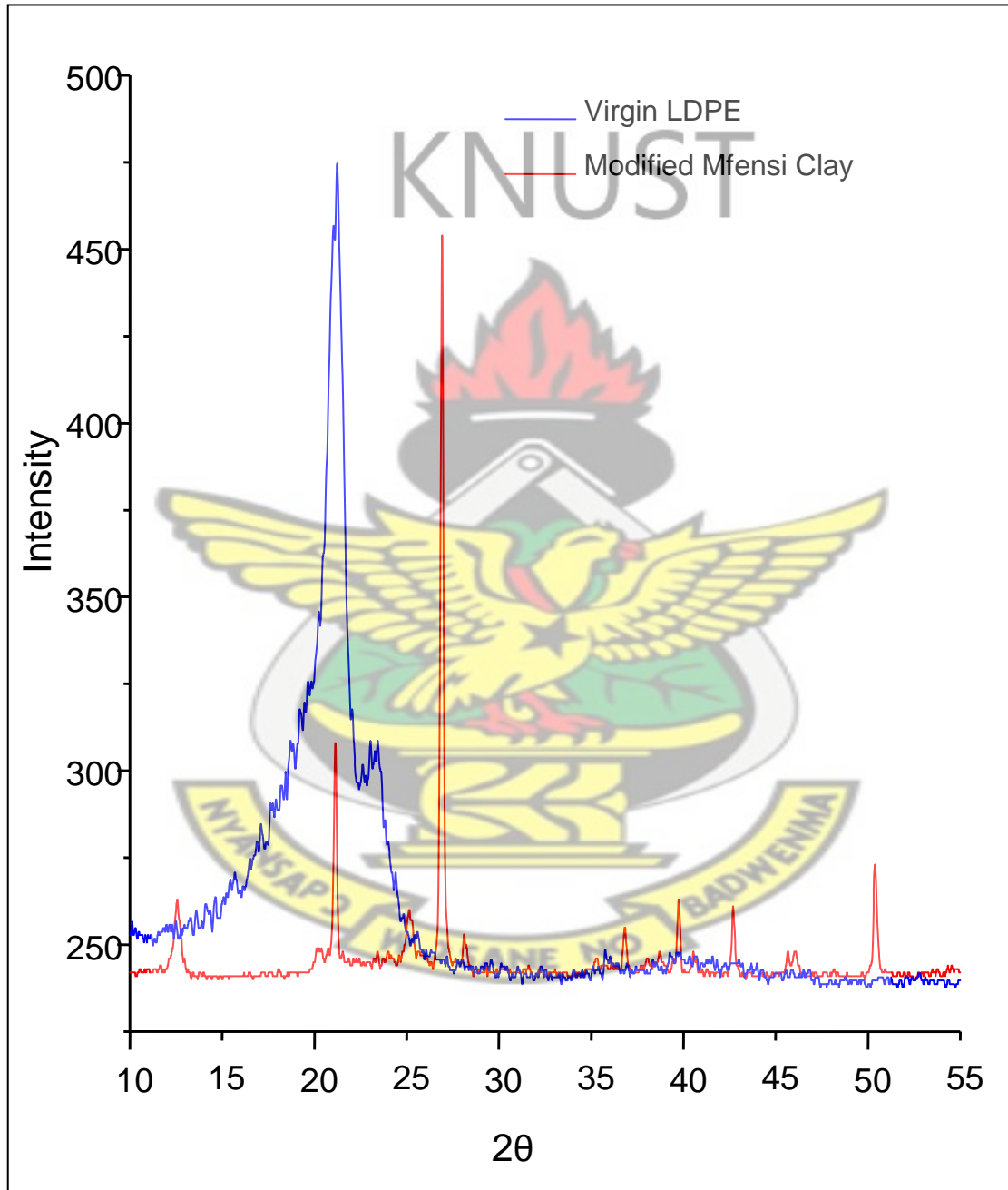


Figure A.5.14: Stacked x-ray diffractogram of virgin LDPE and modified Aferi clay.

